

Optimisation and control of boundary layer flows

by

Antonios Monokrousos

June 2009
Technical Reports
Royal Institute of Technology
Department of Mechanics
SE-100 44 Stockholm, Sweden

Akademisk avhandling som med tillstånd av Kungliga Tekniska Högskolan i Stockholm framlägges till offentlig granskning för avläggande av teknologie licentiatsexamen fredagen den 14 november 2008 kl 10.30 i K1, Kungliga Tekniska Högskolan, Teknikringen 56, entréplan, Stockholm.

©Antonios Monokrousos 2009 Universitetsservice US-AB, Stockholm 2009

Optimisation and control of boundary layer flows

Antonios Monokrousos

Linné Flow Centre, Department of Mechanics, Royal Institute of Technology (KTH)
SE-100 44 Stockholm, Sweden

Abstract

Both optimal disturbances and optimal control are studied by means of numerical simulations for the case of the flat-plate boundary-layer flow. The optimisation method is the Lagrange multiplier technique where the objective function is the kinetic energy of the flow perturbations and the constraints involve the linearised Navier–Stokes equations. We consider both the optimal initial condition leading to the largest growth at finite times and the optimal time-periodic forcing leading to the largest asymptotic response. The optimal disturbances for spanwise wavelengths of the order of the boundary layer thickness are streamwise vortices exploiting the lift-up mechanism to create streaks. For long spanwise wavelengths it is the Orr mechanism combined with the amplification of oblique wave packets that is responsible for the disturbance growth. Control is applied to the bypass-transition scenario with high levels of free-stream turbulence. In this scenario low frequency perturbations enter the boundary layer and streamwise elongated disturbances emerge due to the non-modal growth. These so-called streaks are growing in amplitude until they reach high enough energy levels and breakdown into turbulent spots via their secondary instability. When control is applied in the form of wall blowing and suction, within the region that it is active, the growth of the streaks is delayed, which implies a delay of the whole transition process. Additionally, a comparison with experimental work is performed demonstrating a remarkable agreement in the disturbance attenuation once the differences between the numerical and experimental setup are reduced.

Descriptors: boundary layer, control, estimation, optimal disturbances, Lagrange method

Preface

This thesis deals with optimal control and optimal disturbances in flows over flat-plate boundary layers. A brief overview of the basic concepts and methods is presented in the first part. The second part is a collection of the following articles:

Paper 1. A. MONOKROUSOS, L. BRANDT, P. SCHLATTER & D. S. HENNINGSON, 2008

DNS and LES of estimation and control of transition in boundary layers subject to free-stream turbulence. *Int. J. Heat and Fluid Flow*, 29, Issue 3 841-855

Paper 2. F. LUNDELL, A. MONOKROUSOS & L. BRANDT, 2009

Feedback Control of Boundary Layer Bypass Transition: Experimental and Numerical Progress. *47th AIAA Aerospace Sciences Meeting, Orlando, FL*

Paper 3. A. MONOKROUSOS, E. ÅKERVIK, L. BRANDT & D. S. HENNINGSON, 2009

Global optimal disturbances in the Blasius boundary-layer flow using time-steppers. *Submitted to the Journal of Fluid Mechanics*.

Division of work between authors

The main advisor for the project is Prof. Dan Henningson (DH). Prof. Luca Brandt (LB) has acted as co-advisor.

Paper 1

The code development and computations relevant to the control part were performed by Antonios Monokrousos (AM) with feedback from LB. The code development and computations relevant to the LES part were performed by Philipp Schlatter (PS). Most of the paper has been written by AM with feedback from LB and DH except the LES part, which was written by PS with feedback from AM, LB and DH.

Paper 2

The experiments and system-identification computations were performed by Fredrik Lundell (FL). The code development and computations relevant to the optimal control part were performed by AM with feedback from LB. The writing of the paper was divided accordingly.

Paper 3

The implementation of the adjoint DNS and the optimal initial condition and forcing power iteration scheme was performed by AM with feedback from Espen Åkervik (EÅ) and LB, whereas the Arnoldi iteration scheme using ARPACK method was implemented by EÅ. The computations were for the most part performed by AM except those performed with the Arnoldi method which were done by EÅ. The writing of the paper was done by AM, EÅ and LB with feedback from DH.

Abstract	iii
Preface	iv
Part I	1
Chapter 1. Introduction	2
Chapter 2. Theoretical background	3
2.1. Basic flow, Governing equations	3
2.2. Objective function and the Lagrangian approach	5
Chapter 3. Optimal disturbances	7
3.1. Initial condition	7
3.2. Forcing	8
Chapter 4. Optimal Control	12
4.1. Full-information Control	12
4.2. Estimation	13
4.3. Compensator	15
4.4. Approaching the experiment	15
Chapter 5. Summary of the papers	18
Paper 1	18
Paper 2	18
Paper 3	19
Chapter 6. Conclusions and Outlook	20
Acknowledgements	22
Bibliography	23
Part II	25
Paper 1. DNS and LES of estimation and control of transition in boundary layers subject to free-stream turbulence	27
Paper 2. Feedback Control of Boundary Layer Bypass Transition: Experimental and Numerical Progress	65
Paper 3. Global optimal disturbances in the Blasius boundary-layer flow using time-steppers	85

Part I

Introduction

CHAPTER 1

Introduction

Fluids are all around us. We experience them in all kind of manners and ways. We feel the water opposing us when we swim but also keeping us on the surface, we sense the air around us when we run or bike, finally we just take a sip from a glass of good red wine. However, we hardly realise and even less understand the complicated phenomena taking place within them.

It is impressive how we are able to conceive and describe immense processes, light years away from us, for instance how a star is born or how it dies and also immensely small phenomena like how few sub-atomic particles interact and combine to give us the huge variety of elements found in nature; yet again something so familiar and commonplace like what happens to the flow of water out of an open tap elude us: suddenly and for no apparent reason the simple smooth laminar flow turns into a chaotic and turbulent motion.

This thesis deals with problems of the kind and also attempts to shed some light on how one would try to prevent a catastrophic event like the one described above by applying *control*. The shift of a flow from the laminar to turbulent state is called transition to turbulence and it has been the subject of study for more than a century. However, the more complicated the flow configuration becomes i.e. the geometrical and physical characteristics of the solid objects that the fluid interacts with, the less intuitive or apparent the transition mechanisms are.

In real flows often (but not always) the transition is initiated by small in amplitude perturbations and we can assume that their dynamics can be described, at least at an initial stage, by linear theory. However, whether transition will occur or not does not depend solely on the perturbation amplitude but also on its shape in space. Thus there must be some perturbations that are more efficient at initiating transition than others. These are called *optimal disturbances* and since they represent the path which the flow is taking in order to go from the laminar state to the turbulent they can help understand the transition process.

Theoretical background

2.1. Base flow, Governing equations

This study is concerned with the stability and control of the classical spatially-evolving two-dimensional flat-plate boundary-layer flow subject to three-dimensional disturbances. The system of partial differential equations (PDE) used as a model for the flow are the Navier-Stokes equations. It is, however, enough to assume perturbations of small amplitude and linearise around a base flow enabling the use of optimisation theory that requires a linear system of governing equations. The model describing the dynamics of the small perturbations are therefore the linearised Navier-Stokes equations,

$$\partial_t \mathbf{u} + (\mathbf{U} \cdot \nabla) \mathbf{u} + (\mathbf{u} \cdot \nabla) \mathbf{U} = -\nabla \pi + Re^{-1} \Delta \mathbf{u} + \mathbf{g}, \quad (2.1)$$

$$\nabla \cdot \mathbf{u} = 0, \quad (2.2)$$

where $\mathbf{U} = (U(x, y), V(x, y), 0)^T$ is the two-dimensional base flow and $\mathbf{u} = (u(\mathbf{x}, t), v(\mathbf{x}, t), w(\mathbf{x}, t))^T$ is the small perturbation representing the departure from the base flow. $\mathbf{u}' = \mathbf{U} + \mathbf{u}$ would be the total velocity vector. $\mathbf{x} = (x, y, z)^T$ is the spatial position vector where x corresponds to the streamwise, y to the wall-normal and z to the spanwise direction. Our domain of interest is defined by a rectangular box

$$\Omega = [0, L_x] \times [0, L_y] \times \left[-\frac{L_z}{2}, \frac{L_z}{2}\right]$$

where L_x, L_y and L_z are the corresponding lengths in the three directions. The term \mathbf{g} is a forcing function that can assume different roles depending on if for instance we apply control or seek optimal forcing functions and π is the perturbation pressure. All the quantities in equations (2.1) and (2.2) are non-dimensional. In particular velocities are scaled with the free-stream velocity U_∞ , lengths with the inflow displacement thickness δ_0^* and time with δ_0^*/U_∞ .

The flow is considered to be incompressible and viscous. Two different Reynolds numbers are used throughout this thesis. For the most part the Reynolds number based on the displacement thickness δ^* ,

$$Re_{\delta^*} = \frac{U_\infty \delta^*}{\nu}, \quad (2.3)$$

but also the Reynolds number based on the distance from the leading edge x' ,

$$Re_x = \frac{U_\infty x'}{\nu}, \quad (2.4)$$

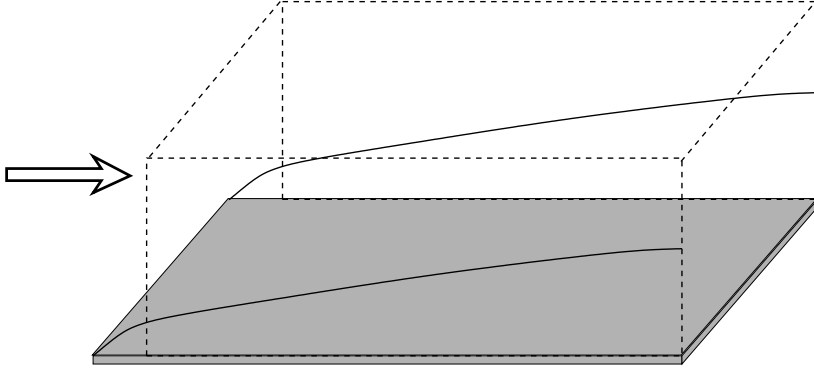


FIGURE 2.1. The boundary layer flow. The dashed lines indicate the computational box. The arrow shows the direction of the flow.

are used. ν is the kinematic viscosity.

For this work both Direct Numerical Simulations (DNS) as well as Large Eddy Simulations (LES) were used by employing a fully-spectral numerical code (Chevalier *et al.* 2007b).

2.1.1. State-Space formulation

As it can also be seen from equations (2.1) and (2.2) for incompressible flows the pressure only acts as a Lagrange multiplier to maintain divergence-free velocity fields. The pressure itself can be formally expressed as a function of the velocity vector $\mathbf{u} = (u, v, w)^T$ enabling the use of \mathbf{u} as the state variable and to re-write the equations in a compact form (Kreiss *et al.* 1994). The momentum part of the forced linearized Navier–Stokes equations can be written as

$$\partial_t \mathbf{u} = -(\mathbf{U} \cdot \nabla) \mathbf{u} - (\mathbf{u} \cdot \nabla) \mathbf{U} + Re^{-1} \Delta \mathbf{u} + \nabla \pi + \mathbf{g}, \quad (2.5)$$

where the pressure is a known function of the divergence-free velocity field \mathbf{u} and base flow \mathbf{U}

$$\Delta \pi = -\nabla \cdot ((\mathbf{U} \cdot \nabla) \mathbf{u} + (\mathbf{u} \cdot \nabla) \mathbf{U}). \quad (2.6)$$

Inversion of the Laplacian requires boundary conditions and formally we may obtain these by projecting (2.5) on the outwards pointing normal of the domain \mathbf{n} . The solution of (2.6) is denoted as $\pi = \mathcal{K} \mathbf{u}$ so we have with the following expression for the system operator

$$\mathcal{A} = -(\mathbf{U} \cdot \nabla) - (\nabla \mathbf{U}) + Re^{-1} \Delta + \nabla \mathcal{K}. \quad (2.7)$$

The resulting state space formulation of equation (2.5) reads

$$(\partial_t - \mathcal{A}) \mathbf{u} - \mathbf{g} = 0, \quad \mathbf{u}(0) = \mathbf{u}_0, \quad (2.8)$$

with solution

$$\mathbf{u}(t) = \underbrace{\exp(\mathcal{A}t)\mathbf{u}_0}_{\text{initial value problem}} + \underbrace{\int_0^t \exp(\mathcal{A}\tau)\mathbf{g}(\mathbf{x}, t - \tau) d\tau}_{\text{forced problem}}. \quad (2.9)$$

Alternatively \mathcal{A} may also be defined using semi-group theory, where it is referred to as an infinitesimal generator. First, the evolution operator $\mathcal{T}(t)$ is defined as the operator that maps a solution at time t_0 to time $t_0 + t$.

$$\mathbf{u}(t + t_0) = \mathcal{T}(t)\mathbf{u}(t_0). \quad (2.10)$$

The infinitesimal generator of $\mathcal{T}(t)$, \mathcal{A} , is defined through the action of \mathcal{T} for an infinitesimal amount of time δt

$$\mathcal{A}\mathbf{u} = \lim_{\delta t \rightarrow 0} \frac{\mathcal{T}(\delta t)\mathbf{u} - \mathbf{u}}{\delta t}. \quad (2.11)$$

See also Trefethen *et al.* (1993) and Bagheri *et al.* (2009).

2.2. Objective function and the Lagrangian approach

The optimisation method employed here is called the Lagrange approach. The idea originates from classical mechanics where the Lagrangian is an alternative way to write the energy of a dynamical system. Using calculus of variations one seeks minima of the Lagrangian which often correspond to preferred (by the system) states. The method is generalised so that new states (still solutions to the original PDE) are recovered that correspond to extrema of a chosen quantity/functional of the system. Additional constraints, apart from the governing equations themselves, can be added according to the needs of a specific problem. Once the Lagrangian is set-up it is a calculus problem to rebuild a new set of PDEs whose solution not only satisfies the original PDE but is additionally an extremum with respect to the chosen objective. The chosen functional is known as objective function and the method is referred to as the Lagrange multiplier technique.

The objective function we choose is the kinetic energy of the perturbation field while the constraints can be either physical, for instance the need to have a divergence-free velocity field (part of the governing equations) or imposed like the demand to have an initial condition of unit amplitude. Thus we introduce the norm based on the kinetic energy of the perturbations

$$\|\mathbf{u}(t)\|^2 = (\mathbf{u}(t), \mathbf{u}(t)) = \int_{\Omega} \mathbf{u}^H \mathbf{u} d\Omega. \quad (2.12)$$

The general form of the Lagrangian used throughout this thesis is

$$\mathcal{L} = (\text{Objective function}) - (\mathbf{p}, (\text{Gov. Eqs})) - (\sigma, (\text{Additional constraints}))$$

The quantities \mathbf{p} and σ are called Lagrange multipliers and they are part of the final system of PDEs. The Lagrange multiplier \mathbf{p} , attached to the governing equations, will be computed as solution to a PDE similar to the original governing equations and is called the *adjoint* variable or the co-state variable.

Here we apply this method to two types of problems. One is finding optimal disturbances, that is structures in the flow that lead to final states with high energy while the other is designing controllers that when applied to a flow minimise the perturbation kinetic energy of the system.

Optimal disturbances

As mentioned above the first task is finding optimal disturbances. We are interested in two different types of disturbances. First we seek the initial condition $\mathbf{u}(0)$ that will have the maximum energy amplification at fixed time. Second we consider the spatial structure of the time-periodic forcing \mathbf{g} that creates the largest response at large times, that is when all transient effects have died out. Our analysis will therefore consider flow states induced by forcing or initial conditions, where a flow state is defined by the three-dimensional velocity vector field throughout the computational domain Ω at time t .

3.1. Initial condition

First we report the derivation relevant to the optimal initial condition. In this case we assume the forcing term \mathbf{g} in (2.8) to be zero, so that only the first term on the right end side of the formal solution (2.9) is of interest. We wish to determine the unit norm initial condition $\mathbf{u}(0)$ yielding the maximum possible energy $(\mathbf{u}(T), \mathbf{u}(T))$ at a prescribed time T . We define the objective function, as the the kinetic energy of the perturbations at time T ,

$$\mathcal{J} = (\mathbf{u}(T), \mathbf{u}(T)). \quad (3.1)$$

Formally, the task is to maximise the above quadratic measure subject to two constraints: the flow needs to satisfy the governing equations (2.8) (the linearised Navier-Stokes) (without forcing) and the initial condition must have unit norm $(\mathbf{u}(0), \mathbf{u}(0)) = 1$. By introducing Lagrange multipliers we may formulate an unconstrained optimisation problem for the functional

$$\mathcal{L}(\mathbf{u}, \mathbf{p}, \gamma) = (\mathbf{u}(T), \mathbf{u}(T)) - \int_0^T (\mathbf{p}, (\partial_t - \mathcal{A}) \mathbf{u}) \, d\tau - \gamma ((\mathbf{u}(0), \mathbf{u}(0)) - 1). \quad (3.2)$$

Therefore we need to determine \mathbf{u} , $\mathbf{u}(0)$, $\mathbf{u}(T)$, \mathbf{p} and γ such that \mathcal{L} is stationary, necessary condition for first order optimality. Finding the stationary points of \mathcal{L} is equivalent to solving the eigenvalue problem

$$\gamma \mathbf{u}(0) = \exp(\mathcal{A}^\dagger T) \exp(\mathcal{A} T) \mathbf{u}(0), \quad (3.3)$$

where $\exp(\mathcal{A}^\dagger T) \exp(\mathcal{A} T)$ is the forward and adjoint composite propagator whose leading eigenfunction is the optimal initial condition for time T . The iteration scheme above can be seen as a power iteration scheme finding the largest eigenvalue of the problem (3.3). The equations are solved iteratively as

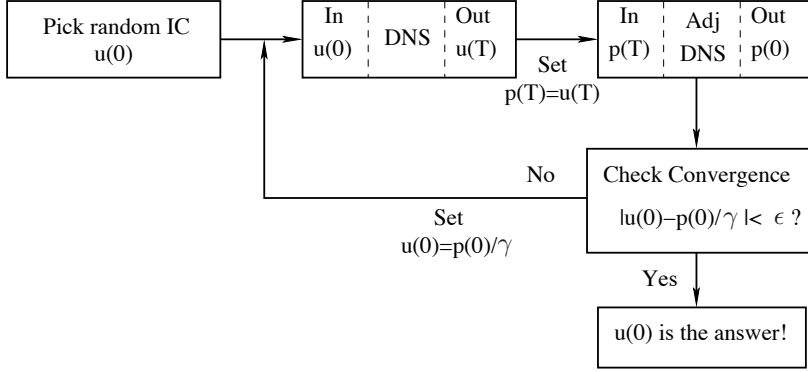


FIGURE 3.1. Power iterations scheme.

described in the block-diagram in figure (3.1). The method is applied in Paper 3.

Additionally the localised initial condition case is studied where a specific region in space is chosen and the optimal shape contained within the region is sought. A sample result is shown in figure (3.2). It is a three-dimensional localised optimal disturbance with target time $T = 1820$ along with the corresponding response. A disturbance similar to a TS-wave is apparent while the characteristic upstream-tilted structure is present in the initial condition. The wave-packet acquires a large initial growth while aligning itself with the wall-normal shear and continues to amplify as it travels downstream exploiting the convective instability of the blasius boundary layer. Finally, it experiences an energy growth of the order of 1700.

3.2. Forcing

This section will focus on the regime response of the system to time-periodic forcing. Since the formulation of the optimal forcing problem in this framework is novel we present the derivation of the new system more extensively. We assume zero initial conditions, $\mathbf{u}(0) = 0$, and periodic behaviour of the forcing function, *i.e.*

$$\mathbf{g} = \Re(\mathbf{f}(\mathbf{x}) \exp(i\omega t)), \quad \mathbf{f} \in \mathbb{C}, \quad \omega \in \mathbb{R}, \quad (3.4)$$

where \mathbf{f} is the spatial structure of the forcing, ω is its circular frequency and \Re denotes the real part. With these assumptions, the governing equations become

$$(\partial_t - \mathcal{A})\mathbf{u} - \Re(\mathbf{f} \exp(i\omega t)) = 0, \quad \mathbf{u}(0) = 0. \quad (3.5)$$

We wish to determine the spatial structure of the forcing \mathbf{f} with frequency ω in the limit of large times, that maximises the regime response of the flow. The measure of the optimum is again based on the energy norm. In order to formulate the optimisation problem we transform the problem in the frequency domain, thereby removing the time dependence. By assuming time periodic

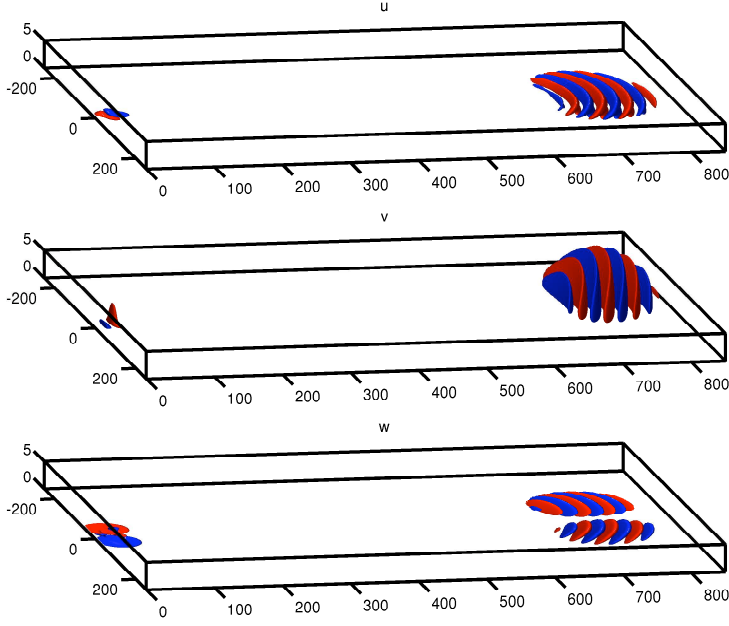


FIGURE 3.2. Optimal initial condition and response for 3d optimals for time $T = 1820$. For the corresponding amplitudes of each structure look at table 1 in Paper 3. Note that we plot both the disturbance and the response in the same figure since they are well separated in space. a) streamwise, b) wall-normal and c) spanwise component.

behaviour, \mathbf{u} is replaced by the complex field $\tilde{\mathbf{u}}$ so that

$$\mathbf{u} = \Re(\tilde{\mathbf{u}} \exp(i\omega t)). \quad (3.6)$$

The resulting governing equations can then be written

$$(i\omega\mathcal{I} - \mathcal{A})\tilde{\mathbf{u}} - \mathbf{f} = 0. \quad (3.7)$$

Note that the spatial operator \mathcal{A} remains unchanged. The objective function is the disturbance kinetic energy of the regime response and the Lagrange function is formulated as follows.

$$\mathcal{L}(\tilde{\mathbf{u}}, \tilde{\mathbf{p}}, \gamma, \mathbf{f}) = (\tilde{\mathbf{u}}, \tilde{\mathbf{u}}) - (\tilde{\mathbf{p}}, (i\omega\mathcal{I} - \mathcal{A})\tilde{\mathbf{u}} - \mathbf{f}) - \gamma((\mathbf{f}, \mathbf{f}) - 1). \quad (3.8)$$

The time behaviour of the co-state or adjoint variable is also assumed to be periodic

$$\mathbf{p} = \Re(\tilde{\mathbf{p}} \exp(i\omega t)). \quad (3.9)$$

Taking variations of \mathcal{L} with respect to $\tilde{\mathbf{u}}$, $\tilde{\mathbf{p}}$, \mathbf{f} and γ gives

$$\delta\mathcal{L} = \left(\frac{\partial\mathcal{L}}{\partial\tilde{\mathbf{u}}}, \delta\tilde{\mathbf{u}} \right) + \left(\frac{\partial\mathcal{L}}{\partial\tilde{\mathbf{p}}}, \delta\tilde{\mathbf{p}} \right) + \left(\frac{\partial\mathcal{L}}{\partial\mathbf{f}}, \delta\mathbf{f} \right) + \left(\frac{\partial\mathcal{L}}{\partial\gamma} \right) \delta\gamma. \quad (3.10)$$

Finally we set $\delta\mathcal{L} = 0$ and obtain a system of equations

$$\left(\frac{\partial\mathcal{L}}{\partial\tilde{\mathbf{p}}}\right) = 0 \rightarrow -(i\omega\mathcal{I} - \mathcal{A})\tilde{\mathbf{u}} + \mathbf{f} = 0, \quad (3.11)$$

$$\left(\frac{\partial\mathcal{L}}{\partial\tilde{\mathbf{u}}}\right) = 0 \rightarrow \tilde{\mathbf{u}} - (-i\omega\mathcal{I} - \mathcal{A}^\dagger)\tilde{\mathbf{p}} = 0, \quad (3.12)$$

$$\left(\frac{\partial\mathcal{L}}{\partial\gamma}\right) = 0 \rightarrow (\mathbf{f}, \mathbf{f}) - 1 = 0, \quad (3.13)$$

$$\left(\frac{\partial\mathcal{L}}{\partial\mathbf{f}}\right) = 0 \rightarrow \mathbf{f} = \gamma^{-1}\tilde{\mathbf{p}}. \quad (3.14)$$

Equations (3.11) and (3.12) provide the two equations we have to solve, while equation (3.13) gives the normalisation condition and (3.14) provides the optimality condition. It can be shown that the Lagrange multiplier technique corresponds to the standard matrix method when the resolvent norm is considered

$$\mathbf{f} = \frac{1}{\gamma}(-i\omega I - \mathcal{A}^\dagger)^{-1}(i\omega I - \mathcal{A})^{-1}\mathbf{f}. \quad (3.15)$$

The above formulation leads to matrix-free method for computing the pseudospectra of the given system. This is a new eigenvalue problem defining the spatial structure of the optimal forcing at frequency ω that is solved iteratively; the largest eigenvalue corresponds to the square of the resolvent norm

$$\gamma = \|(i\omega I - \mathcal{A})^{-1}\|^2. \quad (3.16)$$

The regime response for the direct and adjoint system is extracted from the numerical simulations by performing a Fourier transform of the velocity field during one period of the forcing.

The steps of the optimisation algorithm therefore are (similar to figure 3.1):

- (i) Integrate (3.5) forward in time and obtain the Fourier transform response $\tilde{\mathbf{u}}$ at the frequency of the forcing.
- (ii) $\tilde{\mathbf{u}}$ is used as a forcing for the adjoint system which in time domain is written

$$(-\partial_t - \mathcal{A}^\dagger)\tilde{\mathbf{p}} - \Re(\tilde{\mathbf{u}}\exp(i\omega t)) = 0. \quad (3.17)$$

- (iii) A new forcing function is determined by normalising $\mathbf{f}^{n+1} = \tilde{\mathbf{p}}/\gamma$.

- (iv) If $|\mathbf{f}^{n+1} - \mathbf{f}^n|$ is larger than a given tolerance, the procedure is repeated.

A sample result is shown in figure (3.3) relevant to the optimal forcing structure at spanwise wavenumber $\beta = 0.6$ and zero frequency. The wall-normal and spanwise components of the forcing are displayed in figure (3.3a) and b) while the streamwise component is very weak. In contrast the streamwise velocity component of the response is dominant while the other two components negligible (3.3c). In this case lift-up effect is the prevailing mechanism where counter-rotation vortices parallel to streamwise planes create streamwise streaks. This mechanism is characterised by strong component-wise energy transfer.

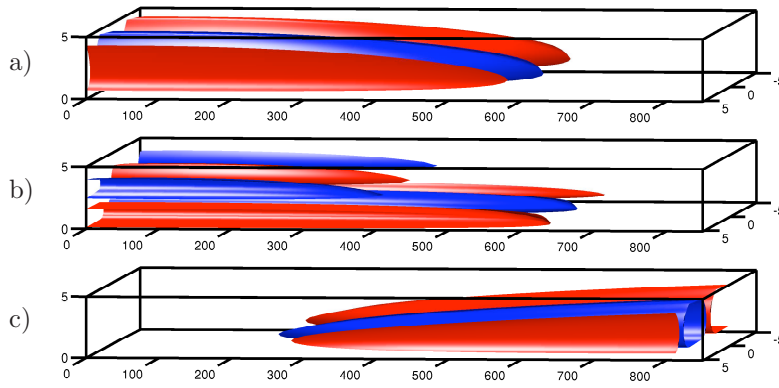


FIGURE 3.3. Isosurfaces of optimal forcing and response for the spanwise wavenumber $\beta = 0.6$ subject to steady forcing. a) Wall-normal component of optimal forcing structure. b) Spanwise component of optimal forcing. c) Streamwise velocity component of the flow response. Both the forcing structures and the response are elongated in the streamwise direction.

As for the initial condition, localised optimal forcing was also computed but in this case we were restricted to the spanwise periodic case due to the high computational cost. A specific region in the streamwise direction is chosen and the optimal shape contained within the region is sought.

Optimal Control

In this chapter we show how the Lagrange multiplier technique can be applied to solve the optimal control problem. The objective is disturbance attenuation and transition delay. The problem is divided into two distinct and self-contained problems. This is called the separation principle (Skogestad & Postlethwaite 2005). The first problem is full-information control where assuming full state knowledge of the flow a feedback control signal is computed. Full-state knowledge is a strong requirement and in order to relax it an estimator based on wall measurements is built. The combination of an estimator and a full information controller is called compensator, where the control law is based on the estimated flow.

4.1. Full-information Control

In this section the design process of the full information controller is presented. Therefore it is assumed that the exact state of the system is known. The state-space formulation is adopted,

$$\partial_t q = \mathcal{A}q + \mathcal{B}_1 w_1 + \mathcal{B}_2 \phi, \quad (4.1)$$

where $q = [v \ \eta \ \chi]^T$ is the new state variable. In relation to the previous section q can also be written as $q = [\mathbf{u} \ \chi]^T$ including χ , the velocity at the wall. $\mathcal{B}_1 w_1$ is the forcing due to external excitations w_1 of stochastic nature and $\mathcal{B}_2 \phi$ is the forcing from the control signal ϕ . The operator \mathcal{A} governs the dynamics of the augmented system (Chevalier *et al.* 2007a). The control is applied through non-homogeneous boundary conditions as a model for localised blowing and suction at the wall and a lifting procedure is adopted so that the formulation becomes compatible with the classical control theory where the control signal is expressed in the equations as a volume forcing (Högberg & Henningson 2002). In the case of full state-feedback control the signal is calculated directly from the state q so $\mathcal{B}_2 \phi = \mathcal{B}_2 \mathcal{K} q$ where \mathcal{K} is the control gain.

The aim is to compute the optimal control gain \mathcal{K} so that the kinetic energy of the mean-flow disturbances is minimised while at the same time the control effort is kept at low levels. To this end the following objective function is defined,

$$\mathcal{F} = \frac{1}{2} \int_0^T (q^H \mathcal{Q} q + \phi^* \mathcal{R} \phi) dt. \quad (4.2)$$

where $(\cdot)^*$ denotes the complex conjugate and $(\cdot)^H$ is the Hermitian transpose. The term $q^* \mathcal{Q} q$ corresponds to the kinetic energy of the perturbations where \mathcal{Q} is the energy norm operator. The second term in equation (4.2) represents the control effort where \mathcal{R} is the actuation penalty.

We apply the Lagrange multiplier technique to find the optimal solution to our problem. The Lagrangian is written as

$$\mathcal{L}(q, p, \phi) = \int_0^T \left[\frac{1}{2} (q^H \mathcal{Q} q + \phi^H \mathcal{R} \phi) - p (\partial_t q - \mathcal{A} q - \mathcal{B}_2 \phi) \right] dt, \quad (4.3)$$

where p is the Lagrange multiplier. The stochastic term $B_1 w_1$ is dropped since the deterministic approach is used for the full information control. The variation of the Lagrangian functional can be written as

$$\delta \mathcal{L} = \left(\frac{\partial \mathcal{L}}{\partial q} \right) \delta q + \left(\frac{\partial \mathcal{L}}{\partial p} \right) \delta p + \left(\frac{\partial \mathcal{L}}{\partial \phi} \right) \delta \phi. \quad (4.4)$$

Combining equations (4.3) and (4.4) and assuming $\delta \mathcal{L} = 0$ leads to the set of equations

$$\partial_t p + \mathcal{A}^H p + \mathcal{Q} q = 0 \quad (4.5a)$$

$$-\partial_t q + \mathcal{A} q + \mathcal{B}_2 \phi = 0 \quad (4.5b)$$

$$\mathcal{R} \phi + \mathcal{B}_2^H p = 0. \quad (4.5c)$$

A linear time dependent relation is assumed between the forward solution q and the Lagrange multiplier $p = \mathcal{X} q$. Inserting this assumption into equation 4.5a and adding equations 4.5a and 4.5c we arrive at the differential Riccati equation

$$\frac{\partial \mathcal{X}}{\partial t} + \mathcal{A}^H \mathcal{X} + \mathcal{X} \mathcal{A} - \mathcal{X} \mathcal{B}_2 \mathcal{R}^{-1} \mathcal{B}_2^H \mathcal{X} + \mathcal{Q} = 0. \quad (4.6)$$

The optimal \mathcal{K} is then given through the non-negative Hermitian solution \mathcal{X} of equation 4.6. A full derivation of the above equation is given by Lewis & Syrmos (1995). A simplified version arises if an infinite time horizon is assumed, yielding the steady-state Riccati equation

$$\mathcal{A}^H \mathcal{X} + \mathcal{X} \mathcal{A} - \mathcal{X} \mathcal{B}_2 \mathcal{R}^{-1} \mathcal{B}_2^H \mathcal{X} + \mathcal{Q} = 0. \quad (4.7)$$

with the control gain computed from

$$\mathcal{K} = -\mathcal{R}^{-1} \mathcal{B}_2^H \mathcal{Q} \mathcal{X}. \quad (4.8)$$

4.2. Estimation

The estimator is designed to approximate the full three-dimensional velocity field from wall measurements in real time. Measurements are taken from the wall and the signal includes noise from the sensors. The estimator can be seen as a filter operator, also termed Kalman filter, where the equations governing the flow are used for the filtering process. Input is the measurements from the real flow and output the estimated flow.

In the estimation problem two flow fields are considered: The 'real' flow and the estimated flow. All the quantities that correspond to the estimated flow are marked with a hat ($\hat{\cdot}$). The estimated field is assumed to fulfill the following equation

$$\frac{\partial \hat{q}}{\partial t} = \mathcal{A}\hat{q} - L(r - \hat{r}) + \mathcal{B}_2\phi, \quad (4.9)$$

where L is the measurement gain and r indicates the measurements. The latter are extracted through the measurement operator \mathcal{C} and since the measurements process introduces noise, we write $r = \mathcal{C}q + g$ and $\hat{r} = \mathcal{C}\hat{q}$, where g is the measurement noise. The following derivation provides with an operator L which optimally minimises the difference between the real and the estimated flow, namely the estimation error $\tilde{q} = q - \hat{q}$. The governing equation for \tilde{q} reads

$$\frac{\partial \tilde{q}}{\partial t} = (\mathcal{A} + LC)\tilde{q} + \mathcal{B}_1w_1 + Lg = \mathcal{A}_e\tilde{q} + \mathcal{B}_1w_1 + Lg. \quad (4.10)$$

We employ the stochastic approach instead of the deterministic used in the full-information control problem, since the equation is forced by stochastic inputs. We assume that the external disturbances w_1 and g are zero-mean stationary white noise Gaussian processes (Chevalier *et al.* 2007a). Since the system is forced by these stochastic processes, expected values of the relevant flow quantities are examined. In particular for the estimation problem the covariance of the estimation error \mathcal{P} (Kailath & Hassibi 2000) is considered and, as for the full information control, a steady state is assumed. The covariance of the error satisfies the algebraic Lyapunov equation

$$\mathcal{A}_e\mathcal{P} + \mathcal{P}\mathcal{A}_e^H + \mathcal{B}_1\mathcal{W}\mathcal{B}_1^H + L\mathcal{G}L^H = 0, \quad (4.11)$$

where \mathcal{W} and \mathcal{G} are the covariances of w_1 and g respectively. This equation along with the objective function, $\mathcal{F} = \tilde{r}^H\tilde{r}$ (amplitude of the measurement difference) form a new Lagrangian \mathcal{M} where the traces of the covariance matrices are involved. The trace of covariance matrices correspond to *rms* (root-mean-square) values of the quantity under consideration (Hoepffner *et al.* 2005).

$$\mathcal{M} = \text{trace}(\mathcal{P}Q) + \text{trace}[\Lambda(\mathcal{A}_e\mathcal{P} + \mathcal{P}\mathcal{A}_e^H + L\mathcal{G}L^H + \mathcal{B}_1\mathcal{W}\mathcal{B}_1^H)] \quad (4.12)$$

where Λ is the Lagrange multiplier. The first term in equation (4.12) is the objective function to be minimised and the second is the constraint coming from the Lyapunov equation satisfied by the covariance error. The Riccati equation that arises from optimising \mathcal{P} reads

$$\mathcal{A}\mathcal{P} + \mathcal{P}\mathcal{A}^H - \mathcal{P}\mathcal{C}^H\mathcal{G}^{-1}\mathcal{C}\mathcal{P} + \mathcal{B}_1\mathcal{W}\mathcal{B}_1^H = 0, \quad (4.13)$$

with the estimation feedback gain given by $L = -\mathcal{P}\mathcal{C}^H\mathcal{G}^{-1}$. For a similar derivation see also Bagheri *et al.* (2007). In this project the theory above is applied in a highly nonlinear case, where one may use the full (nonlinear) equations when solving the estimation problem (4.9) while the L is computed with the linear theory. This is the extended Kalman filter and it is expected to be more accurate than the standard Kalman filter.

4.3. Compensator

The compensator is the combination of full information control and state estimation. The measurements taken from the real flow are communicated to the estimator where they are used to compute the forcing needed to reproduce the perturbations present in the real flow. The actuation signal is computed from the estimated flow and it is applied to both the estimated and the real flow. Although both the control and estimation gains were computed for linear systems, the control and estimation is applied to the full nonlinear Navier-Stokes equations (Högberg *et al.* 2003c).

The model for the flow employed here is somewhat simplified in relation to the optimal disturbance case. A parallel base flow is assumed and thus the streamwise wavenumbers are decoupled. Hence we are able to apply a Fourier transform along both the wall-parallel directions. We can treat each wavenumber pair individually and instead of solving one problem with a large number of degrees of freedom, we solve many smaller systems. This necessity arises from the fact that we employ a matrix-based method to solve the Riccati equation which would be intractable for the global problem. This assumption stands as a good approximation due to the slow viscous growth of the boundary layer.

The compensator problem assumes that measurements are taken and actuation is applied continuously over the whole domain. This theory is applied to a spatial boundary layer and both measurements and actuation are available only on a part of the domain (see figure 2 in Paper 1). Two regions need to be specified, one for the control and one for the estimator. For both regions, the local laminar velocity profile is the base flow in the operator used to solve the problems introduced in the previous section. Once the control and estimation gains are calculated, the actuation forcing is limited to the actuation region by a smooth transfer function in physical space with two smooth step functions around the chosen locations (Chevalier *et al.* 2007a).

In figure 4.1 some sample results are shown. Figure 4.1a shows the wall-normal maximum of the *rms*-value of the streamwise velocity perturbation for the uncontrolled case and for both full information control and compensation. As observed, the growth of the the streaks is reduced within the control region. However, downstream of the control region, velocity fluctuations continue to grow. This can be explained by the presence of the free-stream turbulence above the boundary layer that is able to induce new perturbations inside the boundary layer.

4.4. Approaching the experiment

In this section we describe how we designed a numerical simulation that resembles the experiment done by Lundell (2007) in terms of flow case. Instead of the opposition control strategy used in the experiment we use the optimal control theory described above.

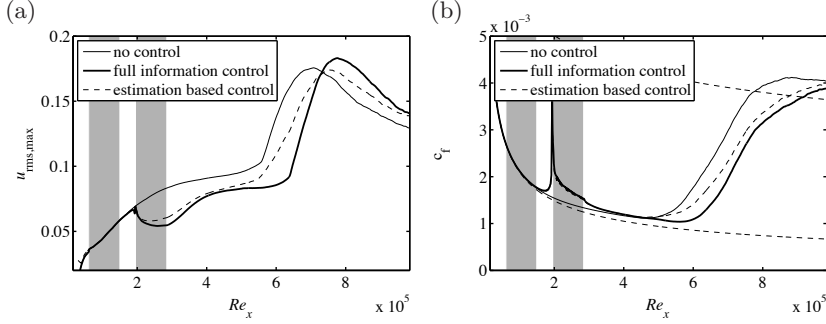


FIGURE 4.1. (a): Wall normal maximum u_{rms} ; (b): skin friction coefficient c_f . No control, —; Full information control, —; Compensator, - - - -. The shaded areas indicate the measurement and actuation region.

First we recall the differences between the actuator in the experiment and in the simulations. These pertain to the way the control signal is calculated and the area over which control is applied. In the experiment opposition control is adopted where the amplitude of the suction velocity and the time delay between the sensor and the actuator are varied. In the simulation an optimisation of the distributed control is performed and no further tuning is required. Note however that the control signal is computed assuming linearly evolving disturbances and parallel base flow. Secondly, it should be mentioned that the control is active over a large area of the plate where relatively weak blowing/suction is applied in the case of the numerical simulations. Conversely, small holes with strong suction velocity are used in the experiment. Further, in the simulation we apply control over the full spanwise width of the domain while in the experiment control sets are only stationed near the middle of the plate on an area about 20 mm wide.

These differences are reduced and further simulations were performed in order to study how much and if the two cases converge. The control strategy in terms of the way the control signal is calculated is not changed but the focus is put on the geometrical/functioning aspects of the actuator itself. In that context we first remove the blowing and keep only the suction. Then, we restrict the area of actuation to spanwise stripes and limit the streamwise extension of the area where suction is applied. Finally we employ a ‘cheaper’ control in order to obtain stronger suction to better mimic the experiment.

In figure 4.2 we show the streak growth and the efficiency of the control Ω from the simulation where all the previous restriction on the actuator have been applied. Ω is the relative decrease of the disturbance level in the boundary layer due to the control,

$$\Omega = 1 - \frac{u_{rms,max,on}}{u_{rms,max,off}}. \quad (4.14)$$

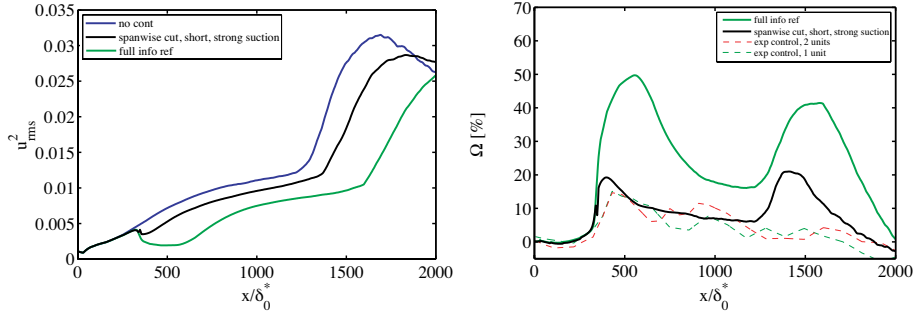


FIGURE 4.2. Wall-normal maximum of u_{rms} . Solid lines are simulations: blue: reference case, green line: control reference case, black line: control with only suction, spanwise and streamwise cut and cheaper control (stronger suction). Dashed lines from experiment.

In this case the control effect is almost the same for both the experiment and the simulation near the actuation region but downstream there is a delay of transition only for the numerical control. This can be explained by the fact that in the experiment, control is applied near the middle of the plate and when transition occurs, fully developed turbulence ‘invades’ the controlled area from the uncontrolled sides.

Summary of papers

Paper 1

DNS and LES of estimation and control of transition in boundary layers subject to free-stream turbulence.

In this paper optimal control is considered where transition to turbulence occurs in a flat-plate boundary-layer flow subjected to high levels of free-stream turbulence. This scenario is denoted bypass transition and is characterised by the non-modal growth of streamwise elongated disturbances called streaks. Linear feedback control is applied in order to reduce the perturbation energy and consequently delay transition. Control is applied by blowing and suction at the wall and it is both based on the full knowledge of the instantaneous velocity field (i.e. full information control) and on the velocity field estimated from wall measurements.

The control is able to delay the growth of the streaks in the region where it is active, which implies a delay of the whole transition process. The flow field can be estimated from wall measurements alone: The structures occurring in the ‘real’ flow are reproduced correctly in the region where the measurements are taken. Downstream of this region the estimated field gradually diverges from the ‘real’ flow, revealing the importance of the continuous excitation of the boundary layer by the external free-stream turbulence. Control based on estimation, termed compensator, is therefore less effective than full information control.

Paper 2

Feedback Control of Boundary Layer Bypass Transition: Experimental and Numerical Progress.

In this paper simulations of optimal feedback control have been performed for a flow configuration similar to that used by Lundell (2007) and disturbance attenuation as well as transition delay have been obtained. First, an effort is made to match the disturbance behaviour in the experimental flow case and in the simulation. Secondly control is applied in simulations of the matched system aiming at approaching the type of actuation used in the experiments (localised suction). Optimal feedback of the linear system is still the basis for computing the control signal. Remarkable agreement is obtained in terms of disturbance attenuation while the discrepancy in the transition delay can be

explained by the fact that in the experiment the controlled region was very narrow in the spanwise direction. Consequently, the controlled region is contaminated by turbulence from the sides.

Paper 3

Global optimal disturbances in the Blasius boundary-layer flow using time-steppers.

In this paper optimal disturbances are computed for the case of the flat-plate boundary-layer flow. Both the optimal initial condition leading to the largest growth at finite times and the optimal time-periodic forcing leading to the largest asymptotic response (pseudospectra) are considered. The Lagrange multiplier technique is employed with objective function the kinetic energy of the flow perturbations and constraints the linearised Navier–Stokes equations. Additionally optimal disturbances are computed within a localised framework which for some cases are more relevant to physical situations. In general two different type of disturbances are recovered; the first is relevant to the modal mechanism of a TS-wavepacket ignited by Orr-like structures and convectively amplifying due to the streamwise non-normality; the second is relevant to streamwise elongated disturbances, called streaks, generated by counter-rotating streamwise vortices associated with the strong component-wise transfer of energy due to the lift-up effect. It was found that the first mechanism(s) is more pronounced because of both the long computational domain and the relatively high Reynolds number considered here.

Conclusions and Outlook

Numerical simulations of flat-plate boundary-layer flows are performed. Linear optimal disturbances are computed and optimal control is applied at the case of the bypass transition. The Lagrange multiplier method is used with a quadratic objective function.

The optimal initial conditions leading to the largest possible energy amplification at time T and the optimal spatial structure of time-periodic forcing are considered. It is found that two mechanisms dominate the dynamics of this configuration. One corresponding to a combination of the Orr mechanism and the streamwise non-normality of the TS-wave and one to the lift-up inherent to spanwise wavelengths of the order of the boundary layer thickness. It is found that due to the long computational box and the relatively high inflow Reynolds number as well as due to the exponential-type of growth of the TS-wave the former has more potential for growth. However the later grows much faster and reaches its maximum sooner.

A linear-based feedback control is applied in order to delay transition, in a flow with highly nonlinear behaviour. The estimator and controller are designed within the Linear Quadratic Regulator (LQR) framework where a parallel base flow is assumed simplifying the computation of the gains. The results show that the control is able to reduce the energy of the streaks, responsible through their secondary instabilities for the considered bypass-transition scenario and thus delay the whole process. Both full-information and estimation-based control are tested. Control based on estimation is less effective than the full information control. The delay achieved is of order of the streamwise extent of the area where control is applied. Additionally numerical simulations are performed for a flow case analogous to the experiment performed by Lundell (2007). The control strategy differs but the rest of the features are kept as close as possible. Remarkable agreement is achieved in terms of disturbance attenuation.

Both of the studies presented in this work concern the relative restrictive geometry of the flat-plate boundary layer. This simplified flow case was chosen due to the importance of understudying processes acting on a fundamental level. Additionally a restriction was imposed by the specific code used (Chevalier *et al.* 2007b) allowing only for simple shear flows. At a next stage we are interested in exploring the optimisation tools developed so far in more complex geometries. Therefore another code is employed e.i. the **Nek5000** (Patera 1984; Tufo & Fischer 1999). This code is built based on the spectral element method, so

while retaining spectral accuracy it is more flexible allowing for the modelling of curved geometries. The aim is to apply the method to still rather generic geometries, simple enough to be able to accurately perform direct numerical simulations. For example two of the cases we intend to investigate in the near future are flow around a parabolic leading edge and through a diffuser.

Acknowledgements

The present thesis is the summary of about two and a half years of research in Prof. Dan Henningson's group at KTH Mechanics. This time has been invaluable for my knowledge of fluid mechanics but also enjoyable.

I would like to thank my supervisor Prof. Dan Henningson for being an endless source of inspiration. I would also like to thank to my co-advisor Prof. Luca Brandt who has always demonstrated immense patience but also astonishing brilliance when it comes to solving problems. Dr. Philipp Schlatter is also acknowledged for his valuable advises on the numerical tools. Many thanks to Dr. Espen Åkervik and Dr. Fredrik Lundell for a very rewarding cooperation. I am greatfull to David Tempelmann for many discussions and exchange of ideas.

Sharing office with Qiang Li, Johan Ohlsson and Onofrio Semeraro has been always a smooth and pleasant experience. Many thanks to the people of the group: Lars-Uve Schrader, Dr. Yohann Duguet, Shervin Bagheri and Dr. Stefan Ivanell. It has been great to work among interesting and fun people. Finally I would like to thank my family and friends for their lasting support and encouragement. I am grateful for the valuable comments of Prof. Carlo Cossu, Johan Ohlsson and Alica Selmanovic on this manuscript

The Swedish Research Council (Vetenskapsrådet) is gratefully acknowledged for funding this project.

This short paragraph is traditionally rounded off with a phrase in native language:

Αλήτσα, σου είμαι ευγνώμων για την αγάπη και αφοσίωση σου. Χωρίς εσένα τίποτα από όλα αυτά δεν θα ήταν κατορθωτό ... ♡

Bibliography

- BAGHERI, S., BRANDT, L. & HENNINGSON, D. S. 2009 Input-output analysis, model reduction and control of the flat-plate boundary layer. *J. Fluid Mech.* **620**, 263–298.
- BAGHERI, S., HOEPFFNER, J., SCHMID, P. J. & HENNINGSON, D. S. 2007 Input-output analysis and control design applied to a linear model of spatially developing flows. *Appl. Mech. Rev.* **62**(2) 020803
- CHEVALIER, M., HOEPFFNER, J., ÅKERVIK, E. & HENNINGSON, D. S. 2007a Linear feedback control and estimation applied to instabilities in spatially developing boundary layers. *J. Fluid Mech.* **588**, 163–187, 167–187.
- CHEVALIER, M., SCHLATTER, P., LUNDBLADH, A. & S., HENNINGSON D. 2007 A pseudo spectral solver for incompressible boundary layer flows. *Technical Report, Trita-Mek* **7**.
- HOEPFFNER, J., CHEVALIER, M., BEWLEY, T. R. & HENNINGSON, D. S. 2005 State estimation in wall-bounded flow systems. Part 1. Perturbed laminar flows. *J. Fluid Mech.* **534**, 263–294.
- HÖGBERG, M., BEWLEY, M. & HENNINGSON, D. S. 2003c Linear feedback control and estimation of transition in plane channel flow. *J. Fluid Mech.* **481**, 149–175.
- HÖGBERG, M. & HENNINGSON, D. S. 2002 Linear optimal control applied to instabilities in spatially developing boundary layers. *J. Fluid Mech.* **470**, 151–179.
- KAILATH, T. & HASSIBI, A. H. SAYED B. 2000 *Linear Estimation*. New Jersey: Prentice Hall.
- KREISS, G., LUNDBLADH, A. & HENNINGSON, D. S. 1994 Bounds for treshold amplitudes in subcritical shear flows. *J. Fluid Mech.* **270**, 175–198.
- LEWIS, F. L. & SYRMOS, V. L. 1995 *Optimal Control*. New York: Wiley-Interscience.
- LUNDELL, F. 2007 Reactive control of transition induced by free-stream turbulence: an experimental demonstration. *J. Fluid Mech.* **585**, 41–71.
- NORDSTRÖM, J., NORDIN, N. & HENNINGSON, D. S. 1999 The fringe region technique and the Fourier method used in the direct numerical simulation of spatially evolving viscous flows. *SIAM J. Sci. Comp.* **20**, 1365–1393.
- PATERA A. T. 1984 A Spectral Element Method for Fluid Dynamics: Laminar Flow in a Channel Expansion. *J. Comp. Phys.* **54**, 468–488.
- SCHMID, P. J. & HENNINGSON, D. S. 2001 *Stability and Transition in Shear Flows*. New York: Springer.

- SKOGESTAD, S. & POSTLETHWAITE, I. 2005 Multivariable feedback control, Analysis and Design, 2nd edition. *West Sussex: Wiley*.
- TREFETHEN, L. N., TREFETHEN, A. E., REDDY, S. C. & DRISCILL, T. A. 1993 Hydrodynamic stability without eigenvalues. *Science* **261**, 578–584.
- TUFO H. M. & FISCHER P. F. 1999 Terascale spectral element algorithms and implementations. *Supercomputing, ACM/IEEE 1999 Conference* , Portland, USA.

Part II

Papers

Paper 1

DNS and LES of estimation and control of transition in boundary layers subject to free-stream turbulence

By Antonios Monokrousos, Luca Brandt, Philipp Schlatter & Dan S. Henningson

Linné Flow Centre, Department of Mechanics
Royal Institute of Technology, SE-100 44 Stockholm, Sweden

International journal of heat and fluid flow, 29, Issue 3 841-855

Transition to turbulence occurring in a flat-plate boundary-layer flow subjected to high levels of free-stream turbulence is considered. This scenario, denoted bypass transition, is characterised by the non-modal growth of streamwise elongated disturbances. These so-called streaks are regions of positive and negative streamwise velocity alternating in the spanwise direction inside the boundary layer. When they reach large enough amplitudes, breakdown into turbulent spots occurs via their secondary instability. In this work the bypass-transition process is simulated using direct numerical simulations (DNS) and large-eddy simulations (LES). The ADM-RT subgrid-scale model turned out to be particularly suited for transitional flows after a thorough validation.

Linear feedback control is applied in order to reduce the perturbation energy and consequently delay transition. This case represents therefore an extension of the linear approach (Chevalier *et al.* 2007a) to flows characterised by strong nonlinearities. Control is applied by blowing and suction at the wall and it is both based on the full knowledge of the instantaneous velocity field (i.e. full information control) and on the velocity field estimated from wall measurements.

The results show that the control is able to delay the growth of the streaks in the region where it is active, which implies a delay of the whole transition process. The flow field can be estimated from wall measurements alone: The structures occurring in the “real” flow are reproduced correctly in the region where the measurements are taken. Downstream of this region the estimated field gradually diverges from the “real” flow, revealing the importance of the continuous excitation of the boundary layer by the external free-stream turbulence. Control based on estimation, termed compensator, is therefore less effective than full information control.

1. Introduction

The aim of this study is to perform numerical simulations to apply linear feedback control to transitional boundary-layer flows in the presence of free-stream turbulence where bypass transition occurs. An efficient pseudo-spectral numerical discretization is used and tools from modern control theory are incorporated into the controller design. Both large-eddy and direct numerical simulations are performed for evaluating the control efficiency in a highly nonlinear configuration.

1.1. Flow Control

Control of wall-bounded transitional and turbulent flows is the object of the present investigation owing to the high potential benefits. Any reduction of the skin friction, for example, implies relevant savings of the operational cost of commercial aircrafts and cargo ships. In particular the bypass transition scenario considered here is relevant in turbomachinery where high levels of free-stream turbulence are present.

Direct numerical simulations (DNS) have provided physical insight into the phenomena of transitional and turbulent flows, despite the fact that they are limited to simple and moderate Reynolds-number flows (Moin & Mahesh 1998). The same tools are now adopted to investigate the feasibility and performance of feedback control algorithms on a complex transitional flow case.

A linear model-based feedback control approach, that minimises an objective function which measures the perturbation energy, is formulated where the Orr-Sommerfeld and Squire equations model the flow dynamics. The latter equations describe the linear evolution of perturbations evolving in a parallel base flow. The requirement implicit in this formulation is the need of complete state information. However, the control problem can be combined with a state estimator to relax this requirement. The information problem is a limiting factor in the success of a control scheme, since, as a first step, it affects the whole procedure. The so-called Kalman and extended Kalman filter have been implemented in order to reconstruct the flow in an optimal manner by only considering wall measurements (Kailath & Hassibi 2000).

Flow control has been the object of comprehensive investigation the past years and recently, much effort has been put in the combination of computational fluid dynamics and control theory. While early attempts of flow control were based on physical intuition or on a trial-and-error basis, more systematic approaches are now followed. General reviews on flow control can be found in Moin & Bewley (1994), Joslin *et al.* (1996), Bewley (2001) and Kim & Bewley (2007) to mention a few.

Different control strategies have been attempted over the years for transitional flows, for example, wave cancellation where Tollmien-Schlichting waves are damped by applying anti-phase signals. Early reviews on the subject can be found in Thomas (1990) and Metcalfe (1994). Wave-cancellation methods for control were applied already in the 80es both experimentally (Thomas 1983)

and numerically, see e.g. Laurien & Kleiser (1989). A more 'drastic' control strategy, also known as laminar flow control, consists in stabilising the flow by applying strong suction on the boundary layer thus modifying the mean flow profile. A review on this method can be found in Joslin (1998). Nonlinear control methods have been studied as well and an overview of these methods is given by Joslin *et al.* (1997). In many cases nonlinear control is applicable only within the conditions and parameter range that it is designed for. An example of a robust controller that addresses that problem is described by Bewley *et al.* (2000). Other examples of application of nonlinear controllers are Berggren (1998), Bewley *et al.* (2001) and Collis *et al.* (2000).

The use of linear feedback controllers has been investigated more recently. This was motivated by the understanding on how the energy growth of fluctuations in a turbulent flow is related to linear mechanisms. In particular, Farrell & Ioannou (1996), Henningson (1996) and Kim & Lim (2000) showed that linear mechanisms are important to sustain turbulence and thus linear controllers can be applied for turbulence control. One early work on linear feedback control schemes is Joshi *et al.* (1995). Results from the application of linear optimal control theory also confirm the importance of linear mechanisms in the nonlinear flows under consideration (Högberg & Henningson 2002). Re-laminarisation of turbulent channel flow was achieved by Högberg *et al.* (2003a) with this method and the controller and estimator were combined by Högberg *et al.* (2003b). The combined control and estimation problem is also known as a "compensator".

Recent studies from our group on the application of model-based linear feedback control have shown the importance of physically relevant stochastic models for the estimation problem which turns out to be crucial for fast convergence (Hoepffner *et al.* 2005; Chevalier *et al.* 2006). Such stochastic noise needs to describe accurately enough the unmodelled dynamics, like uncertainties and nonlinearities. Based on these models the estimator is shown to work for both infinitesimal as well as finite amplitude perturbations in numerical simulations. The compensator has been applied to spatially developing boundary layers and shown to reduce the perturbation energy of both modal and non-modal disturbances (Chevalier *et al.* 2007a).

1.2. Bypass transition

Laminar-turbulent transition in a zero-pressure-gradient boundary layer subject to high levels of free-stream turbulence is considered. Such a scenario is usually referred to as bypass since the transition occurs bypassing the exponential growth of the Tollmien-Schlichting waves. It has indeed been shown both experimentally and theoretically that the asymptotic solutions given by the classical stability analysis are not always adequate to predict transition in wall-bounded shear flows. In some cases significant energy growth can be observed even when the flow is stable (Schmid & Henningson 2001). This can be explained by the non-normality of the the linearised operator describing the

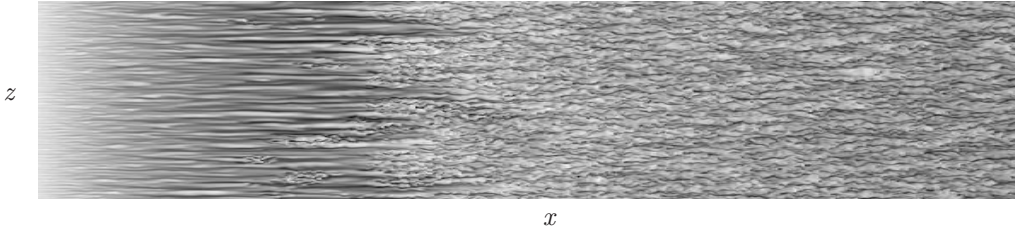


FIGURE 1. Visualisation of the streamwise disturbance velocity component (dark colour is low velocity, light high velocity) in a plane close to the wall showing the flow development under the influence of free-stream turbulence. Streamwise extent $Re_x = [32000, 570000]$, true aspect ratio. The streamwise extent corresponds to almost the full length of a typical turbine blade.

flow dynamics and the associated non-orthogonal set of eigenmodes (Reddy & Henningson 1993). If the state of the system has a strong projection on some of these highly non-orthogonal eigenmodes the energy of the flow can experience a significant transient growth. In the case of boundary layers, the upstream perturbations which undergo the largest possible growth consist of streamwise counter-rotating vortex pairs, see Andersson *et al.* (1999). These vortices lift low-momentum fluid from the wall and push high-momentum fluid from the outer parts towards the plate, thus creating elongated regions of alternating accelerated and decelerated fluid, called streaks. This process of vortex tilting is also known as lift-up effect (Landahl 1980).

After the primary energy growth due to the lift-up effect, the flow is in a more complicated laminar state where strong nonlinear interactions can come into play, leading to transition to turbulence. As the streaks grow in strength, they become susceptible to high-frequency secondary instabilities due to the presence of both wall-normal and spanwise inflectional velocity profiles (Brandt & Henningson 2002; Brandt 2007). These secondary instabilities manifest themselves in symmetric and antisymmetric streak oscillations, which are precursors to the formation of localised regions of chaotic swirly motion, the so-called turbulent spots (Brandt *et al.* 2004; Mans *et al.* 2007). The leading edge of a spot travels at about the free-stream velocity U_∞ while the trailing edge at half this speed. The spots become therefore more elongated and eventually merge: a fully-developed turbulent boundary layer is observed. A visualisation of the transition under free-stream turbulence from the simulations presented here is provided in figure 1. Streamwise streaks can be seen to form close to the computational inlet, followed by streaks oscillations and turbulent spots. The flow is turbulent in the second half of the domain.

The bypass transition scenario is observed when the boundary layer is subject to free-stream turbulence levels higher than 0.5-1% (Matsubara & Alfredsson 2001). As described above, the flow reproduces, though on a larger

scale, the near-wall dynamics of wall-bounded turbulence, see e.g. Robinson (1991), and it is therefore an ideal test configuration in view of possible control of turbulent flows. This work represents therefore a natural extension of the flow control studies mentioned above (Hoepffner *et al.* 2005; Chevalier *et al.* 2007a) to flows characterised by strong nonlinear interactions. An experimental demonstration of reactive control of the same scenario was recently presented by Lundell (2007). In this study, an *ad-hoc* threshold-and-delay control algorithm is evaluated and shown to inhibit the growth of the streamwise velocity fluctuations for a distance downstream of the actuator position.

The paper is organised as follows. In section 2 the control approach is presented while the numerical method, the large-eddy simulation and the free-stream turbulence generation are introduced in section 3. The results are presented in section 4. First, the focus will be on the validation of the LES while in the second part of section 4, linear feedback control applied to bypass transition is considered. The paper ends with a summary of the main conclusions.

2. Feedback control

Linear analysis is commonly used to understand the energy growth mechanisms of perturbations in shear flows (Schmid & Henningson 2001). However, it can also be used as a tool to design controllers that actively reduce the perturbation level and prevent or delay transition. The procedure adopted here is linear feedback control based on noisy measurements within the Linear Quadratic Gaussian (LQG) framework where a Linear Quadratic Regulator (LQR) is combined with a Kalman filter (Friedland 1986).

Within this framework a set of linear equations is used as a model for the physical process to be controlled along with a quadratic objective function. The system is assumed to be subject to Gaussian random excitations which represent unmodelled dynamics, e.g. nonlinearities. The control requires knowledge of the full state of the system. Therefore a state estimator, also called Kalman filter, is used to reconstruct the flow field from noisy measurements taken at the wall. To model uncertainties in the measurements, noise is assumed to contaminate the output signals. The control and estimation problem can be considered and solved separately and when combined it can be proven that this is the optimal solution (Skogestad & Postlethwaite 2005). This is known as the separation principle. Control can be applied both in the real and in the estimated flow. The combination of an estimator and a full information controller is called compensator.

The design of a controller aims at finding the optimal mapping between the various inputs and outputs of the system in such a way that a certain objective is obtained. In this case the system is the boundary layer flow, inputs are the external disturbances from the free stream (unknown) and the blowing/suction at the wall (known) while output is the wall measurements (known). The objective here is to reduce the kinetic energy of the perturbations in the flow.

2.1. *Control*

In this section the design process of the full information controller is presented. Therefore it is assumed that the exact state of the system is known.

To model the flow, the linearised Navier-Stokes equations are employed

$$\frac{\partial \mathbf{u}}{\partial t} + \mathbf{U} \nabla \mathbf{u} + \mathbf{u} \nabla \mathbf{U} = -\nabla \pi + Re^{-1} \nabla^2 \mathbf{u} \quad (1a)$$

$$\nabla \mathbf{u} = 0, \quad (1b)$$

where $\mathbf{u} = [u \ v \ w]^T$. The streamwise, wall-normal and spanwise directions are denoted x , y and z respectively, with the corresponding velocity components u , v and w and wavenumbers k_x , k_y and k_z .

In equations 1 we consider small perturbations around the base flow $\mathbf{U} = [U \ V \ W]^T$. To reduce the order of the system a parallel base flow is assumed $\mathbf{U} = [U(y) \ 0 \ 0]^T$ and under this assumption Fourier transform can be applied along the wall-parallel directions. Thus we can treat each wavenumber pair individually and instead of solving one problem with a large number of degrees of freedom, we solve many smaller systems. For the channel flow this assumption is exact, whereas for boundary layers, it is a good approximation due to their slow viscous growth.

To eliminate the pressure the wall-normal velocity v and wall-normal vorticity η formulation is adopted where the state is $(v \ \eta)^T$. The equations that describe the dynamics are the Orr-Sommerfeld/Squire (OSS) system (see Schmid & Henningson (2001))

$$\frac{\partial}{\partial t} \begin{pmatrix} v \\ \eta \end{pmatrix} = \begin{pmatrix} \mathcal{L}_{OS} & 0 \\ \mathcal{L}_C & \mathcal{L}_{SQ} \end{pmatrix} \begin{pmatrix} v \\ \eta \end{pmatrix} \quad (2)$$

where

$$\begin{aligned} \mathcal{L}_{OS} &= [\Delta]^{-1} [-ik_x U \Delta + ik_x D^2 U + \frac{1}{Re} \Delta] \\ \mathcal{L}_C &= -ik_z D U \\ \mathcal{L}_{SQ} &= -ik_x U + \frac{1}{Re} \Delta. \end{aligned} \quad (3)$$

U is the mean-flow profile, the similarity Blasius solution, Δ is the Laplacian operator $\Delta = D^2 - k^2$ with $k^2 = k_x^2 + k_z^2$ and D the wall-normal derivative. The Reynolds number Re is defined using the free-stream velocity U_∞ and the local boundary-layer displacement thickness δ^* ,

$$Re = \frac{U_\infty \delta^*}{\nu}. \quad (4)$$

The control is applied through non-homogeneous boundary conditions as a model for localised blowing and suction at the wall. To adopt the same formulation as in classical control theory, the control signal is expressed in the equations as a volume forcing by a lifting procedure (Högberg & Henningson 2002). To account for non-modelled dynamics, such as non-parallel effects and nonlinearities, external excitation is added such that two extra forcing terms

appear in the equations

$$\frac{\partial \mathbf{q}}{\partial t} = \mathcal{A} \mathbf{q} + \mathcal{B}_1 \mathbf{w}_1 + \mathcal{B}_2 \psi, \quad (5)$$

where $\mathbf{q} = [v \ \eta \ \chi]^T$, $\mathcal{B}_1 \mathbf{w}_1$ is the forcing due to external excitations \mathbf{w}_1 of stochastic nature and $\mathcal{B}_2 \psi$ is the forcing from the control signal ψ and χ is the velocity at the wall. We thus have $\partial \chi / \partial t = \psi$. The operator \mathcal{A} governs the dynamics of the augmented system (Chevalier *et al.* 2007a). Note that the control signal is the time derivative of the blowing and suction at the wall. In the case of full state-feedback control the signal is calculated directly from the state \mathbf{q} so $\mathcal{B}_2 \psi = \mathcal{B}_2 \mathcal{K} \mathbf{q}$ where \mathcal{K} is the control gain.

The aim is to calculate the control gain \mathcal{K} so that the kinetic energy of the mean-flow disturbances is minimised while at the same time the control effort is kept at low levels. To this end the following objective function is defined,

$$\mathcal{F} = \int_0^T (\mathbf{q}^* \mathcal{Q} \mathbf{q} + \psi^* \mathcal{R} \psi) dt. \quad (6)$$

where $(\cdot)^*$ denotes the complex conjugate. The term $\mathbf{q}^* \mathcal{Q} \mathbf{q}$ corresponds to the kinetic energy of the perturbations for the specific wavenumber pair under consideration where \mathcal{Q} is the energy norm operator. The second term in equation 6 represents the control effort, $\mathcal{R} = l^2$ where l is the actuation penalty.

As a next step we discretise the problem so that it can be solved numerically. The control problem is now redefined as a set of one-dimensional partial differential equations, one for each wavenumber pair. Along the wall-normal direction y , Chebyshev polynomials are used. In the case of unbounded domains the corresponding wall-parallel wavenumbers are a continuous set but in a bounded domain this set becomes discrete and the corresponding Fourier representation transforms from integrals into series. The series will be truncated to a wavenumber that corresponds to the resolution of the numerical simulation.

If q is the discrete state vector the energy norm operator Q is defined in such a way that the quantity $q^H Q q$ approaches the kinetic energy of the system as the resolution increases. q^H is the Hermitian transpose of q .

The discretised system has a similar form as the continuous one

$$\frac{\partial q}{\partial t} = A q + B_1 w_1 + B_2 \phi, \quad (7)$$

where the quantities q , A , B_1 , w_1 , B_2 and ϕ are the equivalent discrete counterparts of \mathbf{q} , \mathcal{A} , \mathcal{B}_1 , \mathbf{w}_1 , \mathcal{B}_2 and ψ .

We use the Lagrange multipliers to find the optimal solution to our problem. We define the Lagrangian

$$\mathcal{L} = \int_0^T \left[\frac{1}{2} (q^H Q q + \phi^H R \phi) - p \left(\frac{\partial q}{\partial t} - A q - B_2 \phi \right) \right] dt, \quad (8)$$

where p is the Lagrange multiplier and R is the discrete versions of \mathcal{R} . Here we have dropped the stochastic term $B_1 w_1$ since we will use the deterministic approach in deriving the full information control. The variation of the Lagrangian functional can be written as

$$\delta\mathcal{L} = \left(\frac{\partial\mathcal{L}}{\partial q}\right)\delta q + \left(\frac{\partial\mathcal{L}}{\partial p}\right)\delta p + \left(\frac{\partial\mathcal{L}}{\partial\phi}\right)\delta\phi. \quad (9)$$

Combining equations 8 and 9 and assuming $\delta\mathcal{L} = 0$ leads to the set of equations

$$\frac{\partial\mathcal{L}}{\partial q} = \frac{\partial p}{\partial t} + A^H p + Qq = 0 \quad (10a)$$

$$\frac{\partial\mathcal{L}}{\partial p} = -\frac{\partial q}{\partial t} + Aq + B_2\phi = 0 \quad (10b)$$

$$\frac{\partial\mathcal{L}}{\partial\phi} = R\phi + B_2^H p = 0. \quad (10c)$$

A linear time dependent relation is assumed between the forward solution q and the Lagrange multiplier $p = Xq$. Inserting this assumption into equation 10a and adding equations 10a and 10c we arrive at the differential Riccati equation

$$\frac{\partial X}{\partial t} + A^H X + XA - XB_2R^{-1}B_2^H X + Q = 0. \quad (11)$$

The optimal K is then given through the non-negative Hermitian solution X of equation 11. A full derivation of the above equation is given by Lewis & Syrmos (1995). A simplified version arises if an infinite time horizon is assumed, yielding the steady-state Riccati equation

$$A^H X + XA - XB_2R^{-1}B_2^H X + Q = 0. \quad (12)$$

with the control gain computed from

$$K = -R^{-1}B^H QX. \quad (13)$$

The Riccati equation is solved for each streamwise and spanwise wavenumber pair (k_x, k_z) separately and an inverse Fourier transform can be applied to visualise the control gains in physical space. It is shown by Högberg & Henningson (2002) that the control gains, relating the velocity perturbations to the control signal, are spatially localised: The control is thus dependent only on the perturbations in a limited region located upstream of the actuator.

2.2. Estimation

The duty of the estimator is to approximate the full three-dimensional velocity field from wall measurements in real time. Measurements are taken from the wall and the sensors responsible for the measurements include noise. The estimator can be seen as a filter operator where the equations governing the flow are used for the filtering process. Input is the measurements from the real flow and output the estimated flow. This is often called Kalman filter.

In the estimation problem two flow fields are considered: The 'real' flow and the estimated flow (see figure 2). All the quantities that correspond to the estimated flow are marked with a hat ($\hat{\cdot}$).

The estimated field is assumed to fulfill the following equation

$$\frac{\partial \hat{q}}{\partial t} = A\hat{q} - L(r - \hat{r}) + B_2\phi, \quad (14)$$

where L is the measurement gain and r indicates the measurements. The latter are extracted through the measurement operator C and since the measurements process introduces noise, we write $r = Cq + g$ and $\hat{r} = C\hat{q}$, where g is the measurement noise. The governing equation for the estimation error can be written as

$$\frac{\partial \tilde{q}}{\partial t} = (A + LC)\tilde{q} + B_1w_1 + Lg = A_e\tilde{q} + B_1w_1 + Lg. \quad (15)$$

The aim of the estimation problem is to minimise the difference between the real and the estimated flow, namely the estimation error $\tilde{q} = q - \hat{q}$. From the equations above the mathematical similarity between the feedback control and the estimation problem is evident. We are looking for the optimal L for which the objective function $\mathcal{F} = \tilde{r}^H \tilde{r}$ is minimised. However in this case we have to use the stochastic approach instead of the deterministic, since the equation is forced by stochastic inputs.

We assume that the external disturbances w_1 and g are zero-mean stationary white noise Gaussian processes (Chevalier *et al.* 2007a). Since the system is forced by these stochastic processes, expected values of the relevant flow quantities are examined. In particular for the estimation problem the covariance of the estimation error P is considered and, as for the full information control, a steady state is assumed. The covariance of the error satisfies the algebraic Lyapunov equation

$$A_e P + P A_e^H + B_1 W B_1^H + L G L^H = 0, \quad (16)$$

where W and G are the covariances of w_1 and g respectively. This along with the objective function \mathcal{F} form a new Lagrangian \mathcal{M} where the traces of the covariance matrices are involved. The trace of covariance matrices correspond to *rms* (root-mean-square) values of the quantity under consideration (Hoepffner *et al.* 2005).

$$\mathcal{M} = \text{trace}(PQ) + \text{trace}[\Lambda(A_e P + P A_e^H + L G L^H + B_1 W B_1^H)] \quad (17)$$

where Λ is the Lagrange multiplier. The first term in equation 17 is the objective function to be minimised and the second is the constraint coming from the Lyapunov equation satisfied by the covariance error. At the stationary point of \mathcal{M}

$$\frac{\partial \mathcal{M}}{\partial P} = Q + (A + LC)^H \Lambda + \Lambda^H (A + LC) = 0 \quad (18a)$$

$$\frac{\partial \mathcal{M}}{\partial \Lambda} = (A + LC)P + P(A + LC)^H + B_1 W B_1^H + L G L^H = 0 \quad (18b)$$

$$\frac{\partial \mathcal{M}}{\partial L} = 2\Lambda(PC^H + LG) = 0. \quad (18c)$$

The solution to this optimisation problem is given by the numerical solution P of a Riccati equation similar to that arising in the feedback control problem

$$AP + PA^H - PC^H G^{-1} CP + B_1 W B_1^H = 0, \quad (19)$$

with the estimation feedback gain given by $L = -PC^H G^{-1}$. For a similar derivation see also Bagheri *et al.* (2007).

In the computations presented, three quantities are measured at the wall, namely the streamwise and spanwise skin friction and the pressure

$$\tau_x = \tau_{xy}|_{wall} = \frac{1}{Re} \frac{\partial u}{\partial y} \Big|_{wall} \quad (20a)$$

$$\tau_z = \tau_{zy}|_{wall} = \frac{1}{Re} \frac{\partial w}{\partial y} \Big|_{wall} \quad (20b)$$

$$p_{wall} = \Delta_{xz}^{-1} \left(\frac{1}{Re} \frac{\partial^3 v}{\partial y^3} \right) \Big|_{wall} \quad (20c)$$

where Δ_{xz}^{-1} denotes the formal inverse of the wall-parallel Laplacian.

The Kalman filter presented here is the optimal estimation in a linear setting. To apply the above theory in a highly nonlinear case, one may use the full (nonlinear) equations when solving the estimation problem 14 while the gains used are computed with the linear theory. This is the extended Kalman filter and it is expected to be more accurate than the standard Kalman filter.

2.3. Compensator

The compensator is the combination of full information control and state estimation. The measurements taken from the real flow are communicated to the estimator where they are used to compute the forcing needed to reproduce the perturbations present in the real flow. The actuation signal is computed from the estimated flow and it is applied to both the estimated and the real flow. Although computed for linear systems, the control and estimation are applied to the full nonlinear Navier-Stokes equations (Högberg *et al.* 2003c).

The compensator problem as it was stated here accounts only for parallel flows as there is no explicit streamwise dependence in the OSS operator. Further, it assumes that measurements are taken and actuation is applied continuously over the whole domain. This theory is applied to a spatial boundary layer and both measurements and actuation are available only on a part of the domain (see figure 2). Two regions need to be specified, one for the control and one for the estimator. For both regions, the local laminar velocity profile is used as a base flow in the OSS operator. The flow is assumed to be locally parallel around these locations in order to solve the control and estimation problems. Once the control and estimation gains are calculated, the actuation forcing is limited to the actuation region by a smooth transfer function in physical space

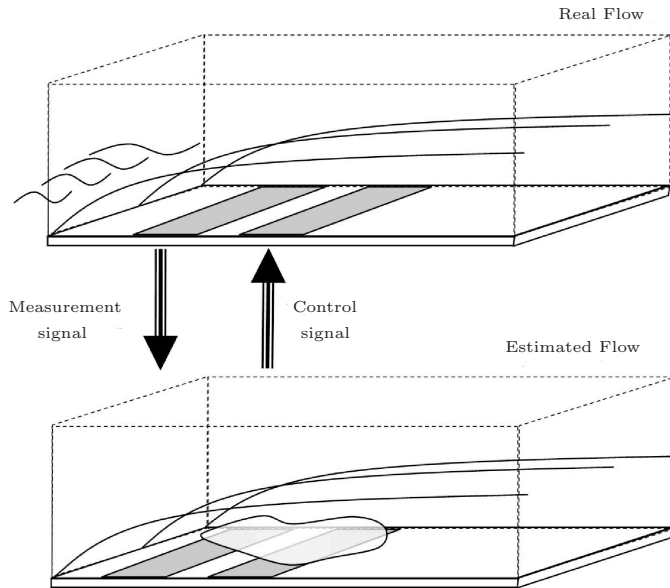


FIGURE 2. A schematic drawing of the compensator. Wall measurements are taken in the real flow and compared to those from the estimator. The control signal is computed based on the reconstructed velocity field and applied in the real flow.

with two smooth step functions around the chosen locations (Chevalier *et al.* 2007a).

3. Simulation approach

3.1. Numerical method

For the present computations, the three-dimensional, time dependent, incompressible Navier-Stokes equations are solved using a spectral method (Chevalier *et al.* 2007b). The algorithm uses Fourier representation in the streamwise and spanwise directions and Chebyshev polynomials in the wall-normal direction, together with a pseudo-spectral treatment of the nonlinear terms. Dealiasing using the 3/2-rule is employed in the wall-parallel (Fourier) directions, whereas a slightly increased resolution is used in the wall-normal direction to reduce aliasing errors. The time is advanced with a four-step low-storage third-order Runge-Kutta method for the nonlinear terms and all the forcing contributions, and a second-order Crank-Nicolson scheme for the linear terms and boundary conditions. To correctly account for the downstream boundary-layer growth the spatial simulation approach is necessary. This requirement is combined with the periodic streamwise boundary condition by the implementation of a *fringe* region (Nordström *et al.* 1999; Lundbladh *et al.* 1999). In this region,

positioned at the downstream end of the computational box occupying approximately 10% of the flow domain, a volume forcing is smoothly raised from zero to force the flow from the outflow to the desired inflow condition. The inflow consists of the laminar Blasius boundary layer with superimposed spatially and temporally varying disturbances, i.e. the free-stream turbulence in the present case.

3.1.1. *MPI implementation and performance*

The numerical code described above is parallelised to run on distributed-memory architectures (i.e. clusters) using the Message Passing Interface (MPI). As detailed in section 2.3, the simulation of the estimator and compensator actually requires the time-advancement of two flow fields, i.e. the “real” flow field and the estimated field. These two fields are coupled by the measurements and the control actuation (in case of compensator), and feature different inflow conditions and may have different spatial resolution and domain size. In the present implementation this is achieved by having two simulations running simultaneously on a subset of the available processors; the two simulations have two different executables, compiled with different options but running within the same MPI environment. Information exchange is then accomplished using distinct messages sent between the two codes. Details on the implementation can be found in Seyed (2007).

To give an estimate of the computational cost, the details of a typical simulation are now outlined. The “real” flow is simulated via direct numerical simulation (DNS) discretised on a domain with approximately $20 \cdot 10^6$ grid points. The corresponding estimator simulation can be run as a large-eddy simulation (LES) (see section 3.2 below) with a lower resolution of approximately $2.5 \cdot 10^6$ grid points. In this example, the DNS is run on 24 processors, and the estimator LES on 6 processors, i.e. employing a total of 30 processors. The necessary runtime in order to obtain fully converged statistics (simulated time $\Delta t = 4000$) is about 300 hours on 30 processors corresponding to 9000 CPU hours.

3.2. *Sub-grid scale modelling*

The fine grids (and the corresponding small time steps) necessary in the DNS of turbulent flows at moderate to high Reynolds numbers give rise to very high computational costs. Therefore, other approaches based on large-eddy simulations (LES) have been developed to be able to simulate transitional and turbulent flows in large-enough domains and at high Re . In LES the mesh size is chosen considerably larger than for DNS. This implies that the structures present in the flow are only resolved above a certain size corresponding to the cutoff wavenumber $\omega_{c,grid}$. This length scale is chosen to be small enough to capture well the structures that are involved in the physical phenomena under investigation. On the other hand, the scales below the cutoff scale are not resolved on the numerical grid, but their influence due to nonlinearity onto

the resolved scales must be modelled by a subgrid-scale (SGS) model. For flows with solid walls, the thin boundary layers adjacent to the walls need to be resolved in both DNS and LES for accurate results. Therefore, even LES requires a substantial computational effort, albeit lower than DNS: A typical resolution for an LES is approximately 1-20% of a corresponding fully-resolved DNS.

Formally, the solution in an LES calculation is obtained by applying a generic low-pass filter G^P with a certain filter width Δ suitable for the problem under consideration,

$$\bar{u}_i(x) := G^P * u_i := \int_{\mathcal{V}} G^P(x, x', \Delta) u_i(x') dx' , \quad (21)$$

where $\bar{u}_i(x)$ denotes the filtered quantity and \mathcal{V} the computational domain. G^P is referred to as the primary LES filter. The governing momentum equations for the filtered quantities become

$$\frac{\partial \bar{u}_i}{\partial t} + \frac{\partial \bar{u}_i \bar{u}_j}{\partial x_j} = - \frac{\partial \bar{p}}{\partial x_i} - \frac{\partial \tau_{ij}}{\partial x_j} + \frac{1}{Re} \frac{\partial^2 \bar{u}_i}{\partial x_j \partial x_j} \quad (22)$$

together with filtered incompressibility constraint

$$\frac{\partial \bar{u}_i}{\partial x_i} = 0 . \quad (23)$$

The interaction between the resolved and unresolved scales is given by the SGS stresses,

$$\tau_{ij} = \overline{u_i u_j} - \bar{u}_i \bar{u}_j , \quad (24)$$

which is an unclosed term and thus has to be modelled based on the filtered velocity field \bar{u}_i . In most LES approaches the primary filter is not applied explicitly, but rather given by the implicit filter due to the lower grid resolution.

The ADM-RT model used here acts on the velocity components directly. The model employs the relaxation term proposed in the context of the approximate deconvolution model (ADM) (Stolz & Adams 1999). It has been shown in e.g. Schlatter *et al.* (2006a,b) that for spectral simulations the deconvolution operation applied in the ADM approach is not necessary. Therefore, the SGS force due to the ADM-RT model is given by (Schlatter *et al.* 2004)

$$\frac{\partial \tau_{ij}}{\partial x_j} = \chi H_N * \bar{u}_i , \quad (25)$$

with χ being the model coefficient. H_N denotes a high-order three-dimensional high-pass filter (Stolz *et al.* 2001), and the symbol $*$ stands for convolution in physical space, i.e. a multiplication with the respective transfer function \hat{H}_N in Fourier space.

The high-pass filter H_N used in the present work is obtained by the repeated application of a low-pass filter G according to

$$H_N = (I - G)^{N+1} , \quad N > 0 . \quad (26)$$

Typically, G is chosen as the low-order low-pass filter suggested by Stolz *et al.* (2001). The cutoff frequency is defined as $\hat{G}(\omega_c) = 1/2$ and can be adjusted. For the present results, $\omega_c = 2\pi/3$ and $N = 5$. H_N is at least of order $r(N+1)$ with r being the order of G . The latter is at least $r = 3$ on non-equidistant grids.

χ is the model coefficient which is set to a constant value herein motivated by previous studies showing little dependency of the results on the actual value of the coefficient (see e.g. Schlatter *et al.* (2006b)). If the model coefficient χ is chosen inversely proportional to the time-step size the relaxation term has a similar effect as a filtering of the velocities after every time step, as mentioned in Stolz & Adams (1999).

The relaxation term $\chi H_N * \bar{u}_i$ is proportional to the small-scale velocity fluctuations in the flow field. Therefore, it will damp out these oscillations leading to a drain of kinetic energy from the smallest resolved scales.

The ADM-RT model proved to be accurate and robust in predicting transitional and turbulent incompressible flows with spectral methods (Schlatter *et al.* 2004, 2006b). Note that the relaxation-term model is related to the spectral vanishing viscosity approach (Karamanos & Karniadakis 2000). Due to the high-order filter H_N with a cutoff frequency of $\omega_c \approx 0.86\pi$ only the smallest represented eddies are affected, whereas the larger, energy-carrying scales are not directly influenced by the model contributions.

3.3. Free-stream turbulence generation

The boundary layer considered here is subject to external disturbances, in particular free-stream turbulence. To generate this inflow a superposition of eigenmodes from the continuous spectrum of the OSS operator is used (Jacobs & Durbin 2001; Brandt *et al.* 2004). In the present implementation disturbances can be introduced in the flow in three different ways: forcing them in the fringe region, with a body force as in the estimation problem, or via blowing and suction at the wall by a non-homogeneous boundary condition as done in the control problem. The free-stream turbulence is forced at the inflow by adding the modes to the laminar base-flow profile in the fringe region.

Detailed description of the procedure adopted can be found in Brandt *et al.* (2004). Here the free-stream generation is shortly outlined. A three-dimensional wave vector $\mathbf{k} = (k_x, k_y, k_z)$ is associated to each eigenfunction of the continuous spectrum where, k_x and k_z are defined by the normal-mode expansion along the wall-parallel directions of the underlying linear problem while the wall-normal wavelength is determined by the eigenvalue along the continuous spectrum. If Taylor's hypothesis is applied the streamwise wavenumber k_x can be replaced by a frequency $\omega = k_x U_\infty$ and the disturbance signal is written as

$$u_{dist} = \sum A_N \hat{u}_N(y) e^{ik_z z + ik_x x - i\omega t}, \quad (27)$$

where the wall-normal wavenumber k_y is implicit in the shape of the eigenfunction $\hat{u}_N(y)$ (Grosch & Salwen 1978). The complex wavenumber k_x is determined

by the dispersion relation once the real wall-normal wavenumber k_y and the real wavenumbers k_z and ω are selected according to the procedure described below. The wavenumbers pertaining to the modes used in the expansion are selected by defining a number of spherical shells of radius $|k|$ in the wavenumber space (ω, k_y, k_z) . 40 points are then placed at equal intervals on the surface of these spheres. The coordinates of these points define the wavenumbers of the modes used in the expansion above. The complex coefficients A_N provides random phase but a given amplitude. The amplitude $|A_N|$ is in fact the same for all modes on each shell and is chosen to reproduce the Von Kármán spectrum

$$E(k) = \frac{2}{3} \frac{a(kL_I)^4}{(b + (kL)^2)^{17/6}} L_I Tu. \quad (28)$$

This spectrum is for large scales asymptotically proportional to k^4 , whereas it matches the Kolmogorov-(5/3)-law for small scales. In the expression above, Tu is the turbulence intensity, L_I is a characteristic integral length scale such that $k_{max} = 1.8/L_I$ where k_{max} is the wavenumber of maximum energy and a , b two normalisation constants.

3.3.1. Free-stream turbulence generation in the LES

Due to the lower resolution employed for the LES runs, the imposed turbulence spectrum at the inlet has to be adapted. To obtain results that are as close to the DNS as possible, it was decided to use exactly the same set of modes and the same random phases on all the various grids, without any modification of the turbulence intensity level at the inlet. Modes with wavenumbers too large to be resolved on a given coarser LES grid were discarded and consequently not forced at the inlet. All the other parameters specifying the inlet spectrum, i.e. length scale, choice of modes and the individual scaling of the modes, are the same on all grids. This leads to the observation that the measured turbulence intensity at the inlet is smaller for coarser grids, because less modes are actually forced. To obtain the true Tu one had to also include the unresolved fluctuations, which are however not available during an LES. The results show that the transition process is not crucially influenced by that difference in inlet Tu . If, on the other hand, the resolved Tu at the inlet is adapted to exactly match the level on the finest (i.e. DNS) grid, premature transition corresponding to the higher turbulence levels is observed. The explanation for this behaviour is that the receptivity of the boundary layer is mainly dominated by low-frequency modes of the free stream. The amplitudes of these modes, which are resolved on both the DNS and LES grids, should therefore not be modified.

3.4. Simulation parameters

The parameters defining the problem are the Reynolds number, the intensity and the integral length scale of the free-stream turbulence and the size of the computational box. The inflow Reynolds number $Re_{\delta_0^*}$, defined using the displacement thickness of the boundary layer at the inflow of the computational domain, was chosen to be 300 for all cases under consideration.

TABLE 1. Different computational boxes used. Resolution for each box dimensions and type of simulation. The box dimensions include the fringe region and are non-dimensionalised with respect to the displacement thickness δ_0^* at the inflow ($Re_{\delta_0^*} = 300$)

Box	Method	$L_x \times L_y \times L_z$ δ_0^*	$N_x \times N_y \times N_z$ (<i>resolution</i>)
Small	DNS	$1000 \times 60 \times 50$	$1024 \times 121 \times 72$
Small	LES	$1000 \times 60 \times 50$	$256 \times 121 \times 36$
Medium	LES	$2000 \times 60 \times 90$	$512 \times 121 \times 64$
Large	LES	$2000 \times 60 \times 180$	$512 \times 121 \times 128$
X-Large	LES	$4000 \times 60 \times 180$	$1024 \times 121 \times 128$

The different computational boxes used are reported in table 1. Direct numerical simulations were only performed in the small box, while the largest boxes were used to allow the transition to turbulence to occur within the computational domain. The latter computational domains are thus used for the parametric study of bypass transition and its control. The medium-size box was used when investigating the influence of limiting the control signal (see section 4.2.1).

The code was run in four different modes, corresponding to four different physical problems: no control (used as reference case), full information control, estimation without control and compensator, i.e. control based on estimation.

4. Results

Based on the theory and numerical methods presented in the previous sections, simulations of transition in a flat-plate boundary layer subject to free-stream turbulence are performed. Linear feedback control is then applied to the flow in order to delay transition. Both LES and DNS are presented here and all the statistics presented are obtained by averaging in time and in the spanwise direction.

In the following results the streamwise coordinate is indicated by the Reynolds number based on the the distance from the leading edge

$$Re_x = \frac{U_\infty x}{\nu} = \frac{Re_{\delta_0^*}^2}{1.7208}, \quad (29)$$

where the value of δ^* for the laminar Blasius solution is used. All the quantities presented are non-dimensionalised with the free-stream velocity, U_∞ , the viscosity, ν and the displacement thickness at the inflow of the computational domain δ_0^* .

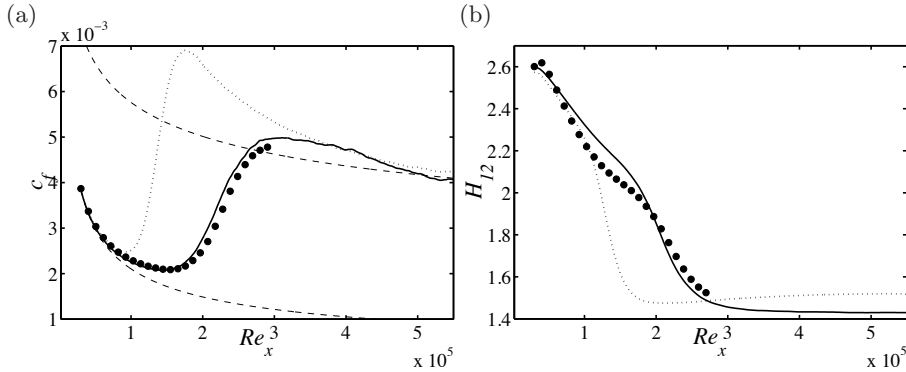


FIGURE 3. Integral quantities during bypass transition ($Tu = 4.7\%$) for different SGS models. (a): skin-friction coefficient c_f , (b): shape factor H_{12} . ADM-RT, —; no-model LES, ·····; DNS, • (Brandt *et al.* 2004). The thin dashed lines correspond to analytical correlations for both laminar and turbulent boundary-layer flow.

4.1. LES validation

In a first step, the possibility to reduce the numerical resolution and consequently replacing the effect of the non-resolved scales by a subgrid-scale model (see section 3.2) is explored. In particular, additional to fully-resolved DNS, two different modelling approaches are considered: under-resolved DNS without model where the interaction between the resolved and unresolved scales is essentially neglected and the ADM-RT model. This SGS model has been shown to perform particularly well with transitional wall-bounded flows (Schlatter *et al.* 2006b). All the LES presented in this section are performed with a free-stream turbulence intensity of $Tu = 4.7\%$ on the “Large LES” grid given in table 1. The reference DNS data is taken from Brandt *et al.* (2004) using the same numerical method and inflow turbulence generation algorithm.

Figure 3 shows the evolution of the statistically averaged skin friction coefficient c_f and the shape factor H_{12} as a function of the downstream distance Re_x . The skin friction coefficient gives a measure on how well the near-wall flow structures can be represented, whereas the shape factor, being the ratio between the boundary-layer displacement thickness and the momentum thickness, describes the flow development and structural reordering of the boundary layer during laminar-turbulent transition further away from the wall.

The evolution of the skin friction (figure 3a) clearly shows that the no-model approach without employing a subgrid-scale model leads to inaccurate results. This behaviour of under-resolved simulations is however well-known from other studies: The reduced dissipation present in the flow leads to an increased fluctuation level at the scales close to the numerical cutoff; in case of flows undergoing transition this increased energy may be causing premature

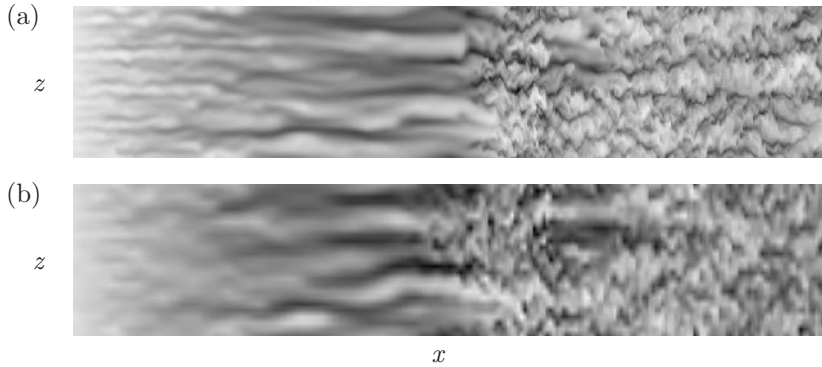


FIGURE 4. Instantaneous streamwise velocity in a plane parallel to the wall. (a): DNS. (b): LES using ADM-RT. Light colour indicates low velocity, dark colour high velocity. Streamwise extent $Re_x = [32000, 300000]$, spanwise extent enlarged by a factor of 5.

breakdown. Usually, increased values of the wall-normal velocity gradient close to the wall lead to a dominant overshoot of the skin friction, until the flow has settled down to a new equilibrium state accounting for the missing dissipation in the small scales. The ADM-RT model with a constant model coefficient however is seen to provide an accurate prediction of the skin friction throughout the laminar initial phase dominated by the streaky structures ($Re_x < 150000$), the stage dominated by the intermittent appearance and growth of turbulent spots ($Re_x < 300000$), and the fully-developed turbulent region thereafter.

The shape factor given in figure 3b confirms the previous findings: The initial phase ($Re_x < 100000$) characterised by only minor disturbances within the boundary layer is predicted accurately also by the no-model LES. However, as soon the boundary-layer distortion becomes too large, the under-resolved DNS will immediately break down to turbulence. It is interesting to note that the SGS model feature a slight departure from the reference level of H_{12} between $Re_x = 100000$ and $Re_x = 170000$; however the final stages of transition seem not to be influenced.

A comparison of an instantaneous visualisation of a wall-parallel plane at $y = 2\delta_0^*$ from both DNS and ADM-RT is presented in figure 4. Note that for both simulations the same amplitudes and phase shifts in the inlet free-stream turbulence have been used (see section 3.3.1), consequently the flow structures can be directly compared between DNS and LES. The most obvious feature is that the LES data looks slightly blurred, which is a natural consequence of the lower resolution. Nevertheless, many of the flow structures present in the DNS flow field can also be detected in the LES field, and vice versa: the shape and location of the dominant strong streaks, the intermittent breakdown to localised turbulent spots, and a calm region even more downstream than the

TABLE 2. Control penalties, estimation sensor noise, measurement-strip position, actuation-strip position and location of the base flow target profiles for the estimator and the controller.

Estimation			Control		
Sensor noise	p	50	penalties	l	10^2
	τ_x	0.07		r^2	0
	τ_z	0.07			
$Re_{x_{start}}$		6.04×10^4	$Re_{x_{start}}$		1.95×10^5
$Re_{x_{end}}$		1.50×10^5	$Re_{x_{end}}$		2.85×10^5
location of target profile		1.05×10^5	location of target profile		2.40×10^5

first turbulent patch. This figure clearly shows that – despite the lower resolution used in the LES – a good prediction of the dominating flow physics and the processes leading to turbulent breakdown can be obtained via appropriate subgrid-scale modelling. It can also be shown that the LES is able to capture the instantaneous structures just prior to turbulent breakdown.

4.2. Full information control

Results on linear feedback control of a boundary layer subject to free-stream turbulence are reported next. The design parameters for the compensator problem are reported in table 2 and will be discussed when presenting the results for each specific case.

The first step when applying control is to design a reasonably good full-information controller. This can be used as reference for the compensation, since the best possible performance is expected when the whole flow field is known. This case is also used as a benchmark for LES: Since LES is used for most of the simulations, it is considered important to evaluate the SGS model against DNS data not only in the general case without control, but also in the case of full information control. Further, in order to later compare these results to those from the compensator, the blowing and suction strip are placed further downstream, so that there will be enough space for the measurement region at the beginning of the computational domain, see table 2. Note that in the following figures the gray areas correspond to the regions where measurements are taken, and blowing and suction is applied, respectively. The simulations in the remaining part of this section are performed with a turbulence level $Tu = 3.0\%$ except the results in figure 6 where $Tu = 4.7\%$.

In figure 5 the wall-normal maximum of the streamwise velocity perturbation is shown for both DNS and LES of the uncontrolled case as well as for the two cases with full information control. This quantity is selected since

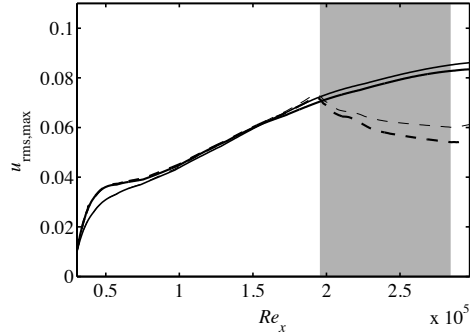


FIGURE 5. Wall-normal maximum u_{rms} . no control DNS, —; no control LES, —; control DNS, ----; control LES, -.-.-.

it indicates the growth of the streaks inside the boundary layer. It can be clearly seen that the control is able to inhibit the streak growth and that using LES-(ADM-RT) gives similar decrease of the streak amplitude as in the fully-resolved DNS. Slight differences between LES and DNS can be noticed at the inlet of the domain. This can be explained by noting that the wall-normal maximum of the rms value is a very sensitive quantity, involving both the location and the amplitude of the fluctuations. Indeed mean quantities, like the skin friction, would not show any difference at all in such a plot.

A study to investigate the influence of the length of the control region on the transition delay was also performed. The free-stream turbulence level was chosen to be 4.7% to be able to reproduce the full transition process within the small computational domain (Barri 2006). The initial and final locations of the control region are reported in table 3, whereas the value of the wall-normal maximum of the streamwise velocity fluctuations and the skin friction are displayed in figure 6 for the three cases under consideration together with the reference uncontrolled case. It can be noticed in figure 6a that with a longer control domain, it is possible to reduce the streak growth even more. The effect of the control is more pronounced when looking at the friction coefficient c_f as shown in figure 6b. By comparing the two plots it can be deduced that the large values of streamwise velocity fluctuations at the end of the computational domain are not associated to a fully turbulent flow. The results further show that for the longest control region the streak growth is indeed quenched for a larger distance but the downstream recovery is faster and the differences between the cases “Medium” and “Long” are attenuated further downstream.

In order to understand the physical mechanism behind the control, instantaneous features that appear in the controlled field are examined. In figure 7 the streamwise velocity component on a plane parallel to the wall at $y = 2\delta_0^*$ (figure 7a) along with the wall-normal velocity component at the wall (figure 7b) indicating the control actuation via wall blowing and suction is displayed.

TABLE 3. Study on the influence of the control region length. The initial and final location of the control region are given in units of Re_x .

	Start (Re_x)	End (Re_x)
No control	—	—
Short	5.3×10^4	1.4×10^5
Medium	5.3×10^4	1.9×10^5
Long	5.3×10^4	2.3×10^5

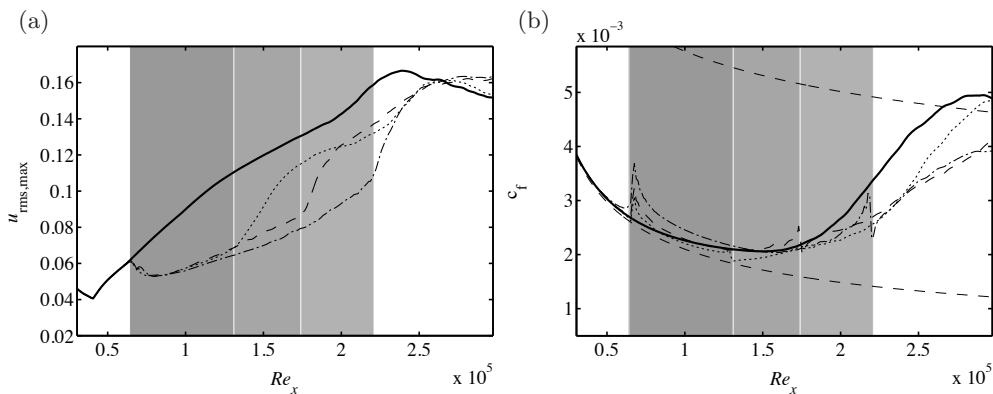


FIGURE 6. Wall-normal maximum $u_{\text{rms,max}}$ (a) and skin friction coefficient c_f (b). no control, —; short, ·····; medium, - - - -; long, - · - ·.

From these two instantaneous images of the flow one can see the correlation between the flow state and the control signal. In the case of a high-speed streak blowing is induced from the controller. This causes the flow downstream of the actuation to settle in a more stable state since the fast moving fluid is forced to move upwards away from the wall. The opposite action is happening for low-speed streaks i.e. the controller is applying suction to move high-speed fluid from the free stream to cancel the region of decelerated flow. One other aspect to note from this figure is that most of the control effort is concentrated at the beginning of the control region in agreement with the results by Chevalier *et al.* (2007a).

4.2.1. Limiting of control signal

When extending the linear control to these highly nonlinear scenarios, problems may arise and *ad hoc* tuning may be necessary. For our case, Brandt &

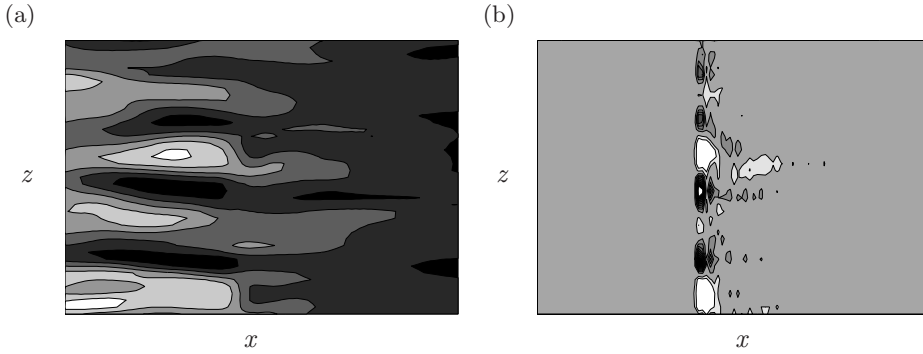


FIGURE 7. (a): Instantaneous streamwise velocity at $y = 2\delta_0^*$. (b): corresponding control signal. The levels of the contours are $u = [0.3U_\infty, 0.6U_\infty]$ for (a) and $v = [-2 \times 10^{-2}U_\infty, 5 \times 10^{-3}U_\infty]$ for (b). White corresponds to the minimum value and black to the maximum.

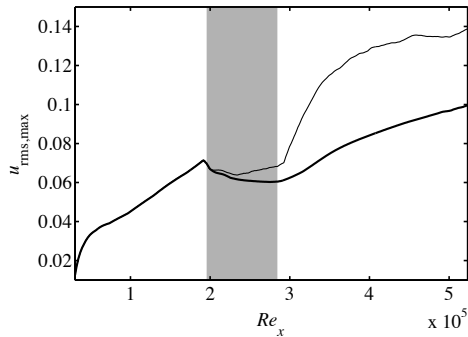


FIGURE 8. Wall normal maximum $u_{\text{rms,max}}$. Control with clipping of the blowing, —; Control without the clipping blowing, - - -.

Henningson (2004) observed that, if too strong localised blowing is applied, turbulent spots may be induced by local instabilities due to wall-normal inflectional profiles already inside the control region. An improvement of the transition delay can therefore be expected by limiting the blowing at the wall. This was implemented in the numerical code by imposing an artificial clipping to the control signal

$$v(x, y, z, t)|_{y=0} = \min\{v(x, y, z, t)|_{y=0}, v_{\text{max}}\}. \quad (30)$$

The clipping threshold v_{max} is set to $0.01U_\infty$, for cases where the (unlimited) maximum of the blowing at the wall occasionally reaches values of the order of $0.02U_\infty$. The value of v_{max} is chosen by examining the instantaneous values of

the blowing in cases where transition was triggered by the wall actuation. The comparison between the optimal linear control and control with limited blowing is displayed in figure 8, where the evolution of the wall-normal maximum of the streamwise velocity fluctuations is depicted for cases with and without clipping. The performance of the control is on average improved by limiting the blowing; analysis of the instantaneous velocity fields reveals that this is due to the absence of the localised spots intermittently induced by the strong control signals and not by an overall decrease of the streak amplitudes, or increase of the actuation efficiency. The results presented in the following are all obtained by limiting the blowing at the wall.

4.3. State estimation

The construction of the estimator involved extensive tuning of several parameters associated with the theoretical tools described in section 2.2. In particular, these parameters are: the covariance matrix as a model for the stochastic disturbances involved in the estimation process, the sensor noise quantifying the confidence in the measurements taken and the length of the estimation region.

The covariance matrix is essential for the estimator (see equation 19). In the ideal case, the measurements indicated in equation 20 would uniquely identify the current state of the system (Bewley & Protas 2004). This is not the case since there are unknown initial conditions, unknown external disturbances and noise corrupting the measurements. To improve the estimation in the case of free-stream turbulence, the variance of the external disturbances needed to be extended further out in the free stream if compared to that used in Chevalier *et al.* (2007a). A diagonal matrix was used as covariance matrix for the external disturbances. For the covariance of the wall measurements a simple function proportional to the boundary-layer velocity profile was selected.

The parameters that define the strength of the forcing that is applied to the system are the sensor noise. The tuning of these parameters was also performed by testing different sets of values; the set of values yielding the best performance is reported in table 2. Note that a relatively large value of the pressure sensor is needed to achieve good estimation. This limits the use of this measurement and can be explained by the fact that the pressure at the wall appears to be more sensitive to the free-stream turbulence than to the streaks inside the boundary layer.

One would expect that the longer the measurement strip the better the estimation since more information from the flow is available. However, since the gains are computed for a parallel flow, this may not be the case and above a certain length the quality of the estimation degrades. The optimal length was found to be 500 approximately δ_0^* units. Further, it was found that at these high levels of perturbation, estimation works better if the forcing is active only on the scales that correspond to the streaks. Thus the gains were rescaled in wavenumber space with a two-dimensional Gaussian function. The parameters of this function were determined by applying two-dimensional Fourier

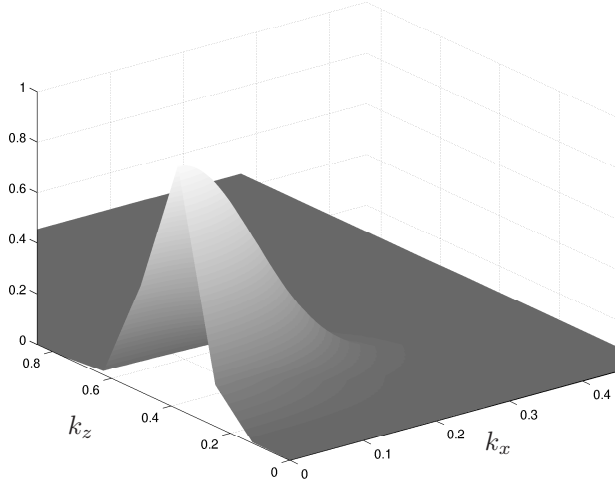


FIGURE 9. The Gaussian function scaling the estimation gains in wavenumber space. The centre of the Gaussian is at $k_x = 0$ and $k_z = 0.4$ in units of δ_0^{*-1} .

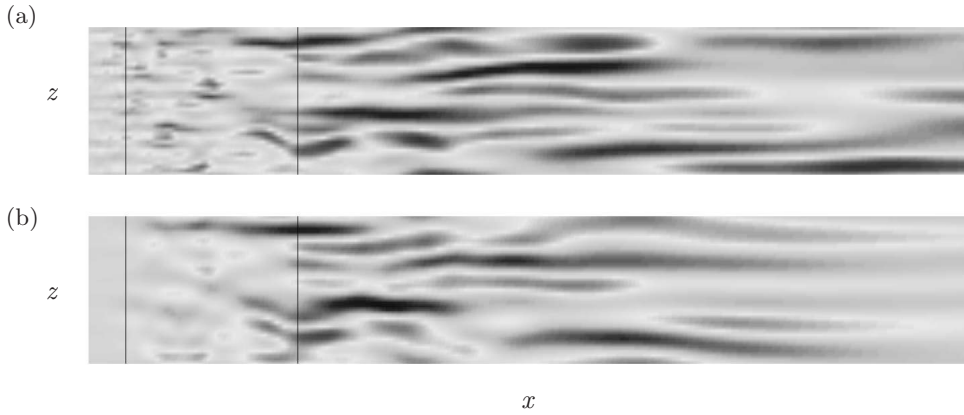


FIGURE 10. Instantaneous streamwise velocity fields. (a): real flow; (b): estimated flow. The measurement strip is indicated with two vertical lines. Streamwise extent $Re_x = [32000, 570000]$, spanwise extent enlarged by a factor of 5.

transforms along the wall-parallel directions to the flow fields to be estimated and extracting the wavenumbers of richest energy content. One example of this weighting function is shown in figure 9. The gains are focused around wavenumber $k_x = 0.0$ in the streamwise direction, which corresponds to infinitely long structures and around $k_z = 0.4$ which corresponds to the spanwise width of the most energetic structures, namely the streaks.

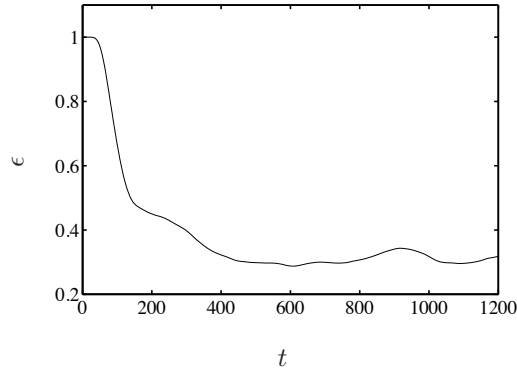


FIGURE 11. Estimation error according to equation 31.

Two different criteria were used to determine the performance of the estimator. The first was visual inspection of the instantaneous velocity fields: One example of this comparison can be seen in figure 10, where the streamwise velocity in a plane parallel to the wall is displayed for the real and the estimated flow. It can be seen in the figure that the main features of the incoming streaks are well reproduced in the estimated field. A second, more systematic way, is to calculate the estimation error given by

$$\epsilon = \frac{\int_{\Omega} (q - \hat{q}) d\Omega}{\int_{\Omega} (q) d\Omega}, \quad (31)$$

where Ω is the region selected to evaluate the estimation error. In figure 11 the estimation error is plotted as a function of time. In this case the error is computed in a plane parallel to the wall, $y/\delta_0^* = 2$, over the whole region where the control will be applied. This is selected as the most relevant area in terms of compensator performance since the flow in this region is used to compute the control signal. It can be seen in the figure that the estimation is converging toward values of $\epsilon \approx 0.3$ after an initial transient of about 400 time units.

The wall-normal maximum of the streamwise velocity perturbation is shown for both the real and the estimated flow in figure 12. The perturbations are weaker in the estimated flow, a strong estimation forcing leading directly to transition in the estimator simulation. In the real flow, the streaks are forming and growing also downstream of the estimation region, whereas in the estimated flow the streaks decay downstream of the measurement region. This can be explained by the fact that the free-stream turbulence is continuously forcing the streaks all along the plate whereas the estimation forcing is active only in a limited streamwise region, i.e. the gray area in the plot.

In figure 13 the wall-normal profiles of u_{rms} at different streamwise locations are shown. Again it can be seen that the streaks are weaker in the estimated flow than in the real flow, and that the difference between the two fields increases further downstream. Perturbations in the free stream are not

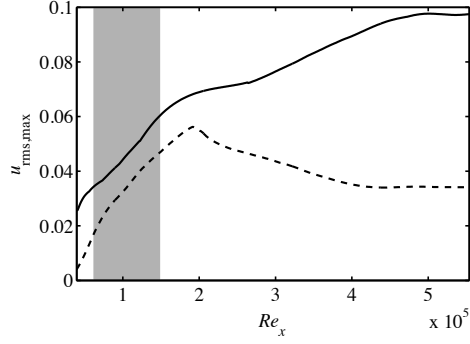


FIGURE 12. Wall-normal maximum of u_{rms} . Real flow, —; Estimated flow, - - - . The shaded area indicates the measurement region.

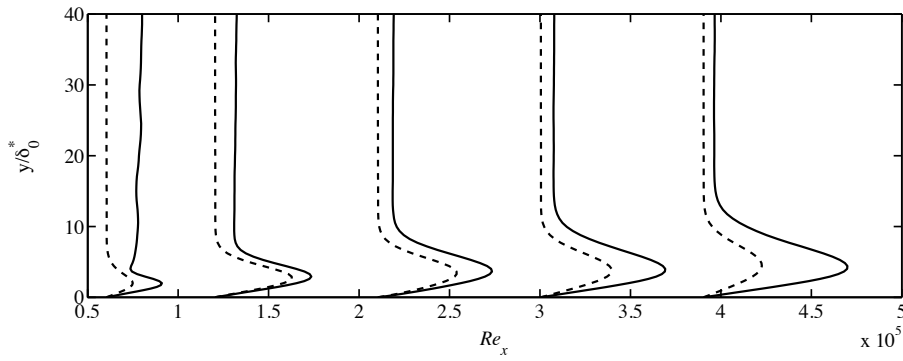


FIGURE 13. Wall normal profile of u_{rms} at different streamwise positions $Re_x = [0.6, 1.2, 2.1, 3.0, 3.9] \times 10^5$. The values of u_{rms} are scaled with 9.0×10^5 . Real flow, —; Estimated flow, - - - .

reproduced in the estimator and the estimation is more accurate close to the wall.

4.4. Compensator

The final stage is combining the full information controller and the estimator into the compensator. The procedure requires the estimator to run first without the control until the estimated field approaches the real flow; afterwards the control forcing is turned on. The control region is placed downstream of the estimated field and an overlap between the two strips is avoided. At the location where the actuation is active, the amplitude of the streaks is significantly increased. The perturbations to be controlled are further downstream i.e. in the region where non-linear effects are more important.

A visualisation of the controlled and uncontrolled flow field is displayed in figure 14 in a wall-parallel plane. The decrease of the streak amplitude in the control region is clearly visible. A turbulent spot is appearing further downstream in the uncontrolled flow while the flow is laminar when blowing/suction is applied. It can also be noticed that the control often changes an incoming high-speed streak into a low-speed region and vice versa. Further, a rapid increase in the streak amplitude is occurring after the end of the control region.

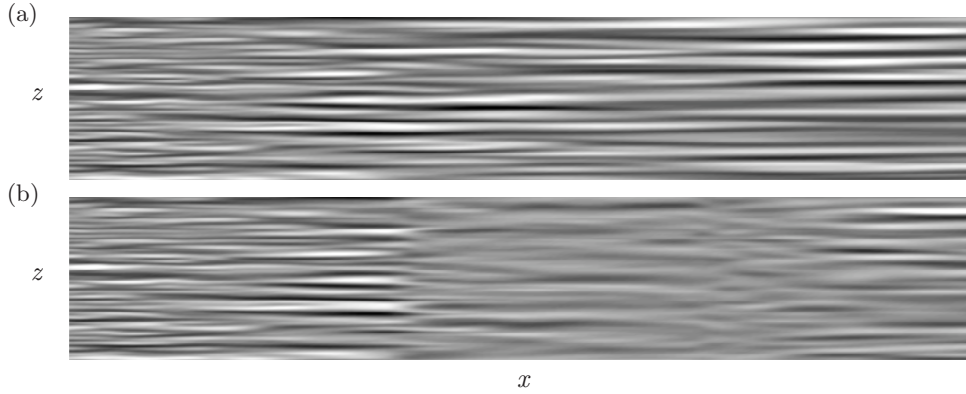


FIGURE 14. Instantaneous streamwise velocity fields. (a): uncontrolled; (b): controlled. Streamwise extent $Re_x = [32000, 382000]$, wall-normal distance $2\delta_0^*$, true aspect ratio.

In figure 15a the wall-normal maximum of the *rms*-value of the streamwise velocity perturbation is shown for the uncontrolled case and for both full information control and compensation. As observed by the flow visualisation in figure 15a, the growth of the streaks is reduced within the control region. However, downstream of the control region, velocity fluctuations continue to grow. This can be explained by the presence of the free-stream turbulence above the boundary layer that is able to induce new perturbations inside the boundary layer.

The skin friction coefficient is shown in figure 15b. This plot quantifies the transition delay which can be achieved in the case of boundary-layer transition induced by free-stream turbulence. The transition delay obtained without estimation corresponds approximately to the length of the control region. The delay is between $120000\nu/U_\infty$ and corresponds to approximately 15 – 20% of the full length of a typical turbine blade, resulting in a reduction of the total friction drag of 5 – 10%. The loss of performance to be expected in the case of control based on estimation from wall measurements is not severe. Thus, a longer control region or alternatively a sequence of measurement and blowing/suction strips may lead to further delay or even prevent the transition process.

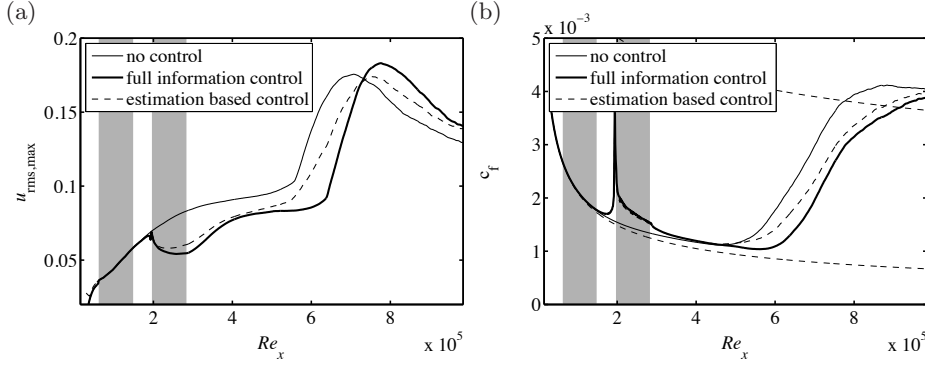


FIGURE 15. (a): Wall normal maximum u_{rms} ; (b): skin friction coefficient c_f . No control, —; Full information control, —; Compensator, - - - -.

In figure 16, wall-normal profiles of the *rms* value of the streamwise velocity perturbation are shown at different streamwise stations along the plate for the three cases under consideration. The reduction of streak amplitude is evident in the control region. Note also that where blowing/suction is applied the profiles feature a double-peak structure: the lowest peak closest to the wall is due to the local effect of the actuation, while the largest peak, representing the streak, is moved away from the wall. The changeover from laminar to turbulent streaks is occurring in the region $5 \times 10^5 < Re_x < 7 \times 10^5$. The typical profiles for u_{rms} of a turbulent boundary layer are observed at the end of the computational domain.

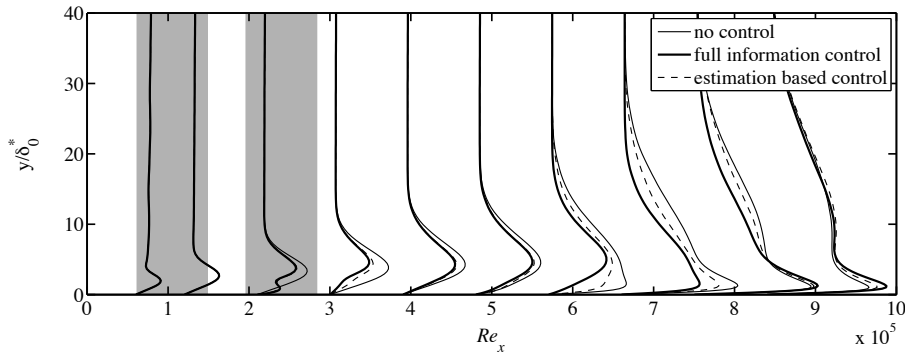


FIGURE 16. Wall normal profiles of u_{rms} at different streamwise positions $Re_x = [0.6, 1.2, 2.1, 3.0, 3.9, 4.8, 5.7, 6.6, 7.5, 8.4] \times 10^5$. The values of u_{rms} are scaled with 8.5×10^5 . No control, —; Full information control, —; Compensator, - - - -.

The production of turbulent kinetic energy $\overline{wv}\partial U/\partial y$ with the Reynolds shear stress \overline{wv} , is considered to characterise the effect of the blowing/suction at the wall. The wall-normal profiles of the turbulent production at two streamwise positions are displayed in figure 17. It can be seen that the turbulence production increases near the wall due to the blowing and suction while it decreases farther up in the boundary layer, attaining negative values at the beginning of the control region. In the compensator a reduction over the whole profile is observed as well as a small peak near the wall.

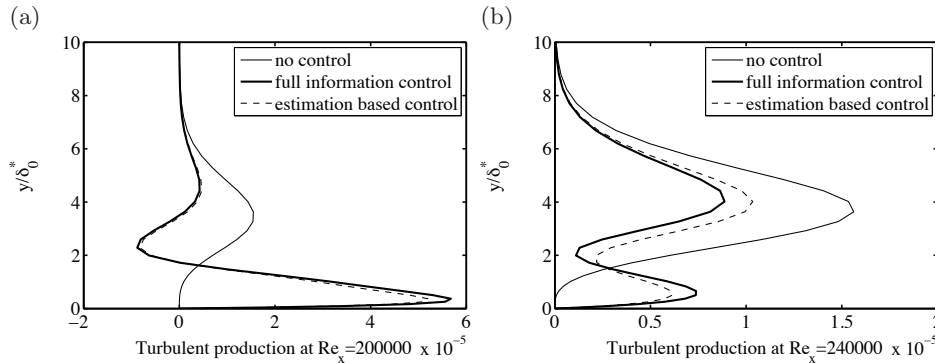


FIGURE 17. Wall normal profiles of turbulent production at (a) $Re_x = 2.0 \times 10^5$ and (b) $Re_x = 2.4 \times 10^5$. No control, —; Full information control, —; Compensator, - - -.

In order to study the performance of the control for higher streak amplitudes, simulations with turbulence intensity $Tu = 4.0\%$ are also performed. Owing to the larger turbulence intensity the growth of the streaks is faster, the transition location is moved upstream and the amplitude of the streaks within the control region are further increased. Overall, the performance of the estimation is as in the case presented above, while the extension of the transition delay is reduced. Even though the growth of the streaks is reduced in the control region, the regeneration downstream is more rapid at this higher free-stream turbulence levels. As shown by Barri (2006), for the control to be more effective, maybe the actuation region should be placed further upstream.

From this project it was desighed that transition delay can

5. Conclusions

Numerical simulations of the transition to turbulence occurring in a flat-plate boundary-layer flow subjected to high levels of free-stream turbulence are performed. This scenario, denoted bypass transition, is characterised by the non-modal growth of streamwise elongated disturbances, so-called streaks. When these streaks reach large enough amplitudes, breakdown into turbulent spots occurs via their secondary instability. The scenario under consideration is highly intermittent in nature, i.e. streaks appear randomly in the boundary

layer, and therefore large computational domains and long integration times are needed to obtain converged statistical data.

In order to reduce the computational cost, mostly large-eddy simulations are performed. The ADM-RT subgrid-scale model is shown to be particularly suited for transitional flows: It is thoroughly validated before examining the effect on the transition process. The results indicate that the details of the streak breakdown can and need to be captured by LES. The high-frequency oscillations of the elongated streaks appearing as spot precursors define the grid size on which the LES can be performed. The reduction in terms of number of degrees of freedom compared to a full DNS is of the order of 10, while the computational cost is reduced about 50 times.

Linear model-based feedback control is applied in order to delay transition, where the linear parallel Orr-Sommerfeld/Squire system is used to design the estimation and control laws. The method presented here was previously developed by Hoepffner *et al.* (2005); Chevalier *et al.* (2006, 2007a) and shown to be successful in damping linear and weakly nonlinear perturbation in a variety of wall-bounded shear flows. The method is now applied to flows with highly nonlinear behaviour.

In practical situations, the full flow field is usually not accessible. The control problem is therefore combined with an estimation procedure based on wall measurements, the two wall-parallel components of the wall-shear stress and the pressure at the wall being considered here. It is found that to achieve an accurate estimation most of the confidence should be put in the shear-stress data; the pressure measurements are in fact too affected by the high-level fluctuations in the free stream.

The results presented show that the control is able to reduce the energy of the streaks, which are responsible, through their secondary instabilities, for the considered bypass-transition scenario and thus delay the whole process. The delay achieved is of order of the streamwise extent of the area where control is applied. For turbomachinery applications, this amounts to about 15 – 20% of the length of a typical turbine blade, resulting in a reduction of the total friction drag of 5 – 10%. The control performance is limited by the fast growth of the streaks just downstream of the region where blowing and suction is applied. This recovery is similar to that observed when control of turbulent flow is investigated and it can be explained by considering the action of the control in these highly disturbed flow: When blowing/suction is applied, the streamwise streaks are quenched close to the wall while the upper part of the boundary layer is less affected. As a consequence, as soon as the actuation is turned off, the streaks diffuse into the shear layer near the wall and can again be amplified. The relatively fast recovery of the streamwise streaks downstream of the control region was also observed in the recent experimental work by Lundell (2007). This author considers the same transition scenario but a different control strategy: reactive control is applied with sensors and actuators placed in a staggered manner. A more direct comparison between

the linear optimal control and the experiments appears therefore relevant and it is the object of new investigations.

The streamwise streaks can be estimated from wall measurements alone; however the structures occurring in the real flow are reproduced correctly mainly in the region where the measurements are taken. Downstream of this region the estimated field gradually diverges from the real field, revealing the importance of the continuous excitation of the boundary layer by the external free-stream turbulence (Westin *et al.* 1998). Control based on estimation (termed compensator) is therefore less effective than full information control. For actual implementations of feedback control the estimation process needs to be improved, in particular by reducing its cost. With this aim, two directions may be followed. First, model reduction can be introduced in the estimation problem. Global modes of the flow can be used for this, as global eigenmodes (Åkervik *et al.* 2007) or balanced POD modes (Rowley 2005). The model based on these two- or three-dimensional modes does not need to be linear, possibly improving the estimation performance for this type of flows. Alternatively, the relation between sensors and actuators may be deduced directly from flow measurements, relaxing the need for a flow model, as suggested e.g. by Lundell (2007). The latter option will be the object of future work, in the context of a closer interplay between experiments and simulations.

Acknowledgements

The authors wish to thank Mattias Chevalier, Espen Åkervik and Jérôme Hoepffner for many fruitful discussions. Computer time was provided by the Centre for Parallel Computing (PDC) at KTH, Stockholm. The present work is supported by the EOARD grant FA8655-04-1-3032 which is gratefully acknowledged.

References

- ÅKERVIK, E., HOEPFFNER, J., EHRENSTEIN, U. & HENNINGSON, D. S. 2007 Optimal growth, model reduction and control in a separated boundary-layer flow using global modes. *J. Fluid Mech.* **579**, 305–314.
- ANDERSSON, P., BERGGREN, M. & HENNINGSON, D. S. 1999 Optimal disturbances and bypass transition in boundary layers. *Phys. Fluids* **11**, 134–150.
- BAGHERI, S., HOEPFFNER, J., SCHMID, P. J. & HENNINGSON, D. S. 2007 Input-output analysis and control design applied to a linear model of spatially developing flows. *Appl. Mech. Rev.* Accepted.
- BARRI, M. 2006 Optimal control of bypass transition in boundary layers. Master's thesis, KTH Mechanics, Stockholm, Sweden.
- BERGGREN, M. 1998 Numerical solution of a flow-control problem: vorticity reduction by dynamic boundary action. *SIAM J. Sci. Comp.* **19** (3), 829–860.
- BEWLEY, T., TEMAM, R. & ZIANE, M. 2000 A general framework for robust control in fluid mechanics. *Physica D*. **138**, 360–392.
- BEWLEY, T. R. 2001 Flow control: New challenges for a new renaissance. *Prog. Aerosp. Sci.* **37**, 21–58.
- BEWLEY, T. R., MOIN, P. & TEMAM, R. 2001 DNS-based predictive control of turbulence: an optimal benchmark for feedback algorithms. *J. Fluid Mech.* **447**, 179–225.
- BEWLEY, T. R. & PROTAS, B. 2004 Skin friction and pressure: the 'footprints' of turbulence. *Physica D* **196**, 28–44.
- BRANDT, L. 2007 Numerical studies of the instability and breakdown of a boundary-layer low-speed streak. *Eur. J. Mech./B Fluids* **26** (1), 64–82.
- BRANDT, L. & HENNINGSON, D. S. 2002 Transition of streamwise streaks in zero-pressure-gradient boundary layers. *J. Fluid Mech.* **472**, 229–262.
- BRANDT, L. & HENNINGSON, D. S. 2004 Linear feedback control of perturbations developing in a boundary layer under free-stream turbulence. In *Advances in Turbulence X, Proc. of the Tenth European Turbulence Conference* (ed. H. I. Andersson & P. Å. Krogstad), pp. 767–770. CIMNE.
- BRANDT, L., SCHLATTER, P. & HENNINGSON, D. S. 2004 Transition in boundary layers subject to free-stream turbulence. *J. Fluid Mech.* **517**, 167–198.
- CHEVALIER, M., HOEPFFNER, J., ÅKERVIK, E. & HENNINGSON, D. S. 2007a Linear feedback control and estimation applied to instabilities in spatially developing boundary layers. *J. Fluid Mech.* **588**, 163–187, 167–187.
- CHEVALIER, M., HOEPFFNER, J., BEWLEY, T. R. & HENNINGSON, D. S. 2006 State estimation in wall-bounded flow systems. Part 2. Turbulent flows. *J. Fluid Mech.* **552**, 167–187.
- CHEVALIER, M., SCHLATTER, P., LUNDBLADH, A. & HENNINGSON, D. S. 2007b Simson: A pseudo-spectral solver for incompressible boundary layer flows. Technical Report KTH/MEK/TR-07/07-SE. KTH, Department of Mechanics, Stockholm.
- COLLIS, S., CHANG, Y., KELLOGG, S. & PRABHU, R. D. 2000 Large eddy simulation and turbulence control. *AIAA paper* (2000-2564).
- FARRELL, B. F. & IOANNOU, P. J. 1996 Turbulence suspension by active control. *Phys. Fluids* **8** (5), 1257–1268.

- FRIEDLAND, B. 1986 *Control system design: An introduction to state-space methods*. Mineola, New York: Dover.
- GROSCH, C. E. & SALWEN, H. 1978 The continuous spectrum of the Orr-Sommerfeld equation. Part 1. The spectrum and the eigenfunctions. *J. Fluid Mech.* **87**, 33–54.
- HENNINGSON, D. S. 1996 Comment on: "Transition in shear flows. Nonlinear normality versus non-normal linearity"[Phys. Fluids 7, 3060 (1995)]. *Phys. Fluid* **8** (8), 2257–2258.
- HOEPFFNER, J., CHEVALIER, M., BEWLEY, T. R. & HENNINGSON, D. S. 2005 State estimation in wall-bounded flow systems. Part 1. Perturbed laminar flows. *J. Fluid Mech.* **534**, 263–294.
- HÖGBERG, M., BEWLEY, M. & HENNINGSON, D. S. 2003a Relaminarization of $Re_\tau = 100$ turbulence using gain scheduling and linear state-feedback control. *Phys. Fluids* **15**, 3572–3575.
- HÖGBERG, M., BEWLEY, M. & HENNINGSON, D. S. 2003c Linear feedback control and estimation of transition in plane channel flow. *J. Fluid Mech.* **481**, 149–175.
- HÖGBERG, M., CHEVALIER, M. & HENNINGSON, D. S. 2003b Linear compensator control of a pointsource induced perturbation in a Falkner-Skan-Cooke boundary layer. *Phys. Fluids* **15**, 2449–2452.
- HÖGBERG, M. & HENNINGSON, D. S. 2002 Linear optimal control applied to instabilities in spatially developing boundary layers. *J. Fluid Mech.* **470**, 151–179.
- JACOBS, R. G. & DURBIN, P. A. 2001 Simulations of bypass transition. *J. Fluid Mech.* **428**, 185–212.
- JOSHI, S. S., SPEYER, J. L. & KIM, J. 1995 Modeling and control of two dimensional poissuille flow. In *34th IEEE Conf on Decision and Control*, pp. 921–927.
- JOSLIN, R. D. 1998 Aircraft laminar flow control. *Annu. Rev. Fluid Mech.* **30**, 1–29.
- JOSLIN, R. D., ERLEBACHER, G. & HUSSAINI, M. Y. 1996 Active control of instabilities in laminar boundary layers-overview and concept validation. *J. Fluids Eng.* **118** (3), 494–497.
- JOSLIN, RONALD D., GUNZBURGER, MAX D. & NICOLAIDES, R. A. 1997 A self-contained automated methodology for optimal flow. *AIAA J.* **35** (5), 816–824.
- KAILATH, T. & HASSIBI, A. H. SAYED B. 2000 *Linear Estimation*. New Jersey: Prentice Hall.
- KARAMANOS, G.-S. & KARNIADAKIS, G. E. 2000 A spectral vanishing viscosity method for large-eddy simulations. *J. Comput. Phys.* **163**, 22–50.
- KIM, J. & BEWLEY, T. R. 2007 A linear systems approach to flow control. *Annu. Rev. Fluid Mech.* **38** (1), 383–417.
- KIM, J. & LIM, J. 2000 A linear process in wall-bounded turbulent shear flows. *Phys. Fluids* **12** (8), 1885–1888.
- LANDAHL, M. T. 1980 A note on an algebraic instability of inviscid parallel shear flows. *J. Fluid Mech.* **98**, 243–251.
- LAURIEN, E. & KLEISER, L. 1989 Numerical simulation of boundary-layer transition and transition control. *J. Fluid Mech.* **199**, 403–440.
- LEWIS, F. L. & SYRMOS, V. L. 1995 *Optimal Control*. New York: Wiley-Interscience.
- LUNDBLADH, A., BERLIN, S., SKOTE, M., HILDINGS, C., CHOI, J., KIM, J. & HENNINGSON, D. S. 1999 An efficient spectral method for simulation of incompressible flow over a flat plate. Technical Report KTH/MEK/TR-99/11-SE. KTH, Department of Mechanics, Stockholm.

- LUNDELL, F. 2007 Reactive control of transition induced by free-stream turbulence: an experimental demonstration. *J. Fluid Mech.* **585**, 41–71.
- MANS, J., DE LANGE, H. C. & VAN STEENHOVEN, A. A. 2007 Sinuous breakdown in a flat plate boundary layer exposed to free-stream turbulence. *Phys. Fluids* **19** (088101).
- MATSUBARA, M. & ALFREDSSON, P. H. 2001 Disturbance growth in boundary layers subjected to free stream turbulence. *J. Fluid. Mech.* **430**, 149–168.
- METCALFE, R. W. 1994 Boundary layer control: A brief review. In *Computational Fluid Dynamics '94, Invited lectures of the Second European CFD Conference; Stuttgart, Germany* (ed. S. Wagner, J. Periaux & E. Hirschel), *Progress in Astronautics and Aeronautics*, pp. 52–60. John Wiley & Sons.
- MOIN, P. & BEWLEY, T. 1994 Feedback control of turbulence. *Appl. Mech.* **47** (6), part 2, S3–S13.
- MOIN, P. & MAHESH, K. 1998 Numerical simulation: A tool in turbulence research. *Annu. Rev. Fluid Mech.* **30**, 539–578.
- NORDSTRÖM, J., NORDIN, N. & HENNINGSON, D. S. 1999 The fringe region technique and the Fourier method used in the direct numerical simulation of spatially evolving viscous flows. *SIAM J. Sci. Comp.* **20**, 1365–1393.
- REDDY, S. C. & HENNINGSON, D. S. 1993 Energy growth in viscous channel flows. *J. Fluid Mech.* **252**, 209–238.
- ROBINSON, S. K. 1991 The kinematics of turbulent boundary layer structure. *Tech. Rep.* TM 103859. NASA.
- ROWLEY, C. W. 2005 Model reduction for fluids using balanced proper orthogonal decomposition. *Intl J. Bifurcation Chaos* **15** (3), 997–1013.
- SCHLATTER, P., STOLZ, S. & KLEISER, L. 2004 LES of transitional flows using the approximate deconvolution model. *Int. J. Heat Fluid Flow* **25** (3), 549–558.
- SCHLATTER, P., STOLZ, S. & KLEISER, L. 2006a Analysis of the SGS energy budget for deconvolution- and relaxation-based models in channel flow. In *Direct and Large-Eddy Simulation VI* (ed. E. Lamballais, R. Friedrich, B. J. Geurts & O. Métais), pp. 135–142. Springer, Dordrecht, The Netherlands.
- SCHLATTER, P., STOLZ, S. & KLEISER, L. 2006b LES of spatial transition in plane channel flow. *J. Turbulence* **7** (33), 1–24.
- SCHMID, P. J. & HENNINGSON, D. S. 2001 *Stability and Transition in Shear Flows*. New York: Springer.
- SEYED, M. M. 2007 Estimation and control of bypass transition in the Blasius boundary layer. Master's thesis, KTH Mechanics, Stockholm, Sweden.
- SKOGESTAD, S. & POSTLETHWAITE, I. 2005 *Multivariable feedback control, Analysis and Design, 2nd edition*. West Sussex: Wiley.
- STOLZ, S. & ADAMS, N. A. 1999 An approximate deconvolution procedure for large-eddy simulation. *Phys. Fluids* **11** (7), 1699–1701.
- STOLZ, S., ADAMS, N. A. & KLEISER, L. 2001 An approximate deconvolution model for large-eddy simulation with application to incompressible wall-bounded flows. *Phys. Fluids* **13** (4), 997–1015.
- THOMAS, A. S. W. 1983 The control of boundary-layer transition using a wave-superposition principle. *J. Fluid Mech.* **137**, 233–250.
- THOMAS, A. S. W. 1990 Active wave control of boundary-layer transition. In *Viscous Drag Reduction in Boundary Layers* (ed. D. M. Bushnell & J. N. Hefner),

Progress in Astronautics and Aeronautics, vol. 123. Washington D.C.: American Institute of Aeronautics and Astronautics.

WESTIN, K. J. A., BAKCHINOV, A. A., KOZLOV, V. V. & ALFREDSSON, P. H. 1998 Experiments on localized disturbances in a flat plate boundary layer. Part 1: the receptivity and evolution of a localized free stream disturbance. *Eur. J. Mech. B/Fluids* **17**, 823–846.

Paper 2

Feedback Control of Boundary Layer Bypass Transition: Experimental and Numerical Progress

By Fredrik Lundell, Antonios Monokrousos & Luca Brandt

Linné Flow Centre, Department of Mechanics
Royal Institute of Technology, SE-100 44 Stockholm, Sweden

47th AIAA Aerospace Sciences Meeting, Orlando, FL

Experimental and numerical work at the Linné FLOW Centre on active control of transition induced by free-stream turbulence is reviewed and two extensions to previous work are reported. Previously, an experimental setup with upstream sensors and downstream actuators has been built. It has been demonstrated that an *ad-hoc* control algorithm is able to give a considerable attenuation of the disturbance amplitude downstream of the actuators. Furthermore, large-eddy simulations (LES) of optimal feedback control have been performed for a similar flow configuration and disturbance attenuation as well as transition delay have been obtained. Two extensions are made. First, an effort is made to match the disturbance behaviour in the experimental flow case and in the LES. Control is applied in simulations of the matched system aiming at approaching the type of actuation used in the experiments (localised suction). The control law is still computed as optimal feedback of the linear system. As the actuation ability approaches the experiments (where much simpler controllers were used), so does the control effect. Second, system identification (SI) is applied to the experimental data and a more efficient controller is designed. It is made plausible that controllers designed by SI can give considerable improvements in the disturbance attenuation. Implications for future work in the area of active control are discussed.

1. Introduction

The term boundary layer bypass transition denotes transition scenarios where the dominant instability mechanism is not the exponential growth of two-dimensional Tollmien-Schlichting waves. The most common example is probably transition induced by high levels of free-stream turbulence (Matsubara & Alfredsson 2001) (typically above 0.5-1% of the free-stream velocity). The non-normality of the linearised operator relevant to the dynamics of perturbations of the boundary layer flows, evidenced by the associated non-orthogonal set of eigenmodes, can cause significant transient energy growth. The upstream

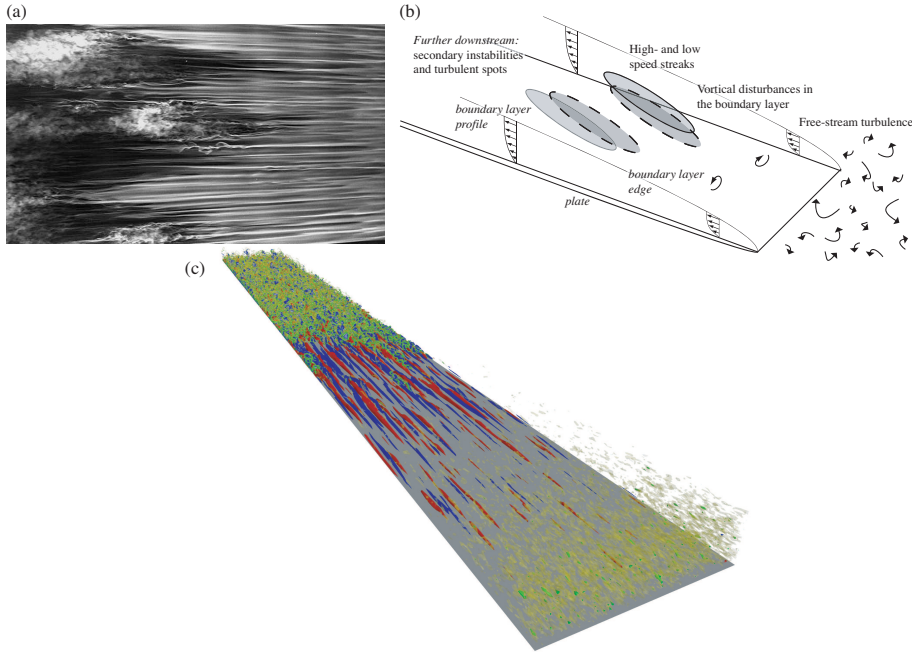


FIGURE 1. Visualisations (a,c) and schematic (b) of boundary layer transition induced by free-stream turbulence. Flow is from right to left. In the experimental visualisation in (a), the smoke is assembled in low velocity regions. In the numerical visualisation in (c), the flow is from lower right to upper left. The blue and red isosurfaces correspond to low and high velocity in a box close to the wall shows the flow and the green and yellow isosurfaces indicate the λ_2 vortex identification criterion. The flow is fully turbulent in the second half of the domain. (c) is a courtesy of Philipp Schlatter (private communication).

perturbations which undergo the largest possible growth consist of streamwise counter-rotating vortex pairs (Andersson *et al.* 1999). These vortices lift low-momentum fluid from the wall and push high-momentum fluid from the outer part of the shear layer towards the plate, thus creating elongated regions of alternating accelerated and decelerated fluid, called streaks. The process of lifting of low-momentum fluid from the region near the plate and pulling high-momentum fluid from the outer region is known as lift-up effect (Landahl 1980).

After their initial generation owing to the lift-up, the streaks grow in strength and become susceptible to high-frequency secondary instabilities.

These appear as symmetric and antisymmetric oscillations of the streaks, forming localized regions of chaotic swirly motion, called turbulent spots (Matsubara & Alfredsson 2001; Brandt *et al.* 2004; Mans *et al.* 2007). Subsequently the spots grow, eventually merge and a fully-developed turbulent boundary layer is formed. Visualisations and a schematic of the transition process under free-stream turbulence from experiments and numerical simulations are provided in figure 1. Streamwise streaks can be seen to form upstream inlet, followed by streak oscillations and turbulent spots.

There are several reason for choosing this flow case as a flow-control test-bed. The dynamics governing the disturbance dynamics is well known and fairly complex. As a consequence, the dynamics is known to have similarities with sub-layer streaks in wall-bounded turbulent shear flow. However, the time and length scales in bypass transition are larger and slower, which simplify the experimental realization of the control.

2. Review of experimental demonstration of feedback control

An experimental demonstration of feedback control of bypass transition has been reported earlier (Lundell 2007). This experiment will now be reviewed in some detail. The data from this experiment will be used in two ways in this paper. One is as the experimental part in a combined numerical/experimental study and the second is as starting point for an analysis in which system identification (SI) is used to predict and indicate possible improvements.

2.1. Setup

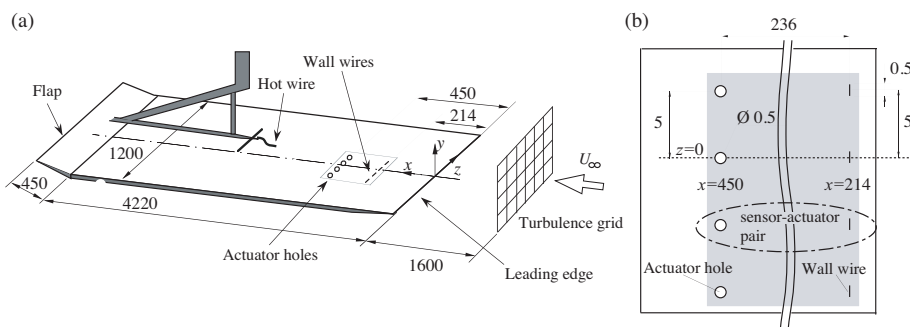


FIGURE 2. (a) Setup and (b) close up of a control unit. Measures are in mm.

A schematic of the setup is shown in figure 2 (a). The experiments were performed on a flat plate in the MTL wind tunnel at Royal Institute of Technology, Stockholm. Free-stream turbulence was generated by a grid upstream of the plate and the velocity was measured by a hot wire traversed in the flow. The disturbances in the boundary layer over the plate was controlled by one or

two control units and one control unit is depicted in figure 2 (b). Two turbulent generating grids are used, one giving a free-stream turbulence level at the leading edge (Tu) of 1.4% and one giving 2.5%. In the first case one control unit is used and in the latter both one and two are used. In the case with more intensive free-stream turbulence, transition occurs within the measured area.

2.1.1. Uncontrolled flow

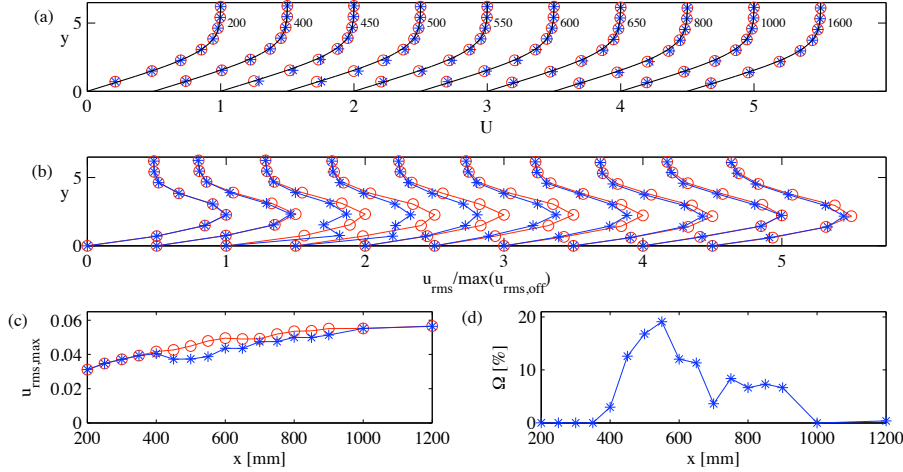


FIGURE 3. (a) Mean flow, (b) disturbance profiles, (c) disturbance growth and (d) disturbance attenuation in the experiments of Lundell (2007) (Lundell 2007). Without control (rings, red) and with control (stars, blue), $Tu = 1.4\%$. The line in (a) is the laminar Blasius solution.

The mean velocity and disturbance profiles and streamwise disturbance growth of the uncontrolled flow ($Tu = 1.4\%$) is illustrated with the circles in figure 3 (a–c). The mean velocity profiles at different streamwise positions in (a) (marked with the circles) are seen to agree well with the Blasius solution for a laminar zero-pressure-gradient boundary layer (shown with the solid line). The disturbance profiles in (b) show the typical disturbance structure in bypass transition: a maximum in the centre of the boundary layer. The disturbances are seen to grow in the streamwise direction in (c).

2.1.2. Control system

The control units consisted of sensors and actuators. The sensors were wall wires (0.5 mm long) giving a signal indicating the instantaneous local streamwise shear-stress. The actuators were holes (0.5 mm diameter) through which suction was turned on and off by fast solenoid valves. The sensors and actuators

were connected in pairs so that the suction through an actuator hole was controlled by the sensor straight upstream of it. The control logic (controller) was such that the suction was turned on and off with a delay whenever the streamwise shear (as sensed by the sensor) crossed a threshold. The suction was turned on at instants of low shear stress (indicating the passage of a low speed streak). Each control unit consisted of four neighbouring sensor-actuator-pairs and the two units were positioned at $x = 214\text{--}450$ mm and $x = 483\text{--}763$ mm. The lower value is the position of the sensor and the higher the position of the actuator.

The control system depends on the three variables threshold, delay and suction strength. These parameters were varied during the experiments to obtain a good control effect. Detailed descriptions of the setup and parameter variations are found in the previous publication (Lundell 2007).

2.2. Disturbance attenuation

The effect of the control is measured by studying the attenuation of the maximum of u_{rms} at different positions. The disturbance attenuation is quantified as

$$\Omega_{rms} = 1 - \frac{u_{rms,max,on}}{u_{rms,max,off}}, \quad (1)$$

so that Ω_{rms} is the relative decrease of the disturbance level in the boundary layer due to the control.

2.2.1. Case low, $Tu=1.4\%$

In this case, the control unit at $x = 214\text{--}450$ mm was used. The results of the control at the low turbulence level are shown in figure 3 (without control with circles and with control with stars). The mean velocity profiles at different streamwise positions in (a) show that there are only minute differences due to the control. Larger effects are seen in the disturbance level (b,c,d). First, in (b), the disturbance level at the center of the boundary layer is seen to decrease with control applied. Over the control hole ($x = 450$ mm) there is an increase close to the wall due to the control suction. Further downstream, there is a consistent attenuation of the *rms*-level thanks to the control. This is further demonstrated in (c) where the maximum of u_{rms} is shown as a function of x . In (d), the maximum disturbance attenuation as measured by Ω is seen to be 20%. Further downstream the attenuation decreases. This is due to new disturbances generated by the free-stream turbulence and disturbances migrating in the spanwise direction.

2.2.2. Case high, $Tu=2.5\%$

The disturbance attenuation in the case with high turbulence level are shown in figure 4. In this case, the turbulence level is high enough to trigger transition within the measured area. Thus, the amplitude development in the streamwise direction (shown in (a)) show three distinct regions: first a linear growth

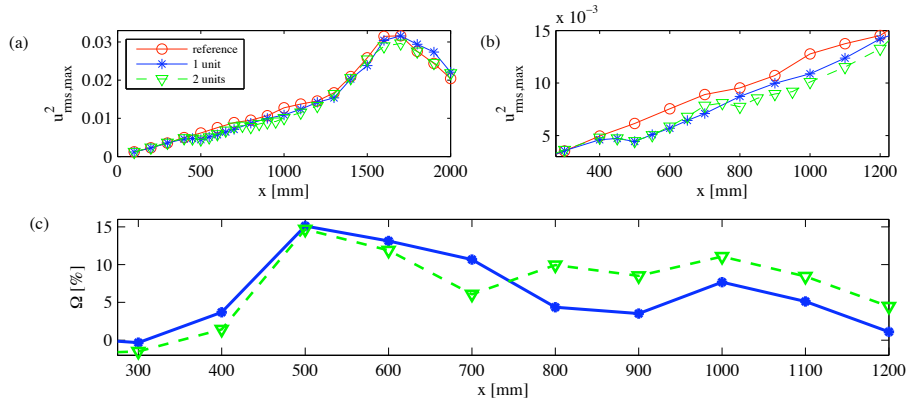


FIGURE 4. (a,b) Disturbance growth and (c) disturbance attenuation in the experiments of Lundell (2007) (Lundell 2007). Without control (rings, red), one control unit (stars, blue) and two control units (triangles, green), $Tu = 2.5\%$.

with low amplification (this is the growth of the streaks) followed by a more rapid growth to a maximum (attributed to secondary instabilities and intermittency) and finally a decrease towards the fully developed turbulent case. Both a single (the upstream) and both control units are applied. The control is seen to attenuate the disturbances and the maximum decrease is around 15%. The second control unit does not give a further increase of the disturbance attenuation. Nevertheless, it keeps the downstream attenuation at a higher value than with only the upstream unit.

No transition delay was obtained in these experiment. This was attributed to the fact that the controlled region was very narrow in the spanwise direction. Consequently, the controlled region is contaminated by turbulence from the sides.

3. Review of numerical simulations of feedback control

A short description of the previous work on feedback control of bypass transition is reported here (Monokrousos *et al.* 2008). The aim is to introduce the method and approach pursued. Bypass transition induced by high levels of free-stream turbulence above a boundary layer was simulated using direct numerical simulations (DNS) (Brandt *et al.* 2004) and large-eddy simulations (LES). A thorough study on different LES models was performed and the ADM-RT subgrid-scale model turned out to be particularly suited for this transitional flow (Monokrousos *et al.* 2008).

3.1. Method

A linear feedback control scheme was employed in order to reduce the perturbation energy and consequently delay transition. The case of bypass transition represents an extension of the linear approach (Chevalier *et al.* 2007) to flows characterised by strong nonlinearities. Control was applied by distributed blowing and suction at the wall. Initially, the control signal was based on the full knowledge of the instantaneous velocity field (i.e. full information control). Afterwards in order to relax this unphysical requirement possible only in a numerical simulation, an estimator based on wall measurements was built. This requires the simultaneous simulation of the real flow (plant) and of the estimated flow that is reconstructed from wall measurements only (the two components of the wall shear and the pressure in the present case).

Both the full information controller and the estimator are derived within the Linear Quadratic Gaussian (LQG) framework where a Linear Quadratic Regulator (LQR) is combined with a Kalman filter (Friedland 1986). Within this framework a set of linear equations of reduced complexity is used as a model for the physical process to be controlled; with the help of the Lagrange multiplier technique a constrained optimisation problem is formulated where a chosen quadratic objective function is minimised. The boundary layer flow is modeled by the Orr-Sommerfeld and Squire system governing the evolution of perturbations in parallel flows.

The control and estimation problem can be considered and solved separately. In the full-information control problem the objective function is the kinetic energy of the perturbation velocity. This quantity is minimised while the state of the flow satisfies the governing equation. In the estimation problem a new “state” is considered, the estimated flow, and the objective is to minimise the difference between the wall-measurements taken from the “real” and the estimated flow; still the perturbations are assumed to satisfy the linearized Navier-Stokes equations. However in the estimation problem a slightly different approach is used. The stochastic framework is employed where the system is assumed to be subject to stochastic excitations. Expected values of the estimation error are therefore examined (Hoepffner *et al.* 2005). The combination of an estimator and a full information controller is called compensator, where the control law is based on the estimated flow.

3.2. Summary of results

The results showed that the control was able to delay the growth of the streaks in the region where it is active, which eventually results in a delay of the whole transition process. In figure 5, the averaged skin friction coefficient and the wall-normal maximum of the streamwise velocity fluctuations are reported to show the transition location and the growth of the streaks inside the boundary layer, respectively. The flow field can be estimated from wall measurements alone: The structures occurring in the “real” flow are reproduced correctly in the region where the measurements are taken. Downstream of this region the

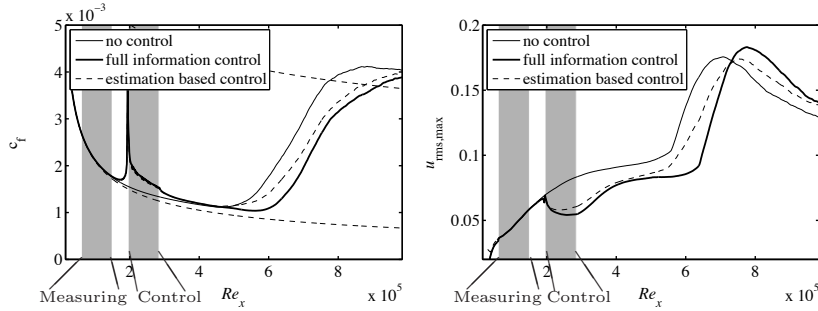


FIGURE 5. The skin friction coefficient and the wall-normal maximum of the streamwise perturbation velocity are shown for the uncontrolled case and for the simulations with full information control and estimation-based control.

estimated field gradually diverges from the “real” flow, revealing the importance of the continuous excitation of the boundary layer by the external stochastic free-stream turbulence. Control based on estimation, termed compensator, was therefore less effective than full information control. Additionally it was found that strong blowing can in fact promote transition due to non-linear effects and thus should be avoided.

4. Matching of LES and experiments

In the following we will attempt to apply the control strategy described in the previous section to a numerical simulation that resembles the experimental conditions of the $Tu = 2.5\%$ case. Once agreement in the disturbance development has been achieved, we will limit the actuation in the simulation to approach the physical characteristics of the control implemented in the experiment.

For the simulation the code employed (Chevalier *et al.* 2007) uses Fourier representation in the streamwise and spanwise directions and Chebyshev polynomials in the wall-normal direction. To correctly account for the downstream boundary-layer growth the spatial simulation approach is necessary. This requirement is combined with the periodic streamwise boundary condition by the implementation of a *fringe* region (Nordström *et al.* 1999). In this region, positioned at the downstream end of the computational box and occupying approximately 10% of the flow domain, a volume forcing is smoothly raised from zero to force the flow from the outflow to the desired inflow condition. The inflow consists of the laminar Blasius boundary layer with superimposed spatially and temporally varying disturbances mimicking the free-stream turbulence in the present case (Brandt *et al.* 2004).

4.1. Matching of the disturbance growth without control

The first task is to setup a numerical simulation of the flow that reproduces as close as possible the actual flow of the experiment. However, there are

TABLE 1. Computational box used. Resolution and box dimensions are shown. The box dimensions include the fringe region and are non-dimensionalised with respect to the displacement thickness δ_0^* at the inflow ($Re_{\delta_0^*} = 300$)

$L_x \times L_y \times L_z$	$N_x \times N_y \times N_z$
δ_0^*	(resolution)
$2250 \times 60 \times 96$	$576 \times 121 \times 64$

restrictions that make a perfect matching with the experiment virtually impossible. The two main differences are that (i) the code we employ can not include the leading edge and therefore perturbations cannot penetrate directly the boundary layer furthest upstream and (ii) the size of the computational domain is smaller than the wind-tunnel test section and therefore free-stream turbulence of smaller integral length scale can be simulated. The difference in length scales causes different decay rates of the external turbulence and thus different effects upon the underlying boundary layer. Note moreover that in a wider computational domain it would be too expensive to perform all the relevant simulations, especially the extensive parametric study that is performed to match the experimental results and test different control strategies. To facilitate our investigation, it was found that LES can give sufficiently good results. Thus we are aiming at a simulation that reproduces the main features of the conditions in the experiment and not an exact match.

A series of large eddy simulations was carried out to match as close as possible the disturbance growth seen in the experiment. The computational box parameters are reported in table 1. We vary the turbulence intensity and the integral length scale of the inlet free-stream turbulence and compare the growth of the wall-normal maximum of the streamwise velocity $u_{rms,max}$. We tried seven different length scales $l/\delta_0^* = 2.5, 3.5, 4.5, 5.5, 6.5, 7.5, 8.5$ and three turbulence intensities at the inlet, $Tu = 3, 3.5, 4\%$.

From figure 6 we see that the case with $Tu = 3.5\%$ and $l = 4.5\delta_0^*$ is closer to the experiment. This is evaluated in terms of initial growth and transition location. The parametric study performed confirms that transition is enhanced when increasing the turbulence intensity and the integral length scale of the turbulence, that is when reducing its decay rate downstream, see also Ref. Monokrousos *et al.* (2008). The turbulence level in the simulation matching the experiment is considerable higher than the one in the experiments. This is due to the fact that there is no leading edge and the integral length scale is shorter due to the limited width of the computational box in the simulations. The shorter length scale results in a faster decay. Consequently, a higher initial turbulence level is needed in the simulations.

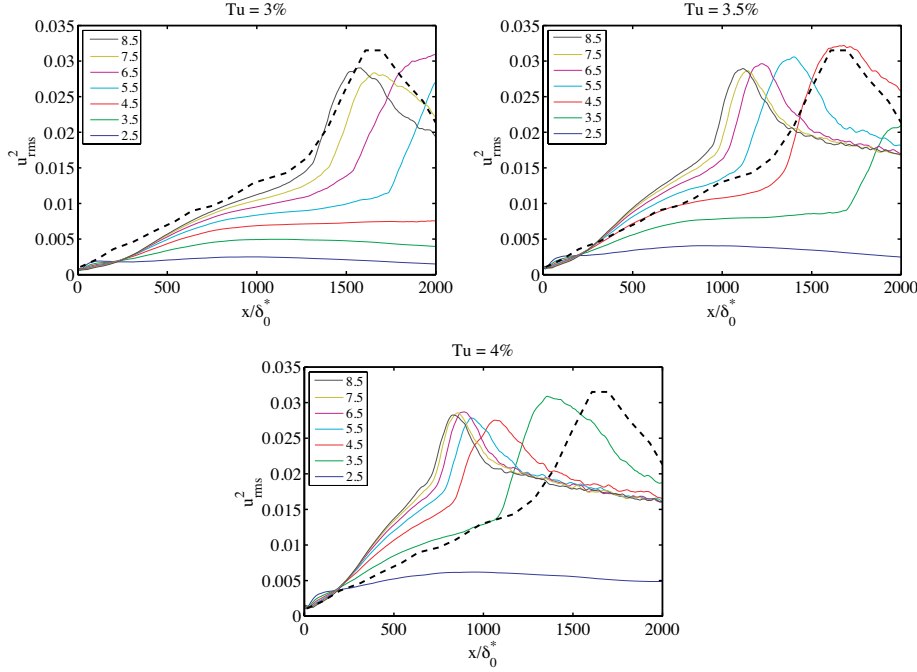


FIGURE 6. Wall-normal maximum of the streamwise velocity fluctuations u_{rms} . Each plot corresponds to a level of turbulence intensity and each line on the plots to different length scales of the free-stream turbulence at the inlet. The legend shows the length scale in δ_0^* units. The dashed black line indicates the experimental data.

4.2. Optimal control applied to the matched flow

In the following we will consider as reference uncontrolled case the simulation that was found to agree the most with the experiment (blue solid lines in the coming figures). In this study we are interested on the difference between distributed and localized actuation and in the effect of suction only; we therefore neglect the estimation problem and only consider the full-information control.

First we apply full information control as outlined in section 3.1 and Ref. Monokrousos *et al.* (2008). This case will provide the control reference case (green solid line in the figures). It can indeed be seen as the best possible performance active control can yield for our configuration. The wall-normal maximum of the u_{rms} and the attenuation factor Ω_{rms} are displayed in figure 7. It should be mentioned here that the control is applied at the stripe starting at $x = 350\delta_0^*$ and ends at $x = 550\delta_0^*$. A significant attenuation of the $u_{rms,max}$ as well as delay of the transition process can be seen.

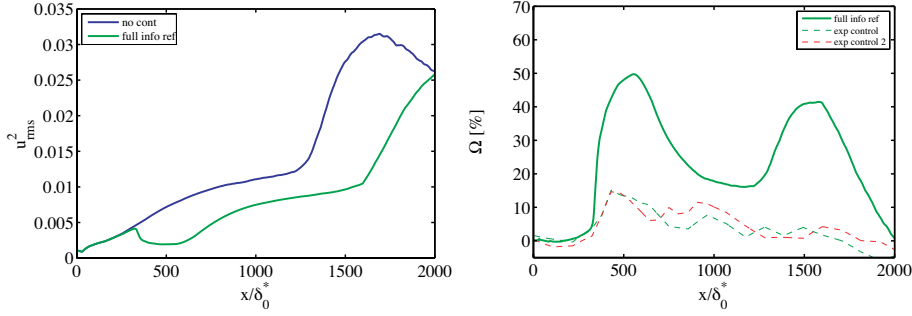


FIGURE 7. Wall-normal maximum of u_{rms} . Solid lines are simulations. Blue: reference case, Green line: control reference case. Dashed lines are experiments; green line: control with one control set red line: control with two control sets.

At this point it is useful to recall the differences between the actuator in the experiment and in the simulations. These pertain to the way the control signal is calculated and the area over which control is applied. In the experiment opposition control is adopted where the amplitude of the suction velocity and the time delay between the sensor and the actuator are varied. In the LES an optimization of the distributed control is performed and no further tuning is required. Note however that the control signal is computed assuming linearly evolving disturbances and parallel base flow. Secondly, it should be mentioned that the control is active over a large area of the plate where relatively weak blowing/suction is applied in the case of the numerical simulations. Conversely, small holes with strong suction velocity are used in the experiment. Further, in the LES we apply control over the full spanwise width of the domain while in the experiment control sets are only stationed near the middle of the plate at an area about 20 mm wide.

We will now try to wind down these differences. We will not change the control strategy in terms of the way the control signal is calculated but we will focus on the geometrical/functioning aspects of the actuator itself. In that context we will first remove the blowing and keep only the suction. After, we will restrict the area of actuation to spanwise stripes and finally we will also limit the streamwise extension of the area where suction is applied. In the latter last case, we will employ a “cheaper” control in order to result in stronger suction to better mimic the experiment.

In figure 8 we see three additional cases where the actuation characteristics are varied. In particular the first case we keep the actuation area the same but cut away all the blowing and keep the suction unchanged (red line in the figure), the second case we keep the blowing and suction unchanged but apply it only in spanwise streaks of width $5\delta_0^*$ (light blue line) with a center-to-center distance of $10\delta_0^*$ and finally combine the two above cases in both applying only suction

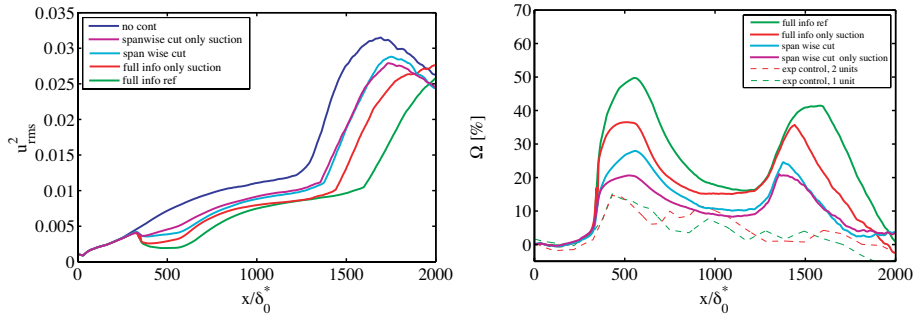


FIGURE 8. Wall-normal maximum of u_{rms} . Solid lines are simulations: blue: reference case, green line: control reference case, red line: control with only suction case, light blue: control with spanwise cut, purple: control with only suction and spanwise cut. Dashed lines as before.

and spanwise cutting of the signal (purple line). We see that the performance of the control in the LES is gradually degrading, approaching the experimental results. However the delay in the transition process remains.

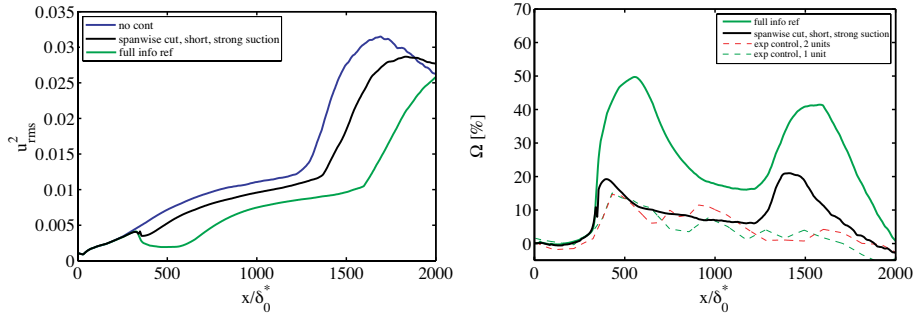


FIGURE 9. Wall-normal maximum of u_{rms} . Solid lines are simulations: blue: reference case, green line: control reference case, black line: control with only suction, spanwise and streamwise cut and cheaper control (stronger suction). Dashed lines as before.

Finally in figure 9 we see the results from the simulation where all the previous restriction on the actuator have been applied but also the streamwise extent of the control has been reduced from $200\delta_0^*$ to $20\delta_0^*$. Additionally we reduce the penalty put on the control during the design process from $l^2 = 10$ to $l^2 = 2$ (see Ref. Monokrousos *et al.* (2008)) resulting in stronger suction. In this last case the control effect is almost the same for both the experiment and the simulation near the actuation region but downstream there is a delay

of transition only for the numerical control. This can be explained by the fact that in the experiment control is applied near the middle of the plate and where transition occurs fully developed turbulence “invades” the controlled area from the uncontrolled sides.

5. System identification applied to experimental data

Linear system identification can be used to model system dynamics for prediction and control purposes (Ljung 1999). Here, linear filters will be identified from parts of the experimental time series. Independent data will be used to verify that the filters predict the measured disturbance attenuation. Based on the verified filters, a more efficient control signal is constructed and the estimated disturbance attenuation calculated.

5.1. System identification strategy and verification

Three signals are used in this work. They are (i) $W(t)$, the fluctuations from the wall-wire sensor, (ii) $U(x, y, t)$, the velocity fluctuations at the position $(x, y, z = 0)$ and (iii) $C(t)$, the digital signal controlling the suction at $(x = 450 \text{ mm}, z = 0)$.

The estimated systems will be used in two ways. The first is to use $W(t)$ and $C(t)$ from experiment and estimate the control effect. This is done to verify the ability of the estimated systems to predict the control result. The second possibility is to use a measured $W(t)$ and design a $C(t)$ which minimises future flow disturbances. This is done in order to show that considerable improvements might be possible.

The system connecting $W(t)$ and $C(t)$ to the velocity fluctuations is supposed to be:

$$U(x, y, t) = B_W(x, y)W(t) + B_C(x, y)C(t) + e(t) \quad (2)$$

where $e(t)$ is a sequence of random Gaussian noise and B_W and B_C are polynomials in the shift operator with a delay. With Δt as the sampling interval in time the polynomials have the form:

$$B_W W(t) = b_W^1 W(t - n_{k_W}) + b_W^2 W(t - \Delta t - n_{k_W}) + \dots + b_W^{n_{b_W}} W(t - n_{b_W} \Delta t - n_{k_W}). \quad (3)$$

Given the signals from the measurements, standard tools (Ljung 1999) are used to determine the orders n_{b_W} , n_{b_C} , the delays and n_{k_W} , n_{k_C} and the coefficients b_W^i , b_C^i .

Since the purpose of these efforts is to improve the disturbance attenuation by the control, the estimation process is verified by its ability to predict the measured disturbance attenuation. The estimated disturbance attenuation is defined as

$$\Omega_{est}(x, y) = 1 - \{B_W(x, y)W(t) + B_C(x, y)C(t)\} / B_W(x, y)W(t). \quad (4)$$

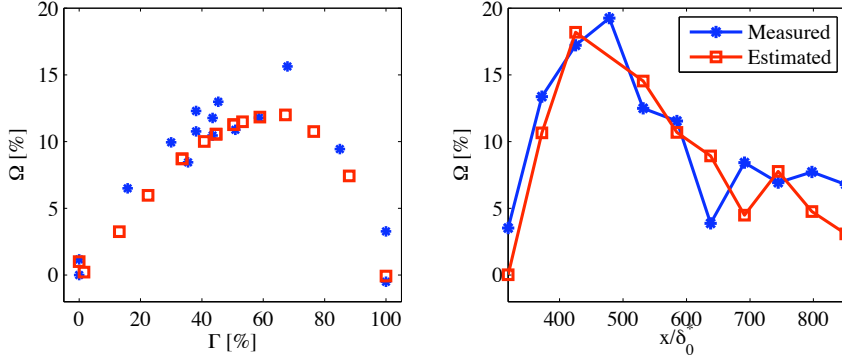


FIGURE 10. Verification of the ability of the system identification to reproduce the disturbance attenuation. Left: Varying the threshold in the controller, resulting in different $C(t)$ with different Γ . Note that only one set of filters B_W and B_C have been used. Right: Measured and estimated disturbance attenuation. For the estimation, one set of $W(t)$ and $C(t)$ (obtained by the threshold-and-delay controller) is used.

5.2. Verification of SI results

The first verification results are shown with stars and squares in figure 10 (a). The stars denote experimental data and the squares the estimated attenuation. The time fraction that the solenoid valves are open is varied. This is done by varying the threshold that the wall-shear-stress has to be below for the valve to be open (after a delay). Thus, for each time fraction an individual $W(t)$ and $C(t)$ are used as input for the estimation. The estimation process is seen to reproduce the measurements well.

This ability is further demonstrated in figure 10 (b), where the disturbance attenuation is shown as a function of streamwise position. The reference data without control applied is shown with stars and a dashed line. The stars with the full line show the measured fluctuation level with control applied. Also here, the estimated results are seen to predict the measured data.

5.3. Improved use of control effort

At this point, it has been demonstrated that the estimated system is able to reproduce the measured disturbance attenuation. The system will now be used to predict ultimate control performance. A good sequence $C(t)$ is determined as follows: at each time instant, the disturbance attenuation with and without control applied ($C = 1$ and $C = 0$) is estimated. The value of C at this time instant is then chosen as the one which gives the lowest disturbance level. This process is performed using data from the y -position of maximum fluctuations and $x/\delta_0^* = 530$. This gives a signal $C(t)$ and the Ω_{est} obtained when using it is

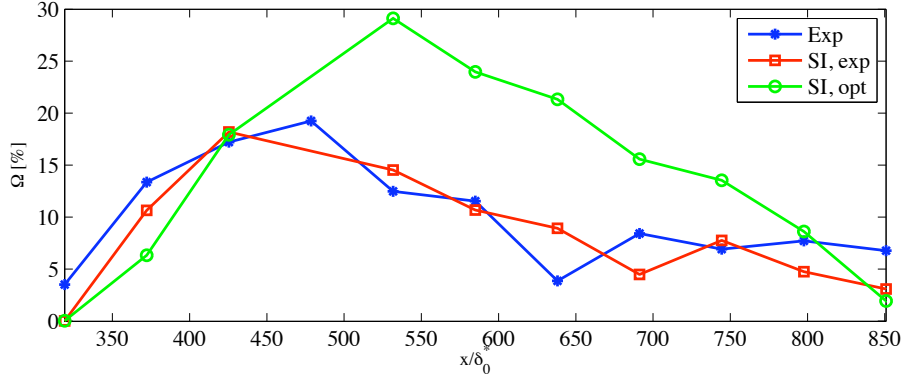


FIGURE 11. Disturbance attenuation obtained by the optimal $C(t)$.

shown with circles in figure 11. From $x/\delta_0^* = 530$ to $x/\delta_0^* = 800$ the disturbance reduction is about twice that obtained in the experiments.

The physical explanation behind these improvements can be understood by studying the step response from actuator to flow. From $x/\delta_0^* = 530$, the step response is non-monotonic and a controller more sophisticated than only linear cancellation (as used in the experiments) is necessary.

6. Conclusions

Feedback control of bypass transition has been studied. One experimental (Lundell 2007) (suction through holes triggered by threshold and delay) and one numerical (Monokrousos *et al.* 2008) (LQR with Kalman filter estimation) study are reviewed. A simulation giving a similar development of the disturbance amplitude as the experiment has been obtained and the LQR has been applied to this simulation. Furthermore, the control effect in one of the experimental cases have been modelled by linear system identification. The main observations are summarised below.

- The LQR with Kalman filter estimation with time and space varying blowing/suction gives much larger initial disturbance attenuation than the experiments (55% as compared to 15%) and a considerable transition delay.
- The initial disturbance attenuation in the simulations approaches the one obtained in the experiments if the capability of the actuator coupled to the LQR is limited towards the ability of the experimental ones (by (i) using only suction, (ii) limiting the actuation to limited spanwise positions and (iii) decreasing the streamwise length of the actuation).
- Compared to the case with complete actuation, a smaller, but still distinct, transition delay is obtained as the actuation ability is decreased.
- The linear system identification (SI) manages to predict the disturbance attenuation well.

- There are indications that SI could be used to improve the disturbance attenuation in future experiments.

Based on these observations, we find it plausible that an experiment in which the full span of the wind tunnel was controlled, would produce a transition delay. Furthermore, we are of the opinion that our results point out durable, flexible, small and cheap actuators as the most important missing technology if feedback control is to be applied to transitional flows for drag reduction. If less advanced actuators have to be used, it might be beneficial to consider their limitations in the controller design.

Acknowledgements

This work has relied on inspiration and support from professor D. S. Henningson and professor P. H. Alfredsson at KTH Mechanics. Financial support has been received from the Swedish Research Council.

References

- MATSUBARA, M. & ALFREDSSON, P. H. 2001 Disturbance growth in boundary layers subjected to free stream turbulence. *J. Fluid Mech.* **430**, 149–168.
- ANDERSSON, P., BERGGREN, M. & HENNINGSON, D. S. 1999 Optimal Disturbances and Bypass Transition in Boundary Layers. *Phys. Fluids* **11**, 134–150.
- LANDAHL, M. T. 1980 A note on an algebraic instability of inviscid parallel shear flows. *J. Fluid Mech.* **98**, 243–251.
- BRANDT, L., SCHLATTER, P. & HENNINGSON, D. S. 2004 Transition in boundary layers subject to free-stream turbulence. *J. Fluid Mech.* **517**, 167–198.
- MANS, J., DE LANGE, H. C. & VAN STEENHOVEN, A. A., 2007 Sinuous breakdown in a flat plate boundary layer exposed to free-stream turbulence. *Phys. Fluids* **19**, 088101.
- LUNDELL F. 2007 Reactive control of transition induced by free-stream turbulence: an experimental demonstration *J. Fluid Mech.* **585**, 41– 71.
- MONOKROUSOS, A., BRANDT, L., SCHLATTER, P. & HENNINGSON, D.S. 2008 DNS and LES of estimation and control of transition in boundary layers subject to free-stream turbulence. *Int. J. Heat and Fluid Flow* **29**, 841–855.
- CHEVALIER, M., HOEPFFNER, J., ÅKERVIK E. & HENNINGSON, D. S. 2007 Linear feedback control and estimation applied to instabilities in spatially developing boundary layers. *J. Fluid Mech.* **588**, 163–187.
- FRIEDLAND, B. 1986 Control system design: An introduction to state-space methods. *Dover, Mineola, New York*
- HOEPFFNER, J., CHEVALIER, M., BEWLEY, T. R. & HENNINGSON D. S. 2005 State estimation in wall-bounded flow systems. Part 1. Perturbed laminar flows. *J. Fluid Mech.* **534**, 263–294.
- CHEVALIER, M., SCHLATTER, P., LUNDBLADH, A. & HENNINGSON, D. S. 2007 SIMSON: A Pseudo-Spectral Solver for Incompressible Boundary Layer Flows. *KTH Mechanics, Stockholm 2007 Technical Report*, KTH/MEK/TR-07/07-SE
- NORDSTRÖM, J., NORDIN, N. & HENNINGSON, D. S. The fringe region technique and the Fourier method used in the direct numerical simulation of spatially evolving viscous flows. *SIAM J. Sci. Comp.* **20**, 1365–1393.
- LJUNG, L 1999 System Identification, theory for the user. *Prentice Hall, New York*.

Paper 3

3

Global optimal disturbances in the Blasius boundary-layer flow using time-steppers

By **Antonios Monokrousos, Espen Åkervik, Luca Brandt & Dan S. Henningson**

Linné Flow Centre, Department of Mechanics
Royal Institute of Technology, SE-100 44 Stockholm, Sweden

Submitted to the Journal of Fluid Mechanics

The global linear stability of the flat-plate boundary-layer flow to three-dimensional disturbances is studied by means of an optimisation technique. We consider both the optimal initial condition leading to the largest growth at finite times and the optimal time-periodic forcing leading to the largest asymptotic response. Both optimisation problems are solved using a Lagrange multiplier technique, where the objective function is the kinetic energy of the flow perturbations and the constraints involve the linearised Navier–Stokes equations. The approach proposed here is particularly suited to examine convectively unstable flows, where single global eigenmodes of the system do not capture the downstream growth of the disturbances. In addition, the use of matrix-free methods enables us to extend the present framework to any geometrical configuration. The optimal initial condition for spanwise wavelengths of the order of the boundary layer thickness are finite-length streamwise vortices exploiting the lift-up mechanism to create streaks. For long spanwise wavelengths it is the Orr mechanism combined with the amplification of oblique wave packets that is responsible for the disturbance growth. It is found that the latter mechanism is dominant for the long computational domain and thus for the relatively high Reynolds number considered here. Three-dimensional localised optimal initial conditions are also computed and the corresponding wave-packets examined. For short optimisation times, the optimal disturbances consist of streaky structures propagating and elongating in the downstream direction without significant spreading in the lateral direction. For long optimisation times, we find the optimal disturbances with the largest energy amplification. These are wave-packets of TS-waves with low streamwise propagation speed and faster spreading in the spanwise direction. The pseudo-spectrum of the system for real frequencies is also computed with matrix-free methods. The spatial structure of the optimal forcing is similar to that of the optimal initial condition, and the largest response to forcing is also associated with the Orr/oblique wave mechanism, however less so than in the case of the optimal initial condition. The lift-up mechanism is most efficient at zero frequency and degrades slowly for increasing frequencies. The response to localised upstream forcing is also discussed.

1. Introduction

The flat-plate boundary layer is a classic example of convectively unstable flows; these behave as broadband amplifiers of incoming disturbances. As a consequence, a global stability analysis based on the asymptotic behaviour of single eigenmodes of the system will not capture the relevant dynamics. From this global perspective all the eigenmodes are damped, and one has to resort to an input/output formulation in order to obtain the initial conditions yielding the largest possible disturbance growth at any given time and the optimal harmonic forcing. To do this, an optimisation procedure is adopted. The aim of this work is to investigate the global stability of the flow over a flat plate subject to external perturbations and forcing and to examine the relative importance of the different instability mechanisms at work, see discussion below. The approach adopted here can be extended to any complex flow provided a numerical solver for the direct and adjoint linearised Navier-Stokes equations is available.

Recently, the global stability of the spatially-evolving Blasius flow subject to two-dimensional disturbances has been studied within an optimisation framework by projecting the system onto a low-dimensional subspace consisting of damped Tollmien-Schlichting (TS) eigenmodes (Ehrenstein & Gallaire 2005). These results were extended by Åkervik *et al.* (2008), who found that by not restricting the spanned space to include only TS modes, the optimally growing structures could exploit both the Orr and TS wave packet mechanism and yield a substantially higher energy growth. The Orr mechanism was studied in the context of parallel shear flows using the Orr–Sommerfeld/Squire equations by Butler & Farrell (1992), who termed it the Reynolds stress mechanism. This instability extracts energy from the mean shear by transporting momentum down the mean momentum gradient through the action of the perturbation Reynolds stress. In other words disturbances that are tilted against the shear can borrow momentum from the mean flow while rotating with the shear until they are aligned with it. This mechanism is also referred to as wall-normal non-normality.

From the local point of view the TS waves appear as unstable eigenvalues of the Orr–Sommerfeld equation. In the global framework however the global eigenmodes belonging to the TS branch are damped (Ehrenstein & Gallaire 2005), and the evolution of TS waves consist of cooperating global modes that produce wave packets. Considering the model problem provided by the Ginzburg-Landau equation with spatially varying coefficients, Cossu & Chomaz (1997) demonstrated that the non-normality of the streamwise eigenmodes combined with local convective instabilities leads to substantial transient growth. This non-normality is revealed by the streamwise separation of the direct and adjoint global modes induced by the basic flow advection; it is therefore also termed streamwise non-normality (Chomaz 2005).

It is now well established that when incoming disturbances exceed a certain amplitude threshold the flat-plate boundary layer is likely to undergo transition due to three-dimensional instabilities arising via the lift-up effect (Ellingsen & Palm 1975; Landahl 1980). This transient growth scenario, where streamwise vortices induce streamwise streaks by the transport of the streamwise momentum of the mean flow, was studied for a variety of shear flows in the locally parallel assumption (c.f. Butler & Farrell 1992; Reddy & Henningson 1993; Trefethen *et al.* 1993). The extension to the non-parallel flat plate boundary layer was performed at the same time by Andersson *et al.* (1999) and Luchini (2000) by considering the steady linear boundary-layer equations parabolic in the streamwise direction. In these investigations the optimal upstream disturbances are located at the plate leading edge and a Reynolds number independent growth was found for the evolution of streaks at large downstream distances. Levin & Henningson (2003) examined variations of the position at which disturbances are introduced and found the optimal location to be downstream of the leading edge. In this study, also low-frequency perturbations were considered, still within the boundary layer approximation. In the global framework an interpretation of the lift-up mechanism is presented e.g. in Marquet *et al.* (2008): Whereas the TS mechanism is governed by a transport of the disturbances by the base flow, the lift-up mechanism is governed by a transport of the base flow by the disturbances. Inherent to the lift up mechanism is the component-wise transfer of momentum from the two cross-stream to the streamwise velocity component (component-wise non-normality).

The standard way of solving the optimisation problems involved in the determination of optimal initial condition (or forcing) is to directly calculate the matrix norm of the discretized evolution operator (or the pseudo-spectrum of the resolvent) of the system. In the local approach, where the evolution is governed by the Orr–Sommerfeld/Squire equations it is clearly feasible to directly evaluate the matrix exponential or to invert the relevant matrix. In the global approach it is in general difficult and in some cases impossible to build the discretized system matrix. One possible remedy is to compute a set of global eigenmodes with iterative methods and project the flow system onto the subspace spanned by these eigenvectors. The optimisation is then performed in a low dimensional model of the flow (Schmid & Henningson 2001; Ehrenstein & Gallaire 2005; Åkervik *et al.* 2007, 2008). However, the direct *matrix-free* approach followed here is preferable if not indispensable for more complicated flows. This amounts to introducing the adjoint evolution operator and solving the eigenvalue problem of the composite operator only using Direct Numerical Simulations. This approach is commonly referred to as a time-stepper technique (Tuckerman & Barkley 2000), and has been applied to several generic flow cases such as spherical Couette flow (Mamun & Tuckerman 1995), backward facing step flow (Blackburn *et al.* 2008), separation bubbles (Marquet *et al.* 2008) and the flat-plate boundary-layer flow subject to two-dimensional disturbances (Bagheri *et al.* 2009a).

Thus, in this paper we study the stability of the flat-plate boundary-layer flow subject to three-dimensional disturbances from a global perspective using a time-stepper technique. The base flow has two inhomogeneous directions, namely the wall-normal and streamwise, thereby allowing a decoupling of Fourier modes in the spanwise direction only. Both optimal initial condition and optimal forcing are therefore first considered for a range of spanwise wavenumbers, seeking to find the spanwise scale of the most amplified disturbances. In the case of optimal initial conditions, we optimise over a range of final times, while time-periodic optimal forcing are computed for a range of frequencies. In addition, we compute for the first time optimal initial conditions localised in space. The evolution of the resulting wave-packet is analysed in terms of flow structures and propagation speed.

Whereas the computation of optimal initial condition is known in the global time-stepper context (see references above), the formulation of the optimal forcing problem in this framework is novel. This enables us to compute the pseudo-spectrum of the non-normal governing operator with a matrix-free method. The latter type of analysis can have direct implications for flow control as well: The optimisation procedure allows us to determine the location and frequency of the forcing to which the flow under consideration is most sensitive.

The paper is organised as follows. Section 2 is devoted to the description of the base flow and the governing linearised equations. Section 3 and 4 describe the Lagrange approach to solving the optimisation problems defined by the optimal initial conditions and optimal forcing, respectively. The main results are presented in section 5; the paper ends with a summary of the main conclusions.

2. Basic steady flow, governing equations and adjoint system

We investigate the stability of the classical spatially-evolving two-dimensional flat-plate boundary-layer flow subject to three-dimensional disturbances. The computational domain starts at a distance x from the leading edge defined by the Reynolds number $Re_x = U_\infty x / \nu = 3.38 \cdot 10^5$ or $Re_{\delta^*} = 1.72 \sqrt{Re_x} = U_\infty \delta_0^* / \nu = 10^3$. Here U_∞ is the uniform free stream velocity, δ^* is the local displacement thickness and ν is the kinematic viscosity. We denote the displacement thickness at the inflow position δ_0^* . All variables are non-dimensionalised by U_∞ and δ_0^* . The corresponding non-dimensional inflow position is $x_0 = 337.7$. We solve the linearised Navier–Stokes equations using a spectral DNS code described in Chevalier *et al.* (2007) on a domain $\Omega = [0, L_x] \times [0, L_y] \times [0, L_z]$. The non-dimensional height of the computational box is $L_y = 30$ and the length is $L_x = 1000$, while the spanwise width is $L_z = 502.6$ is for the case of localised initial conditions or defined in each simulation by the Fourier mode under investigation. In the wall-normal y direction a Chebyshev-tau technique with $n_y = 101$ polynomials is used. In the streamwise and spanwise directions we assume periodic behaviour, hence allowing for a Fourier transformation of all variables. For the simulations presented here, the continuous variables are approximated by $n_x = 768$ and $n_z = 128$ Fourier

modes in the streamwise and spanwise direction respectively, whereas we solve for each wave-number separately in the spanwise direction when considering spanwise periodic disturbances, a decoupling justified by the spanwise homogeneity of the base flow. Since the boundary layer flow is spatially evolving a fringe region technique is used to ensure that the flow is forced back to the laminar inflow profile at $x = 0$ (Nordström *et al.* 1999). The fringe forcing is quenching the incoming perturbations and is active at the downstream end of the computational domain, $x \in [800, 1000]$, so that $x = 800$ can be considered as the effective outflow location, corresponding to $Re_x = 1.138 \cdot 10^6$. The steady state used in the linearisation is obtained by marching the nonlinear Navier–Stokes equations in time until the norm of the time derivative of the solution is numerically zero. Thus the two-dimensional steady state with velocities $\mathbf{U} = (U(x, y), V(x, y), 0)^T$ and pressure $\Pi(x, y)$ differs slightly from the well-known Blasius similarity solution.

2.1. The linearised Navier–Stokes equations

We are investigating the growth of small amplitude three-dimensional disturbances on a two-dimensional base flow. The stability characteristics of the base flow \mathbf{U} to small perturbations $\mathbf{u} = (u(\mathbf{x}, t), v(\mathbf{x}, t), w(\mathbf{x}, t))^T$ are determined by the linearized Navier–Stokes equations

$$\partial_t \mathbf{u} + (\mathbf{U} \cdot \nabla) \mathbf{u} + (\mathbf{u} \cdot \nabla) \mathbf{U} = -\nabla \pi + Re^{-1} \Delta \mathbf{u} + \mathbf{g}, \quad (1)$$

$$\nabla \cdot \mathbf{u} = 0, \quad (2)$$

subject to initial condition $\mathbf{u}(\mathbf{x}, t = 0) = \mathbf{u}_0(\mathbf{x})$. The boundary conditions for the perturbations are periodicity in x and z and homogeneous Dirichlet conditions in y . Note that we have included a divergence-free forcing term $\mathbf{g} = \mathbf{g}(\mathbf{x}, t)$ to enable us to also study the response to forcing as well as to initial condition. In the expression above, the fringe forcing term is omitted for simplicity (see Bagheri *et al.* 2009b).

When performing systematic analysis of the linearized Navier–Stokes equations we are interested in the initial condition $\mathbf{u}(0)$ and in the features of the flow states $\mathbf{u}(t)$ at times $t > 0$. We will also consider the spatial structure of the time-periodic forcing \mathbf{g} that creates the largest response at large times, that is when all transient effects have died out. Our analysis will therefore consider flow states induced by forcing or initial conditions, where a flow state is defined by the three-dimensional velocity vector field throughout the computational domain Ω at time t . To this end, it is preferable to re-write the equations in a more compact form. In order to do so we define the velocities as our state variable, *i.e.* $\mathbf{u} = (u, v, w)^T$, discarding the pressure π . An important observation can be made from equations (1) and (2); for incompressible flows the pressure only acts as a Lagrange multiplier to maintain divergence free velocity fields. We follow the notation of Kreiss *et al.* (1994) and let the forced linearized Navier–Stokes equations be written as

$$\partial_t \mathbf{u} = -(\mathbf{U} \cdot \nabla) \mathbf{u} - (\mathbf{u} \cdot \nabla) \mathbf{U} + Re^{-1} \Delta \mathbf{u} + \nabla \pi + \mathbf{g}, \quad (3)$$

where the pressure is a known function of the divergence free velocity field \mathbf{u} and base flow \mathbf{U}

$$\Delta\pi = -\nabla \cdot ((\mathbf{U} \cdot \nabla)\mathbf{u} + (\mathbf{u} \cdot \nabla)\mathbf{U}). \quad (4)$$

Inversion of the Laplacian requires boundary conditions, and formally we may obtain these by projecting (3) on the outwards pointing normal of the domain \mathbf{n} . If we let the solution of (4) be denoted as $\pi = \mathcal{K}\mathbf{u}$ we end up with the following expression for the system operator

$$\mathcal{A} = -(\mathbf{U} \cdot \nabla) - (\nabla\mathbf{U}) + Re^{-1}\Delta + \nabla\mathcal{K}. \quad (5)$$

The resulting state space formulation of equation (3) reads

$$(\partial_t - \mathcal{A})\mathbf{u} - \mathbf{g} = 0, \quad \mathbf{u}(0) = \mathbf{u}_0, \quad (6)$$

with solution

$$\mathbf{u}(t) = \underbrace{\exp(\mathcal{A}t)\mathbf{u}_0}_{\text{initial value problem}} + \underbrace{\int_0^t \exp(\mathcal{A}\tau)\mathbf{g}(\mathbf{x}, t - \tau) d\tau}_{\text{forced problem}}. \quad (7)$$

Alternatively \mathcal{A} may also be defined using semi-group theory, where it is referred to as an infinitesimal generator. First, the evolution operator $\mathcal{T}(t)$ is defined as the operator that maps a solution at time t_0 to time $t_0 + t$.

$$\mathbf{u}(t + t_0) = \mathcal{T}(t)\mathbf{u}(t_0). \quad (8)$$

The infinitesimal generator of $\mathcal{T}(t)$, \mathcal{A} , is defined through the action of \mathcal{T} for an infinitesimal amount of time δt

$$\mathcal{A}\mathbf{u} = \lim_{\delta t \rightarrow 0} \frac{\mathcal{T}(\delta t)\mathbf{u} - \mathbf{u}}{\delta t}. \quad (9)$$

For further explanation we refer to Trefethen & Embree (2005) or Bagheri *et al.* (2009b). In what follows we will utilise equation (7) to study both the response to initial condition, excluding the forcing terms, and the response to forcing excluding the initial value part, *i.e.* we look at the regime response. For practical numerical calculations the variables are often discretized, so that the operator \mathcal{A} becomes a matrix of size $n \times n$, with $n = 3n_x n_y n_z$ for general three-dimensional disturbances. When considering spanwise periodic disturbances we can focus on one wave number at the time and the dimension of the system matrix is reduced to $n = 3n_x n_y$. However, even in this case the evaluation of the discretized evolution operator $\exp(\mathcal{A}t)$ is computationally not feasible. The complete stability analysis, including the optimisation, can be performed only by considering solutions to (7), which is readily obtained by marching in time the linearised Navier–Stokes equations using a numerical code. This so called time stepper technique has indeed become increasingly popular in stability analysis (Tuckerman & Barkley 2000).

2.2. Choice of norm and the adjoint equations

In order to measure the departure from the base flow we introduce the norm based on the kinetic energy of the perturbations

$$\|\mathbf{u}(t)\|^2 = (\mathbf{u}(t), \mathbf{u}(t)) = \int_{\Omega} \mathbf{u}^H \mathbf{u} \, d\Omega. \quad (10)$$

This norm will be used extensively throughout this paper in order to systematically determine the optimal initial condition and optimal forcing. Having defined the inner product (10) we may derive the adjoint evolution operator. The adjoint evolution operator associated with the adjoint linearized Navier–Stokes equations is central to the optimisation framework when investigating the flow non-modal stability. Using the above inner product we may define the action of adjoint evolution operator as

$$(\mathbf{p}, \exp(\mathcal{A}t)\mathbf{u}) = (\exp(\mathcal{A}^\dagger t)\mathbf{p}, \mathbf{u}), \quad (11)$$

where \mathcal{A}^\dagger is defined by the initial value problem

$$-\partial_t \mathbf{p} = \mathcal{A}^\dagger \mathbf{p} = (\mathbf{U} \cdot \nabla) \mathbf{p} - (\nabla \mathbf{U})^T \mathbf{p} + Re^{-1} \Delta \mathbf{p} + \nabla \mathcal{Z} \mathbf{p}, \quad \mathbf{p}(T) = \mathbf{p}_T. \quad (12)$$

The adjoint system (12) is derived using the inner product in time space domain $\Sigma = [0, T] \times \Omega$. The operator \mathcal{Z} is the counterpart of the operator \mathcal{K} for the adjoint pressure: $\sigma = \mathcal{Z} \mathbf{p}$. For more details see Appendix Appendix A. This initial value problem has stable integration direction backwards in time so we may define the adjoint solution at time $T - t$ for the forward running time t as

$$\mathbf{p}(T - t) = \exp(\mathcal{A}^\dagger t) \mathbf{p}_T, \quad t \in [0, T]. \quad (13)$$

It is important to note that the addition of the forcing term \mathbf{g} in (3) has no effect on the derivation of the adjoint equations.

3. Optimal initial condition

In this section, the derivation of the system to be solved in order to find the initial conditions that optimally excites flow disturbances is reported. When seeking the optimal initial condition we assume that the forcing term \mathbf{g} in (6) is zero, so that only the first term on the right end side of (7) is of interest. We wish to determine the unit norm initial condition $\mathbf{u}(0)$ yielding the maximum possible energy $(\mathbf{u}(T), \mathbf{u}(T))$ at a prescribed time T . A common way of obtaining the optimal initial condition is to recognise that the condition

$$G(t) = \max_{\|\mathbf{u}(0)\| \neq 0} \frac{\|\mathbf{u}(T)\|^2}{\|\mathbf{u}(0)\|^2} = \max_{\|\mathbf{u}(0)\| \neq 0} \frac{\|\exp(\mathcal{A}T)\mathbf{u}(0)\|^2}{\|\mathbf{u}(0)\|^2} = \max_{\|\mathbf{u}(0)\| \neq 0} \frac{(\mathbf{u}(0), \exp(\mathcal{A}^\dagger T) \exp(\mathcal{A}T)\mathbf{u}(0))}{(\mathbf{u}(0), \mathbf{u}(0))} \quad (14)$$

defines the Rayleigh quotient of the composite operator $\exp(\mathcal{A}^\dagger T) \exp(\mathcal{A}T)$. The optimisation problem to be solved is hence the eigenvalue problem

$$\gamma \mathbf{u}(0) = \exp(\mathcal{A}^\dagger T) \exp(\mathcal{A}T) \mathbf{u}(0). \quad (15)$$

In the case of large system matrix, as in fluid-flow systems, this eigenvalue problem can be efficiently solved by matrix-free methods using a time-stepper (DNS) and perform power-iterations or the more advanced Arnoldi method (c.f. Nayar & Ortega 1993; Lehoucq *et al.* 1997); both methods only need a random initial guess for $\mathbf{u}(0)$ and a numerical solver to determine the action of $\exp(\mathcal{A}T)$ and $\exp(\mathcal{A}^\dagger T)$. An alternative approach to our optimisation problem relies on the use of the Lagrange multiplier technique. As show below, this will yield the same results for the problem considered here. However, within this framework, it is more straightforward to implement modifications in e.g. the function to maximise. When defining the problem, we need to define the objective function, in our case the kinetic energy of the perturbations at time T

$$\mathcal{J} = (\mathbf{u}(T), \mathbf{u}(T)). \quad (16)$$

Formally, the task is to maximise the above quadratic measure subject to two constraints: the flow needs to satisfy the governing linearized Navier–Stokes equations (6) (without forcing) and the initial condition must have unit norm $(\mathbf{u}(0), \mathbf{u}(0)) = 1$. Note that the second normalisation condition selects a unique solution of the eigenvalue problem (15) and thus enable the numerical procedure to converge. By introducing Lagrange multipliers (or costate variables) we may formulate an unconstrained optimisation problem for the functional

$$\mathcal{L}(\mathbf{u}, \mathbf{p}, \gamma) = (\mathbf{u}(T), \mathbf{u}(T)) - \int_0^T (\mathbf{p}, (\partial_t - \mathcal{A}) \mathbf{u}) \, d\tau - \gamma ((\mathbf{u}(0), \mathbf{u}(0)) - 1). \quad (17)$$

We thus need to determine \mathbf{u} , $\mathbf{u}(0)$, $\mathbf{u}(T)$, \mathbf{p} and γ such that \mathcal{L} is stationary, necessary condition for first order optimality. This can be achieved by requiring that the variation of \mathcal{L} is zero,

$$\delta \mathcal{L} = \left(\frac{\partial \mathcal{L}}{\partial \mathbf{u}}, \delta \mathbf{u} \right) + \left(\frac{\partial \mathcal{L}}{\partial \mathbf{p}}, \delta \mathbf{p} \right) + \left(\frac{\partial \mathcal{L}}{\partial \gamma}, \delta \gamma \right) = 0. \quad (18)$$

This is only fulfilled when all terms are zero simultaneously. The variation with respect to the costate variable (or adjoint state variable) yields directly the state equation

$$\left(\frac{\partial \mathcal{L}}{\partial \mathbf{p}}, \delta \mathbf{p} \right) \Rightarrow (\partial_t - \mathcal{A}) \mathbf{u} = 0, \quad (19)$$

and similarly the variation with respect to the multiplier γ yields a normalisation criterion

$$\left(\frac{\partial \mathcal{L}}{\partial \gamma}, \delta \gamma \right) \Rightarrow (\mathbf{u}(0), \mathbf{u}(0)) = 1. \quad (20)$$

In order to take the variations with respect to the other variables we perform integration by parts on the second term of \mathcal{L} in (17) to obtain

$$\begin{aligned} \mathcal{L} &= (\mathbf{u}(T), \mathbf{u}(T)) - \int_0^T (\mathbf{u}, (-\partial_t - \mathcal{A}^\dagger) \mathbf{p}) \, d\tau \\ &- (\mathbf{p}(T), \mathbf{u}(T)) + (\mathbf{p}(0), \mathbf{u}(0)) - \gamma ((\mathbf{u}(0), \mathbf{u}(0)) - 1). \end{aligned} \quad (21)$$

Note that the inner product between the direct and adjoint variables \mathbf{p} at the initial and end time is obtained in the integration, see derivation in Appendix Appendix A. The variation of this expression with respect to the state variable \mathbf{u} yields an equation for the adjoint variable as well as two optimality conditions

$$\left(\frac{\partial \mathcal{L}}{\partial \mathbf{u}}, \delta \mathbf{u}\right) \Rightarrow - \int_0^T (\delta \mathbf{u}, (-\partial_t - \mathcal{A}^\dagger) \mathbf{p}) + (\delta \mathbf{u}, \mathbf{p} - \gamma \mathbf{u})|_{t=0} + (\delta \mathbf{u}, \mathbf{u} - \mathbf{p})|_{t=T} = 0.$$

The simplest choice to satisfy this condition is each of these terms being separately zero so finally we get

$$(-\partial_t - \mathcal{A}^\dagger) \mathbf{p} = 0, \quad (22)$$

and

$$\begin{aligned} \mathbf{u}(0) &= \gamma^{-1} \mathbf{p}(0), \\ \mathbf{p}(T) &= \mathbf{u}(T). \end{aligned} \quad (23)$$

The optimality system to be solved is hence composed of equations (19), (20), (22) and (23). From (20) and the first relation in (23), it can readily be seen that $\gamma = (\mathbf{p}(0), \mathbf{p}(0))$. The remaining equations are solved iteratively as follows.

Starting with an initial guess $\mathbf{u}(0)^n$:

- (i) we integrate (19) forward in time and obtain $\mathbf{u}(T)$;
- (ii) $\mathbf{p}(T) = \mathbf{u}(T)$ is used as an initial condition at $t = T$ for the adjoint system (22), which integrated backward in time gives $\mathbf{p}(0)$;
- (iii) we determine a new initial guess by normalising, $\mathbf{u}(0)^{n+1} = \mathbf{p}(0)/\gamma$;
- (iv) if $|\mathbf{u}(0)^{n+1} - \mathbf{u}(0)^n|$ is larger than a given tolerance, the procedure is repeated.

Before convergence is obtained $\mathbf{u}(0)$ and $\mathbf{p}(0)$ are not aligned. At convergence, $\mathbf{u}(0)$ is an eigenfunction of (15). The iteration scheme above can be seen as a power iteration scheme finding the largest eigenvalue of the problem (15). Since the composite operator is symmetric its eigenvalues are real and its eigenvectors form an orthogonal basis. The eigenvalues of the system rank the set of optimal initial conditions according to the output energy at time T . If several optimals are sought, e.g. to build a reduced order model of the flow, the sequence of $\mathbf{u}(0)^n$ produced in the iteration can be used to build a Krylov subspace suitable for the Arnoldi method.

The formulation presented is extended to determine an optimal localised initial condition. In this case, the initial perturbation is forced to exist only inside a certain region Λ in space. The optimal shape contained within this region is determined by the optimisation procedure. The changes in the derivation of the optimality condition necessary for this case are detailed in Appendix Appendix B. The gradient of the objective function is defined only inside Λ and an additional multiplier is necessary to enforce the initial condition to be divergence free.

4. Optimal forcing

This section will focus on the regime response of the system to time-periodic forcing. Thus we assume zero initial conditions, $\mathbf{u}(0) = 0$, and periodic behaviour of the forcing function, *i.e.*

$$\mathbf{g} = \Re(\mathbf{f}(\mathbf{x}) \exp(i\omega t)), \quad \mathbf{f} \in \mathbb{C}, \quad \omega \in \mathbb{R}, \quad (24)$$

where \mathbf{f} defines the spatial structure of the forcing, ω is its circular frequency and \Re denotes the real part. With these assumptions, the governing equations become

$$(\partial_t - \mathcal{A})\mathbf{u} - \Re(\mathbf{f} \exp(i\omega t)) = 0, \quad \mathbf{u}(0) = 0. \quad (25)$$

In this case, we wish to determine the spatial structure and relative strength of the components of the forcing \mathbf{f} that maximise the response of the flow at the frequency ω in the limit of large times, *i.e.* the regime response of the flow. The measure of the optimum is also here based on the energy norm. Note that for this method to converge and for the regime response to be observed, the operator \mathcal{A} must be globally stable. In the spatial framework this requirement is always satisfied.

In order to formulate the optimisation problem it is convenient to work in the frequency domain, thereby removing the time dependence. By assuming time periodic behaviour, \mathbf{u} is replaced by the complex field $\tilde{\mathbf{u}}$ so that

$$\mathbf{u} = \Re(\tilde{\mathbf{u}} \exp(i\omega t)). \quad (26)$$

The resulting governing equations can then be written

$$(i\omega\mathcal{I} - \mathcal{A})\tilde{\mathbf{u}} - \mathbf{f} = 0. \quad (27)$$

Note that the operator \mathcal{A} , containing only spatial derivatives, remains unchanged. The objective function is the disturbance kinetic energy of the regime response,

$$\mathcal{J} = (\tilde{\mathbf{u}}, \tilde{\mathbf{u}}) = \int_{\Omega} \tilde{\mathbf{u}}^H \tilde{\mathbf{u}} \, d\Omega, \quad (28a)$$

where the complex variable $\tilde{\mathbf{u}}$ requires the use of the Hermitian transpose. The Lagrange function for the present optimisation problem is similar in structure to that used to determine the optimal initial condition and is formulated as follows.

$$\mathcal{L}(\tilde{\mathbf{u}}, \tilde{\mathbf{p}}, \gamma, \mathbf{f}) = (\tilde{\mathbf{u}}, \tilde{\mathbf{u}}) - (\tilde{\mathbf{p}}, (i\omega\mathcal{I} - \mathcal{A})\tilde{\mathbf{u}} - \mathbf{f}) - \gamma((\mathbf{f}, \mathbf{f}) - 1). \quad (29)$$

The additional constrains require the flow to be solution of the linearised Navier–Stokes equations and introduce a normalisation condition for the forcing amplitude. Since the state variable $\tilde{\mathbf{u}}$ is a solution of the time independent system (27), the inner product used in the definition of the adjoint involves only spatial integrals. The time behaviour of the costate or adjoint variable is indeed assumed to be also periodic

$$\mathbf{p} = \Re(\tilde{\mathbf{p}} \exp(i\omega t)). \quad (30)$$

Thus, the derivation will proceed as reported in Appendix Appendix A, only without the time integral: the time derivative is replaced by the term $i\omega\tilde{\mathbf{u}}$, with adjoint $-i\omega\tilde{\mathbf{p}}$.

As for the computation of the optimal initial condition, we take variations with respect to $\tilde{\mathbf{u}}$, $\tilde{\mathbf{p}}$, \mathbf{f} and γ

$$\delta\mathcal{L} = \left(\frac{\partial\mathcal{L}}{\partial\tilde{\mathbf{u}}}, \delta\tilde{\mathbf{u}}\right) + \left(\frac{\partial\mathcal{L}}{\partial\tilde{\mathbf{p}}}, \delta\tilde{\mathbf{p}}\right) + \left(\frac{\partial\mathcal{L}}{\partial\mathbf{f}}, \delta\mathbf{f}\right) + \left(\frac{\partial\mathcal{L}}{\partial\gamma}\right)\delta\gamma. \quad (31)$$

The first order optimality condition requires all of the terms to be simultaneously zero. By taking variations with respect to the costate variable (or adjoint variable) we again obtain the state equation

$$\left(\frac{\partial\mathcal{L}}{\partial\tilde{\mathbf{p}}}\right) \Rightarrow -(i\omega\mathcal{I} - \mathcal{A})\tilde{\mathbf{u}} + \mathbf{f} = 0, \quad (32)$$

and similarly the variation with respect to the multiplier γ yields a normalisation criterion

$$\left(\frac{\partial\mathcal{L}}{\partial\gamma}\right) \Rightarrow (\mathbf{f}, \mathbf{f}) - 1 = 0. \quad (33)$$

In order to take the variations with respect to the other variables we perform integration by parts on the second term of \mathcal{L} in (29) to obtain

$$\mathcal{L}(\tilde{\mathbf{u}}, \tilde{\mathbf{p}}, \gamma, \mathbf{f}) = (\tilde{\mathbf{u}}, \tilde{\mathbf{u}}) - (\tilde{\mathbf{u}}, (-i\omega\mathcal{I} - \mathcal{A}^\dagger)\tilde{\mathbf{p}}) + (\mathbf{f}, \tilde{\mathbf{p}}) - \gamma((\mathbf{f}, \mathbf{f}) - 1). \quad (34)$$

No initial-final condition terms appear during this integration by parts since here the inner product is only in space (in contrast to the optimal initial condition). The spatial boundary terms cancel owing to the chosen boundary conditions as seen in Appendix Appendix A. Variations with respect to the state variable $\tilde{\mathbf{u}}$ and to the forcing function \mathbf{f} yield

$$\left(\frac{\partial\mathcal{L}}{\partial\tilde{\mathbf{u}}}\right) \Rightarrow \tilde{\mathbf{u}} - (-i\omega\mathcal{I} - \mathcal{A}^\dagger)\tilde{\mathbf{p}} = 0, \quad (35)$$

$$\left(\frac{\partial\mathcal{L}}{\partial\mathbf{f}}\right) \Rightarrow \mathbf{f} = \gamma^{-1}\tilde{\mathbf{p}}. \quad (36)$$

Equations (32) and (35) provide the two equations we have to solve, equation (33) gives the normalisation condition and (36) provides the optimality condition that is used to calculate the new forcing field after each iteration of the optimisation loop.

Next, we show the equivalence between the Lagrange multiplier technique and the corresponding standard matrix method when the resolvent norm is considered. The formal solution of equation (25) can be written as.

$$\tilde{\mathbf{u}} = (i\omega I - \mathcal{A})^{-1}\mathbf{f}. \quad (37)$$

The corresponding solution for the adjoint system

$$\tilde{\mathbf{p}} = (-i\omega I - \mathcal{A}^\dagger)^{-1}\tilde{\mathbf{u}}. \quad (38)$$

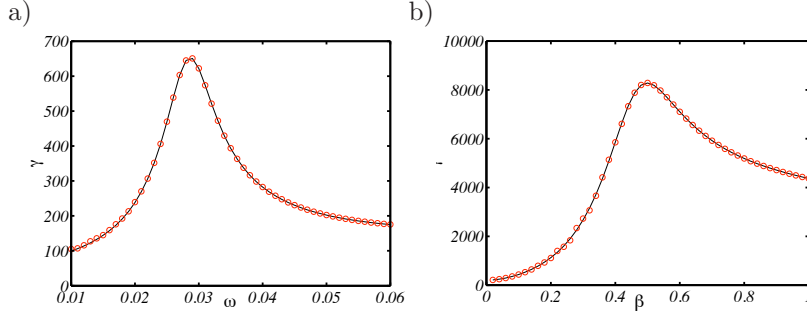


FIGURE 1. Comparison of results from the adjoint iteration scheme (shown as circles) and direct solution in terms of SVD of the OSS resolvent (shown as solid lines) for optimal forcing to the parallel Blasius flow at $Re = 1000$. a) Zero spanwise wave-number β for different frequencies ω and for streamwise wave-number $\alpha = 0.1$. b) Streamwise wave-number $\alpha = 0.1$ for different spanwise wave-numbers β subject to forcing with frequency $\omega = 0.05$. Both plots shows excellent agreement between the two methods. Note that in order to obtain a regime response in the parallel case the wave-numbers are chosen so that the system operator is stable.

Combining the two equations above and using (36)

$$\mathbf{f} = \frac{1}{\gamma} (-i\omega I - \mathcal{A}^\dagger)^{-1} (i\omega I - \mathcal{A})^{-1} \mathbf{f}. \quad (39)$$

This is a new eigenvalue problem defining the spatial structure of the optimal forcing at frequency ω that is solved iteratively; the largest eigenvalue corresponds to the square of the resolvent norm

$$\gamma = \|(i\omega I - \mathcal{A})^{-1}\|^2. \quad (40)$$

Note that the actual implementation is using a slightly different formulation, since the available time-stepper does not solve directly (32) and (35). In practice, the governing equations are integrated in time long enough that the transient behaviour related to the system operator \mathcal{A} has died out. The regime response for the direct and adjoint system is extracted by performing a Fourier transform of the velocity field during one period of the forcing.

The steps of the optimisation algorithm therefore are:

- (i) Integrate (25) forward in time and obtain the Fourier transform response $\tilde{\mathbf{u}}$ at the frequency of the forcing.
- (ii) $\tilde{\mathbf{u}}$ is used as a forcing for the adjoint system which in time domain is written

$$(-\partial_t - \mathcal{A}^\dagger)\mathbf{p} - \Re(\tilde{\mathbf{u}} \exp(i\omega t)) = 0. \quad (41)$$

- (iii) A new forcing function is determined by normalising $\mathbf{f}^{n+1} = \tilde{\mathbf{p}}/\gamma$.
- (iv) If $|\mathbf{f}^{n+1} - \mathbf{f}^n|$ is larger than a given tolerance, the procedure is repeated.

A validation of the method is presented in figure 1, where the results from the present adjoint-based iteration procedure are compared to those obtained by the standard method of performing a singular value decomposition (SVD) of the resolvent of the Orr–Sommerfeld and Squire equations for the parallel Blasius flow (c.f. Schmid & Henningson 2001). In figure 1a) the response to forcing with spanwise wave-number $\beta = 0$ is shown for different frequencies, whereas the response to steady forcing with streamwise wave-number α is shown in figure 1b). In the latter case, variations of the spanwise wave-numbers are considered. In both cases, excellent agreement between the two methods is observed.

5. Results

The flat plate boundary layer flow is globally stable, *i.e.* there are no eigenvalues of \mathcal{A} located in the unstable half plane. Hence we do not expect to observe the evolution of single eigenmodes. In Åkervik *et al.* (2008) the non-modal stability of this flow subject to two-dimensional disturbances was studied by considering optimal superposition of eigenmodes. These authors found that the optimal initial condition exploits the well known Orr mechanism to efficiently trigger the propagating Tollmien–Schlichting wave packet. In Bagheri *et al.* (2009a), the stability of the same flow was studied using forward and adjoint iteration scheme together with the Arnoldi method to reproduce the same mechanism. By allowing for three-dimensional disturbances, it is expected that in addition to the instability mechanisms mentioned above (convective Tollmien–Schlichting instability and the Reynolds stress mechanism of Orr) the lift-up mechanism will be relevant in the system.

This has been well understood both using the Orr–Sommerfeld/Squire equations (Butler & Farrell 1992; Reddy & Henningson 1993) in the parallel temporal framework and using the Parabolized Stability Equations in the spatial non-parallel framework (Andersson *et al.* 1999; Luchini 2000; Levin & Henningson 2003). In the former formulation, the base flow is assumed to be parallel. At the Reynolds number $Re = 1000$, the inflow Reynolds number of the present investigation, it is found that for spanwise wave-numbers β larger than ≈ 0.3 there is no exponential instability of TS/oblique waves. The largest non-modal growth due to the lift-up mechanism is observed at the wave-number pair $(\alpha, \beta) = (0, 0.7)$. In the present work we do not restrict ourselves to zero streamwise wave-number $\alpha = 0$, but instead we take into account the developing base flow. Indeed the spatially developing base flow allows for transfer of energy between different wave-numbers through the convective terms.

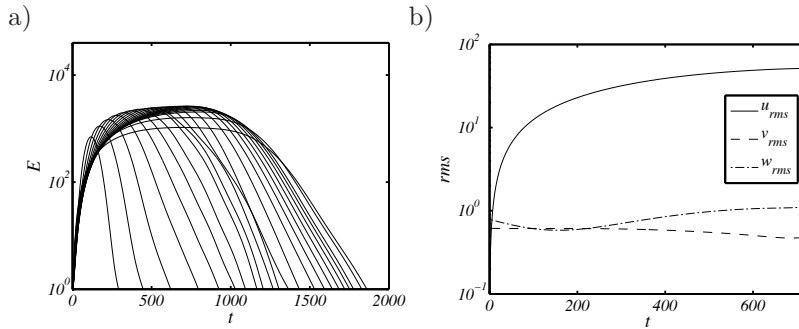


FIGURE 2. a) Energy evolution of the optimal initial conditions for different times T at the wave-number $\beta = 0.55$, where the optimal streak growth is obtained. The largest growth is obtained at time $T = 720$. The maximum at each time in this figure defines the envelope growth. b) Component-wise rms-values when optimising for time $T = 720$. A transfer of energy from the wall-normal and spanwise component to the streamwise velocity is observed during the time evolution, clearly showing that the lift-up mechanism is active.

5.1. Optimal initial condition

5.1.1. Spanwise periodic flows

We investigate the potential for growth of initial conditions with different spanwise wave-numbers β by solving the eigenvalue problem (15) for a range of instances of time T . This amounts to performing a series of direct and adjoint numerical simulations until convergence towards the largest eigenvalues of (15) at time T is obtained. If only the largest eigenvalue of (15) is desired it suffices to use a power iteration scheme, whereas if several of the leading eigenvalues are needed, one has to resort to a Krylov/Arnoldi procedure (c.f. Nayar & Ortega 1993; Lehoucq *et al.* 1997). Both of these approaches are matrix-free and rely on the repeated action of $\exp(\mathcal{A}^\dagger T) \exp(\mathcal{A} T)$ on an initial velocity field $\mathbf{u}(0)$. In other words, it is not necessary to store matrices in order to obtain the eigenvalues but to time-integrate the governing equations.

Figure 2a) shows the energy evolution when optimising for different times and for spanwise wave-number $\beta = 0.55$. It is at this wave number that the maximum growth due to the lift-up mechanism is found for the configuration under consideration. From figure 2b) it is evident that the disturbance leading to the maximum streak growth at time $T = 720$ exploits the component-wise transfer between velocity components, inherent to the lift-up mechanism. The initial condition is in fact characterised by strong wall-normal v and spanwise w perturbation velocity while the flow at later times is perturbed in its streamwise velocity component.

An important feature of this high Reynolds number flat-plate boundary-layer flow with length $L_x = 800$ is that the combined Orr/Tollmien-Schlichting mechanism is very strong with a growth potential of $\gamma_1 = 2.35 \cdot 10^4$ (see also Bagheri *et al.* 2009a) for time $T = 1800$. If, however, the streaks induced by the lift-up mechanism have reached sufficiently large amplitudes to trigger significant non-linear effects, the TS wave transition scenario will be by-passed. In figure 3 a contour map of the maximum growth versus optimisation time and spanwise wave-numbers β is shown. Note that local maxima are obtained in two regions; (I) a low spanwise wave-number regime dominated by the TS/oblique waves where the growth is the largest but slow. (II) For high spanwise wave-number it is the fast lift-up mechanism that is dominating. The TS/oblique mechanism can be seen to yield one order of magnitude larger growth than the lift-up instability. The global maximum growth is obtained at the wave-number $\beta = 0.05$ and not for $\beta = 0$. This somewhat surprising result can be explained by the larger initial transient growth of spanwise-dependent perturbations which initiates the TS-waves. The growth rate of the latter is almost independent of β for the low values under consideration (see e.g. figure 3.10 in Schmid & Henningson 2001).

The competition between the exponential and algebraic growth was also studied using local theory by Corbett & Bottaro (2000). These authors have shown that as the Reynolds number increases, the growth due to modal instability becomes more pronounced. The results presented in that work for $Re_\theta = 386$ (equivalent to $Re_{\delta^*} = 1000$ in our scaling) indicate that TS instability becomes dominant for final times $T > 2000$. Our results show that in a spatially evolving boundary layer with local Reynolds number Re_{δ^*} ranging between 1000 and 1800 the exponential growth dominates at times larger than about 1250. In the following we study in more detail the disturbances corresponding to the two local maxima mentioned above.

The evolution of the most dangerous initial condition is shown in figure 4. The streamwise velocity component of the optimal initial condition leading to the maximum growth at time $T = 1820$ is depicted together with the flow response at various times. The initial disturbance is as in the two-dimensional case leaning against the shear of the base flow (see figure 4a). The resulting instability exploits the Orr-mechanism to efficiently initialise the wave packet propagation, eventually giving the disturbance shown in figures 4 b), c) and d).

Figure 5 shows the space-time diagram for the evolution of the three velocity components of the disturbance. Isocontours of the integrated- in spanwise and wall-normal direction- energy associated to each component are plotted versus the streamwise direction and time. Since this is a modal instability there is no significant component-wise transfer of energy and thus the different components of the disturbance evolve (grow) in a similar manner. Additionally, the propagation velocity of the disturbance is estimated from the space-time diagrams. The leading edge of the wave-packet travels at $c_{le} = 0.51$ while the

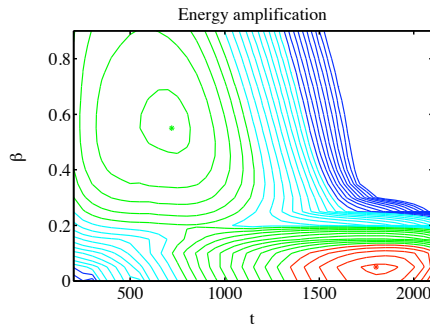


FIGURE 3. Contour map of optimal growth due to initial condition in the time spanwise wave-number domain. The contour levels span four orders of magnitude and thus we use a logarithmic scale. The blue lines are of order $10 - 10^2$, the light blue $10^2 - 10^3$, the green $10^3 - 10^4$ and the red $10^4 - 10^5$. For each level we define 10 contour lines but only levels present in the actual data are visible. The maximum streak growth is obtained for $\beta = 0.55$ at time $T = 720$ and the amplification factor is $G = 2.63 \cdot 10^3$. The global maximum is obtained for $\beta = 0.05$ at time $T = 1820$, with the streamwise exponential amplification of oblique waves combined with the Orr-mechanism. The amplification factor is $G = 2.71 \cdot 10^4$.

trailing edge has a velocity $c_{te} = 0.33$. These values shows remarkable agreement with the classic results on the propagation of wave-packets by Gaster (1975) and Gaster & Grant (1975).

The optimal initial condition leading to the maximum growth at time $T = 720$ for spanwise wave-number $\beta = 0.55$ and the corresponding flow response at various times are shown figure 6. The initial disturbance is an elongated perturbation with most of its energy (99.94%) in the wall-normal and spanwise velocity components (figure 6a). The resulting instability exploits the lift-up eventually giving the disturbance shown in figures 6 b), c) and d). This is a non-modal instability characterised by the strong transfer of energy from the wall-normal and spanwise towards the streamwise velocity component. Already at time $t = 100$ more than 99% of the kinetic energy of the perturbation is in the streamwise component. As it can be seen the disturbance evolves into alternating slow and fast moving streaks that are tilted so that the leading edge is higher than the trailing edge as observed in the experimental investigation by Lundell & Alfredsson (2004).

It is also interesting to note that while the optimal initial condition is streamwise independent for parallel flows, it is localised in the streamwise direction for a spatially growing boundary layer. This indicates that it is most

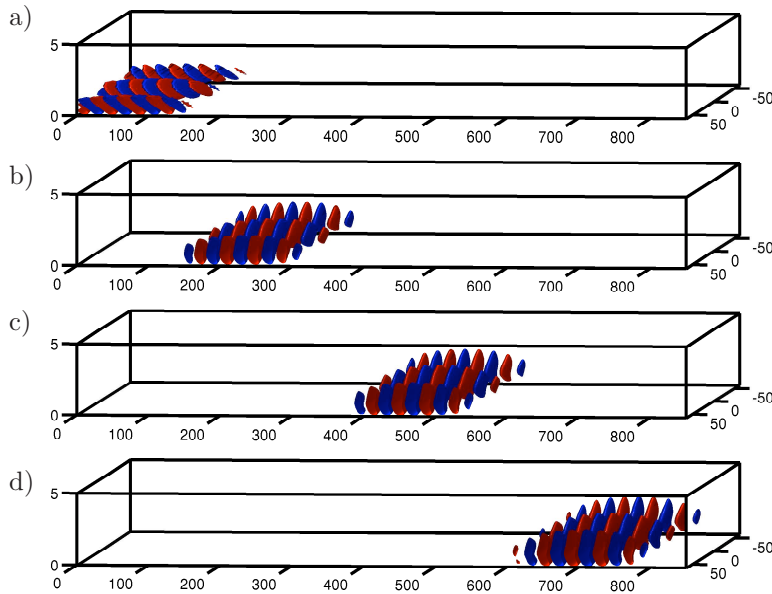


FIGURE 4. Isosurfaces of streamwise component of disturbances at the spanwise wave-number $\beta = 0.05$. Red/blue colour signifies isosurfaces corresponding to positive/negative velocities at 10 percent of the maximum. a) Streamwise component of optimal initial condition leading to the global optimal growth at time $T = 1820$. b), c) and d) Corresponding flow responses at times $T = 400, 1000$ and 1600

efficient to extract energy from the mean flow further upstream where nonparallel effects are stronger. For optimisation times longer than that pertaining the peak value, still with $\beta = 0.05$, the initial perturbation is located further upstream and is shorter. This is to compensate for the downstream propagation of perturbations out of the control domain. Conversely, for optimisation times lower than $T = 720$, the initial conditions assumes more and more the form of a packet of vortices aligned in the streamwise direction and tilted upstream. The growth is then due to a combined Orr and lift-up mechanism.

The space-time diagram for each velocity component of the streaky optimal perturbation is presented in figure 7. The non-modal nature of the instability and the component wise transfer of energy are seen in the plots. The streamwise component is for large times several orders of magnitude larger than the other two. The propagation velocity of the disturbance is calculated: the leading edge velocity of the “streak-packet” is $c_{le} = 0.87$ while the trailing edge travels at velocity $c_{te} = 0.44$. Note that these values are based on the streamwise velocity component. The propagation velocities of the non-modal streaks are larger than those pertaining modal disturbances. This can be explained by

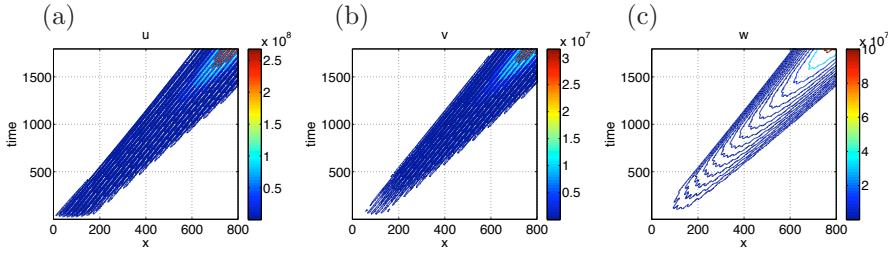


FIGURE 5. Space-Time diagram of the three velocity components of the perturbation for the TS-wave case ((a) streamwise, (b) wall-normal and (c) spanwise). The propagation velocity of the leading edge of the disturbance is $c_{le} = 0.51$ while of the trailing edge is $c_{te} = 0.33$.

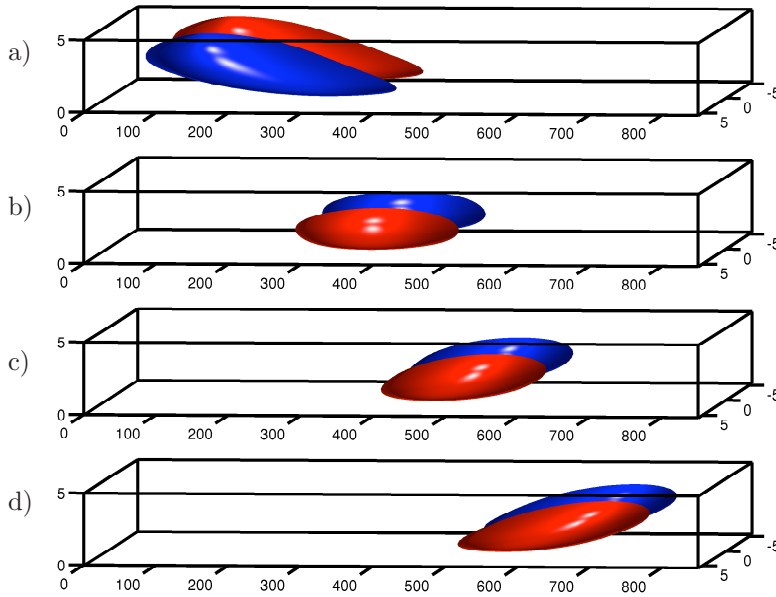


FIGURE 6. Evolution of streamwise velocity when initialising the system with the optimal initial condition at $\beta = 0.55$. a) The wall-normal velocity of the optimal initial condition. b) The streamwise velocity at $t = 200$ with surface levels at ten percent of its maximum value, c) at time $t = 400$ and d) at time $t = 600$.

the fact that the disturbances are located in the upper part of the boundary layer, especially the downstream part of it, as deduced also from the three-dimensional visualisation in figure 6. Note finally in the plot for the spanwise velocity component a kink around $t = 400$ and $x = 400$. In this region, the main

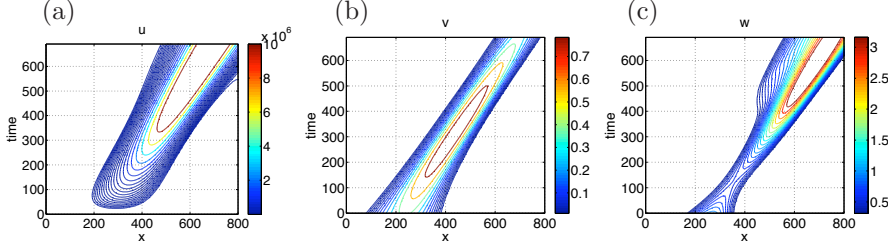


FIGURE 7. Space-Time diagram of the three velocity components of the perturbation for the streak case ((a) streamwise, (b) wall-normal and (c) spanwise). The propagation velocity of the leading edge of the disturbance is $c_{le} = 0.87$ while of the trailing edge is $c_{te} = 0.44$. The two speeds are measured in the second half of the time domain after the initial transient phase.

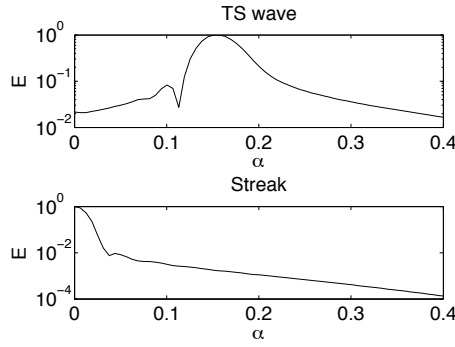


FIGURE 8. Energy spectra along the streamwise direction for the optimal initial condition at for that case $T = 1820$, $\beta = 0.05$ (TS-wave) and $T = 720$, $\beta = 0.55$ (Streak).

contribution to the trailing edge of the disturbance changes from streamwise vortices to streamwise streaks. The propagation velocity of the former is thus larger than that of the streaks as confirmed by a comparison between figure 7(a) and (b).

To further interpret the present results, we perform the Fourier transform along the streamwise direction of the two disturbances investigated above and compute the energy distribution in the various streamwise wave-numbers α (the energy density is first integrated in wall-normal and spanwise direction). The result shown in figure 8 demonstrates that the TS-wave disturbance has a peak at a relatively higher $\alpha \approx 0.17$, a value in agreement with predictions from local parallel stability calculations. The streak mode, conversely, has most of its energy at the lowest wave-numbers.

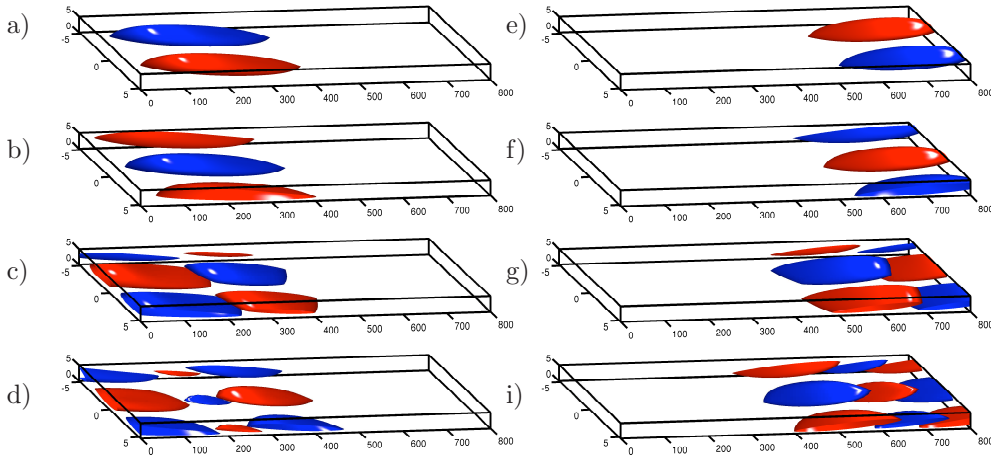


FIGURE 9. Wall-normal component of the leading four eigenvectors for the optimisation problem at $\beta = 0.55$, $t = 720$ and the corresponding responses. The structures are plotted over one wavelength in the spanwise direction. Red/blue colour indicate isosurfaces corresponding to positive/negative velocities at 10 percent of the maximum. a) The initial condition with largest growth. b) Flow structures corresponding to the second eigenvalue. This is similar to the first eigenvector, only shifted in the spanwise direction. The corresponding eigenvalue is the same. c) Third eigenvector associated to the same eigenvalue as the fourth eigenvector (not shown). d) Fifth eigenvector. In e), f), g) and i) the corresponding responses are shown, in particular the streamwise component. Note that the axes are not at the actual aspect ratio, the structures are elongated.

Four different optimal initial conditions for $\beta = 0.55$ and $T = 720$ are shown in figure (9). The wall-normal velocity component of the eigenvector leading to the maximum growth is reported in (9a). Since the base flow is uniform in the spanwise direction, the second eigenvector has the exact same shape as the first, only shifted half a wavelength in z as shown in figure (9b). These eigenvectors correspond to the same eigenvalue $\gamma_{1,2} = 2.6 \cdot 10^3$, and they may be combined linearly to obtain a disturbance located at any spanwise position. In figure 9c)-d) the third eigenvector associated with $\gamma_3 = 2.2 \cdot 10^3$ and the fifth associated with $\gamma_5 = 1.6 \cdot 10^3$ are shown respectively. Also these eigenvectors come in pairs with matching eigenvalues. It is thus possible with the Arnoldi method to obtain several optimals for a single parameter combination. This has not been done previously for the Blasius flow, while Blackburn *et al.* (2008) computed several optimals for the flow past a backward-facing step.

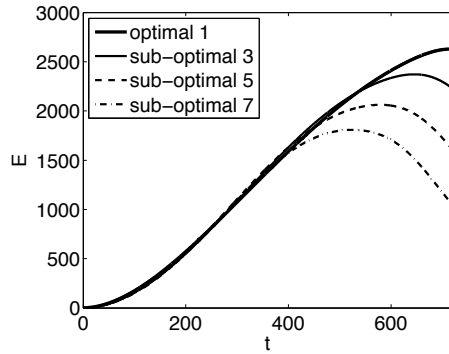


FIGURE 10. The evolution of the energy of the perturbation in time for each of the initial conditions in figure 9. The even-numbered sub-optimals give exactly the same evolution as their corresponding odd-numbered.

The responses to each of these initial conditions are shown in figures (9e-i). One can see that the sub-optimal initial conditions reproduce structures of shorter extension and with low- and high-speed streaks alternating in the streamwise direction. Figure (10) shows the energy evolution versus time for each of the sub-optimals. The energy growth is similar in the beginning, however later on, faster decay is observed with decreasing order of optimality. Optimal perturbations form an orthogonal basis; this fact may be exploited to project incoming disturbances and predict their evolution.

5.1.2. Localised optimal initial condition

In this section, we look into the general case of three-dimensional initial disturbances. Using the method described in section 3, along with the necessary modifications explained in appendix Appendix B, spatially localised optimal initial conditions are sought. A large domain is chosen to allow for a fully three-dimensional disturbance to propagate and expand in all directions without interacting with the boundaries. The spanwise width is chosen to be $Lz = 502.6$ (corresponding to the fundamental wave-number $\beta = 0.0125$) for the cases with longest optimisation time and $Lz = 251.3$ ($\beta = 0.025$) for the shorter optimisation times. Furthermore $n_z = 128$ Fourier modes were used in the spanwise direction, instead of 4 for the spanwise periodic cases. This increases the total number of degrees of freedom in our optimisation problem from approximately 1 to 30 millions.

The initial condition is placed near the inflow of the computational domain and power iterations are used to compute the optimal shape of the disturbance inside a fixed region. The area to which the initial condition is limited is $30\delta_0^*$ long and $40\delta_0^*$ wide and it is centered around the location $x = 25\delta_0^*$ and $z = 0$. Along the wall-normal direction the optimisation process restricts

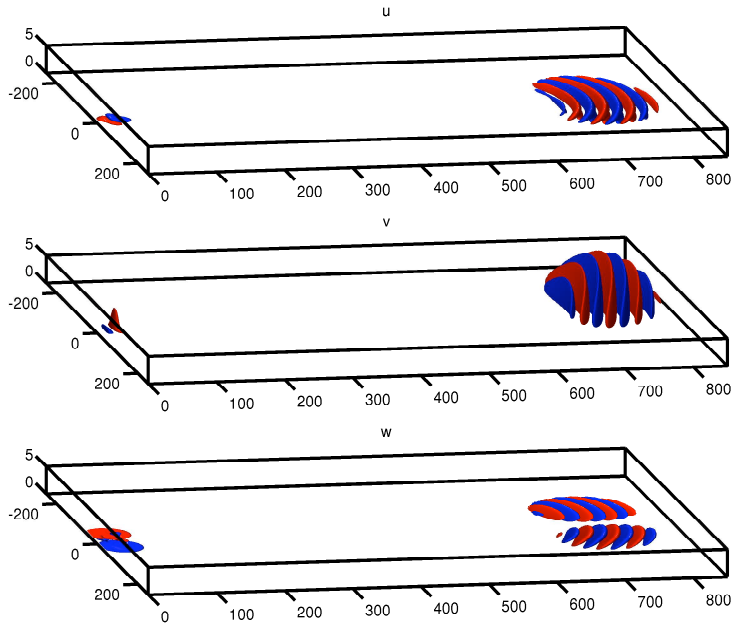


FIGURE 11. Optimal localised initial condition and corresponding response at time $T = 1820$, the optimal TS wave-packet. The amplitudes of each velocity component are reported in table 1.

the perturbation near the wall, inside the boundary layer, hence no additional localisation is adopted. The cases presented here correspond to the two physical mechanisms found to be relevant in the previous section, the Orr/TS-wave scenario and the lift-up process. To excite the two separately, the corresponding optimisation times are chosen to be $T = 1820$ and $T = 720$. In addition, one intermediate case, $T = 900$, where both these two mechanisms are active, is presented.

For the longest optimisation time considered, see figure 11, the TS-wave scenario is completely dominating the dynamics. The characteristic upstream tilted structures are present in the initial condition and all the velocity components achieve a significant growth. The wave-packet grows while travelling downstream and it consists of structures almost aligned in the spanwise direction, forming symmetric arches. The three-dimensional nature of this wave-packet is noticeable in the spanwise velocity component of the response, accounting for the spreading of the disturbance normal to the propagation direction and to the presence of unstable oblique waves. As in the case of the spanwise periodic disturbances, the total energy growth due to the streamwise normality (TS-waves for $T = 1820$) is about one of order magnitude larger than the amplification triggered by the lift-up effect at $T = 720$ (component-wise

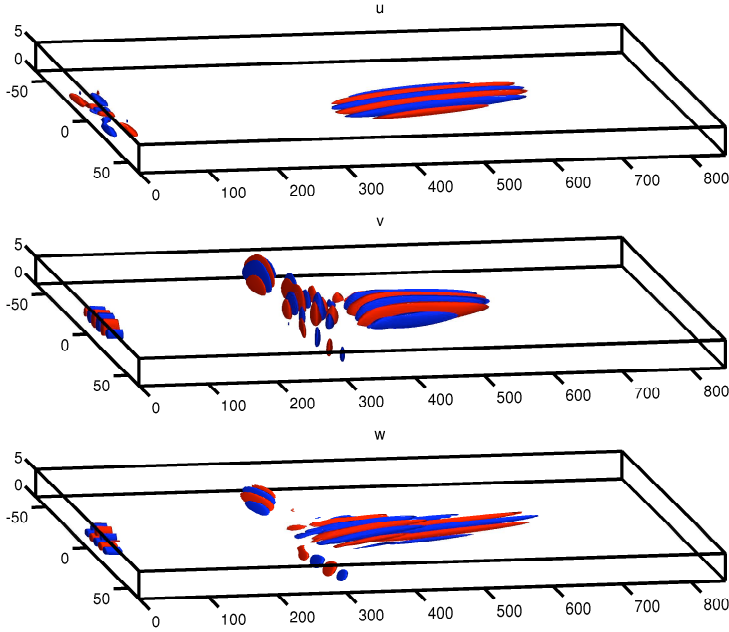


FIGURE 12. Optimal localised initial condition and corresponding response at time $T = 720$, the optimal streaky wavepacket. The amplitudes of each velocity component are reported in table 1.

Time	Comp.	Initial condition	Response	Total growth
720	u	0.00398	275.42913	275.76202
	v	0.36452	0.02334	
	w	0.63149	0.30954	
1820	u	0.74441	1012.39550	1763.75695
	v	0.00314	278.58122	
	w	0.25244	472.78022	

TABLE 1. Energy pertaining each component of the three-dimensional optimal initial condition and the corresponding response. The total energy amplification is reported in the last column. All the values are normalised with the total energy of the initial condition.

non-normality). Table 1 compiles the energy amplifications for the cases under investigation and reports the value of the energy content in each velocity component for the initial and final conditions.

The flow structures shown in figure 12, with corresponding amplitudes in table 1, document the optimal initial conditions for $T = 720$. The lift-up effect

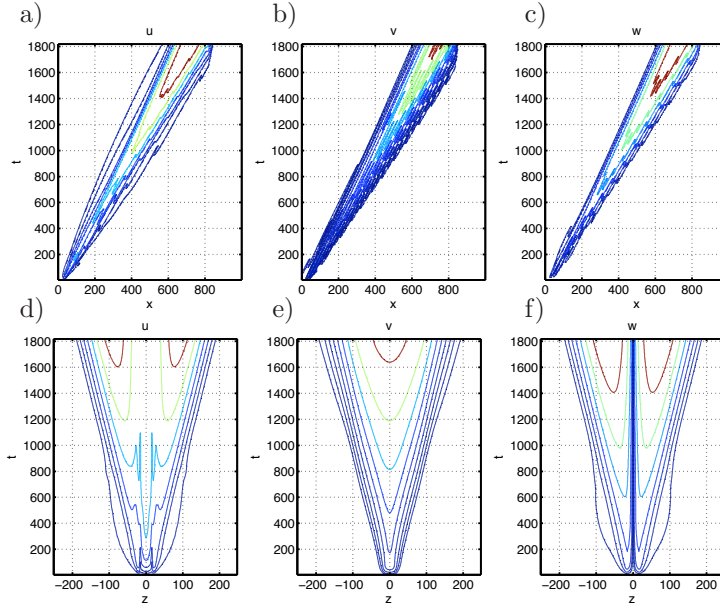


FIGURE 13. Space-time diagram of the energy of three velocity components of the perturbation for the optimal TS wavepacket (optimisation time $T = 1820$). Top line shows the spreading of the disturbance in the streamwise direction where the disturbance velocity is integrated in the spanwise and wall-normal direction: (a) streamwise, (b) wall-normal and (c) spanwise velocity component, respectively. (d), (e) and (f) show the evolution in the spanwise direction of the perturbations integrated in the streamwise and wall-normal direction. The propagation velocity of the leading edge of the disturbance is $c_{le} = 0.47$ while the trailing edge travels at $c_{te} = 0.32$. The spanwise spreading speed is $c_z = 0.084$.

with the formation of streamwise elongated streaks is evident in this case. The initial condition is characterised by strong streamwise vorticity, wall-normal and spanwise velocity components, while the response is predominantly in the streamwise velocity component. Interestingly, we note weak TS-waves propagating behind the streaks (visible in the wall-normal and spanwise velocity components). Since the optimisation time is short, TS-waves will not have the opportunity to grow and their contribution to the initial condition is therefore limited. However, this cannot be zero for a localised initial perturbation. Note further that the spanwise component is found to be weak and hence the spreading of the disturbance in this direction is limited.

The characteristics of the optimal wave-packets are analysed by the space-time diagrams in figure 13 and 14. Here, the propagation of the disturbance

in the streamwise direction is determined by considering the integral of the energy associated with each velocity component in the wall-normal and spanwise direction. Similarly, the lateral spreading is computed by integrating the perturbation velocities in the streamwise and wall-normal direction. Comparing the two cases we see that the TS wave-packet expands faster in the spanwise direction while travelling downstream more slowly than the optimal streaky wave-packet. The propagation velocity of the leading edge of the TS-like disturbance is $c_{le} = 0.47$ while the trailing edge travels at $c_{te} = 0.32$. The spanwise spreading speed is $c_z = 0.084$, corresponding to an angle of $\theta = 11.46^\circ$. These values can be compared to those observed experimentally by Gaster (1975); Gaster & Grant (1975) and to the theoretical analysis in Koch (2002). The latter author determined the propagation speed of the leading edge of a localised wave-packet to be 0.5 and the trailing edge velocity to be 0.36 by computing the group velocity of three-dimensional neutral waves. The largest spanwise group velocity was found to be approximately 0.085, a value very close to those reported here. The agreement is remarkable even though the results in Koch (2002) are obtained at a lower Reynolds number, i.e. $Re = 580$.

The difference between leading and trailing edge of the optimal streaky wave-packet, $c_{le} = 0.90$ and $c_{te} = 0.36$, explains the larger extension of the latter; while the front travels at the speeds typical of the upper part of the boundary layer where the streaks are located, the trailing edge velocity is that of the unstable waves seen on the rear. The spanwise spreading speed is $c_z = 0.0098$, corresponding to an angle of $\theta = 0.89^\circ$. It should be mentioned that this spreading rate pertains the energetically dominant velocity component, i.e. the streamwise component. The slow lateral diffusion is most likely only due to the effect of viscosity; the growing streaky structures are therefore characterised by zero spanwise propagation velocity.

Figure 14b) and c) clearly demonstrates the short and slower packet of waves following the main streaky structures. As mentioned above, the spanwise propagation of the streamwise vortices and streaks is limited; conversely, the sequence of waves on the rear part of the wave-packet has a spanwise spreading rate comparable to that of the TS wave packet, in particular the value $c_z = 0.073$ is obtained by considering the energy of the spanwise velocity component.

Finally, we computed optimal disturbances for intermediate optimisation times and the amplifications were generally lower than in the two previous cases. However it was interesting to notice that for times around 800 to 900 perturbations containing both streaky and wavy structures emerge. The spectrum of the initial conditions is composed by a broad range of disturbances. Interestingly, the flow response is again characterised by short-wavelength instability waves following elongated streaks, apparent only in the streamwise velocity component. The TS wave-packet becomes more and more relevant as the optimisation time increases.

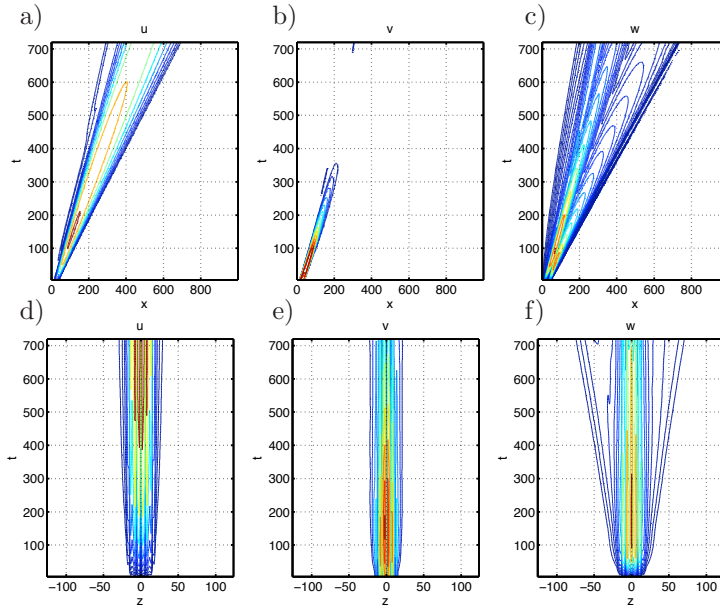


FIGURE 14. Space-time diagram of the energy of three velocity components of the perturbation for the optimal streaky wave-packet (optimisation time $T = 720$). Top line shows the propagation of the disturbance in the streamwise direction where the disturbance velocity is integrated in the spanwise and wall-normal direction: (a) streamwise, (b) wall-normal and (c) spanwise velocity component, respectively. (d), (e) and (f) show the evolution in the spanwise direction of the perturbations integrated in the streamwise and wall-normal direction. The propagation velocity of the leading edge of the disturbance is $c_{le} = 0.90$ while the trailing edge travels at $c_{te} = 0.36$. The spanwise spreading speed is $c_z = 0.0098$ (based on the u -component).

5.2. Optimal forcing

5.2.1. Global forcing

Since boundary layers are convectively unstable, thereby acting as noise amplifiers, a prominent role is played by the response to forcing, rather than by the detailed time-evolution of the initial condition; The optimal forcing is therefore a relevant measure of the maximum possible growth that may be observed in the computational domain. Analysis of the frequency response can also have implications for control revealing the forcing location and frequencies the flow is most sensitive to. While the evolution of the optimal initial condition consists of the propagation and amplification of a wave packet, eventually leaving the

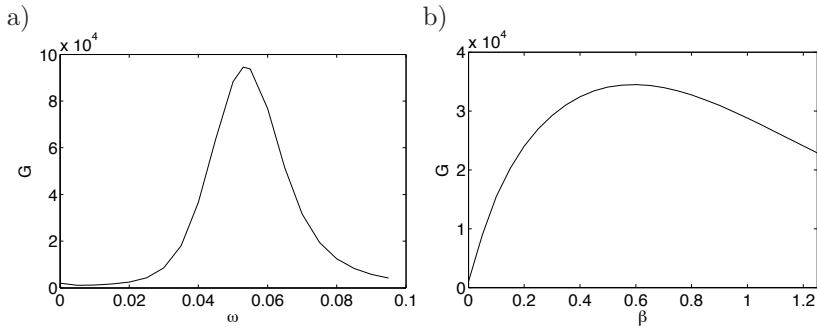


FIGURE 15. a) Frequency response for zero spanwise wavenumber *i.e.* two-dimensional disturbances. The optimal response is obtained for the frequency $\omega = 0.055$. b) Response to zero frequency forcing $\omega = 0$ for different spanwise wavenumbers. The maximum response is obtained at $\beta = 0.6$

computational box (or measurement section), the response of the flow to periodic forcing will consist of structures with a fixed amplitude at each streamwise station, oscillating around the mean flow. We investigate the structure of the optimal forcing and the corresponding response for a range of spanwise wavenumbers and frequencies. Thus, for each wave number we examine a number of temporal frequencies. Ideally we would like to solve the linearized Navier–Stokes equations for very large times, ensuring that we are only considering the regime (long-time) response at the specific frequency under investigation. In practice however we are restricted to a finite final time by the computational cost of solving the direct and adjoint equations involved in the iteration scheme. Using power iterations to find the largest eigenpair typically requires from approximately 15 iterations to about 100 for the most stable frequencies; in other words we need to integrate the governing equations at least 30 times. As can be deduced from the results in the previous section transiently growing perturbations of small spanwise scale leave our domain at time $t \approx 2000$, while locally unstable TS-waves propagates at a speed of about $0.3 U_\infty$. This observation, along with several convergence tests using different integration intervals to extract the flow regime response lead to the conclusion that integration to $T = 5000$ is long enough to observe the pure frequency response.

Figure 15 shows the square of the resolvent norm, *i.e.* the response to forcing for the two limiting cases $\beta = 0$ and $\omega = 0$. In figure 15a) the response to two-dimensional forcing, inducing perturbations with $\beta = 0$, is displayed. The maximum response is observed for the frequency $\omega = 0.055$. This maximum is obtained at the frequency where the least stable TS eigenvalue is located (see Bagheri *et al.* 2009a). Indeed it is known that by projecting the dynamics of the flow onto the basis of eigenmodes, the response to forcing is given by the combination of resonant effects (distance in the complex plane from forcing frequency to eigenvalue) and non-modal effects, *i.e.* the cooperating

non-orthogonal eigenvectors (Schmid & Henningson 2001). In Åkervik *et al.* (2008) it was shown for a similar flow that non-normal eigenvectors could induce a response about twenty times larger than that induced only by resonant effects.

The response to zero temporal frequency for different spanwise wave-numbers β is shown in figure 15b), where according to local theory the maximum response is expected for spanwise periodic excitations. The maximum growth may be observed for the wave-number $\beta = 0.6$, a slightly larger value than for the optimal initial condition case. Notice that in the case of optimal forcing there is a smaller difference in the maximum gain between the two different dominating mechanisms (TS-waves vs. streaks).

A full parameter study has been carried out in the frequency–spanwise wave-number (ω, β) plane. A contour map showing the regime response to optimal forcing is displayed in figure 16. As in the case of the optimal initial condition, the global maximum response to forcing is observed for $\beta = 0.05$. It reaches this maximum for the frequency $\omega = 0.055$. A second region of strong amplification is found for low frequencies and high spanwise wave-numbers. Here the most amplified structures consist of streamwise elongated streaks induced by cross-stream forcing. At the largest spanwise wave-numbers, we also observe that the decay of the amplification when increasing the forcing frequencies is rather slow. Conversely, the peak corresponding to excitation of the TS-waves is more pronounced.

A visualisation of the overall maximum amplification, found for the spanwise wave-number of $\beta = 0.05$ and for the same frequency $\omega = 0.55$ yielding the optimal two-dimensional forcing, is presented next. The optimal forcing in the streamwise momentum equation and the streamwise velocity component of the optimal response are shown in figure 17. The optimal forcing structures are leaning against the shear (see 17a) to optimally trigger the Orr mechanism; the regime long-time response of the flow, shown in figure 17b), reveals the appearance of amplified TS-waves at the downstream end of the computational domain.

The optimal forcing structure at $\beta = 0.6$ and the zero frequency has almost all its energy in the spanwise and wall normal components, that is the flow is forced optimally in the wall-normal and spanwise direction as shown among others by Jovanovic & Bamieh (2005) for channel flows. The wall-normal and spanwise components of the forcing are displayed in figure 18a) and b). The rms values of the streamwise component of the forcing is only two percent of that pertaining to its spanwise and wall-normal counterparts. The lift-up effect transfers momentum into the streamwise component (shown in figure 18c), which contains 99.99 percent of the energy of the flow response. The streak amplitude increases in the streamwise direction until the fringe region is encountered.

The Fourier transform along the streamwise direction of the two disturbances investigated above is shown in figure 19. As in the case of the optimal initial

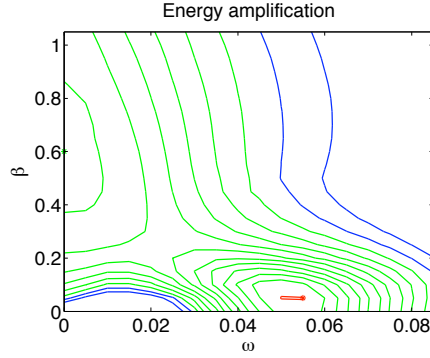


FIGURE 16. Contour map of response to forcing with frequency ω versus spanwise wave-number β . The contour levels span three orders of magnitude and thus we use a logarithmic scale. The blue lines are of order $10^3 - 10^4$, the green $10^4 - 10^5$ and the red $10^5 - 10^6$. For each level we define 10 contour lines but only levels present in the actual data are visible. The maximum response to forcing is observed for $\beta = 0.05$ and for the frequency $\omega = 0.055$. The amplification factor is $G = 1.01 \cdot 10^5$. The maximum growth due to the streak mechanism is found for the spanwise wave-number $\beta = 0.6$ at $\omega = 0$ where the amplification factor is $G = 3.45 \cdot 10^4$.

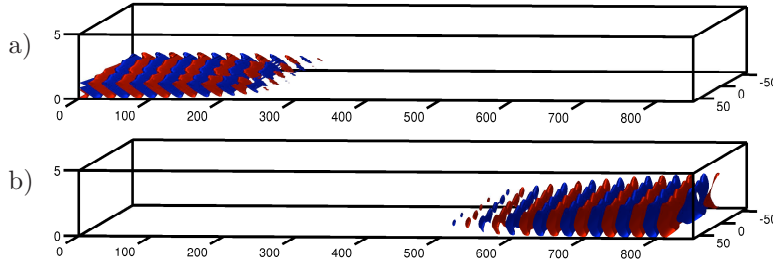


FIGURE 17. Isosurfaces of optimal forcing and response for the streamwise wave-number $\beta = 0.05$ subject to forcing at the frequency $\omega = 0.055$. Red/blue colour signifies isosurfaces corresponding to positive/negative velocities at 10 percent of the maximum. a) Streamwise component of optimal forcing structure. b) Streamwise velocity component of the response.

conditions in figure 8, the energy density is first integrated in wall-normal and spanwise direction. The results indicate that the TS-wave disturbance has a peak at a relatively high $\alpha \approx 0.17$ while the zero-frequency forcing is concentrated at the lowest wave-numbers. The peak at the wave-number of the most

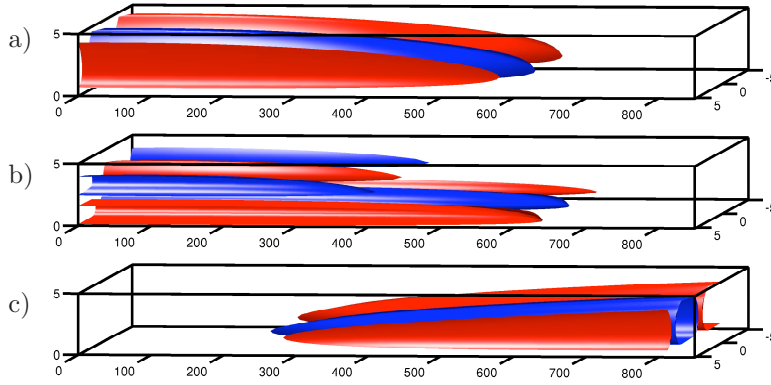


FIGURE 18. Isosurfaces of optimal forcing and response for the streamwise wave-number $\beta = 0.6$ subject to steady forcing. Red/blue colour indicates isosurfaces corresponding to positive/negative velocities at 10 percent of the maximum. a) Wall-normal component of optimal forcing structure. b) Spanwise component of optimal forcing. c) Streamwise velocity component of the flow response. Both the forcing structures and the response are elongated in the streamwise direction.

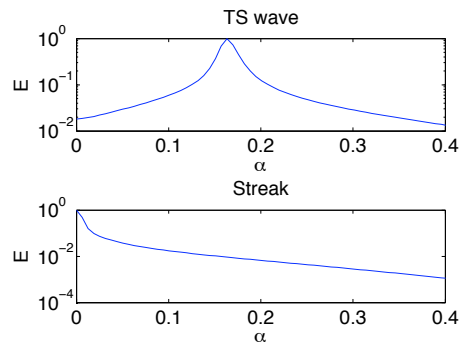


FIGURE 19. Energy spectra along the streamwise direction for the optimal forcing at for that case $\omega = 0.055$, $\beta = 0.05$ (TS-wave) and $\omega = 0$, $\beta = 0.6$ (Streak).

unstable TS-waves is more evident in the case of forcing than in the case of the optimal initial condition (cf. figure 8).

5.2.2. Localised forcing

In this section we present results obtained by restricting the forcing to a small region near the inflow of the computational domain. The formulation presented

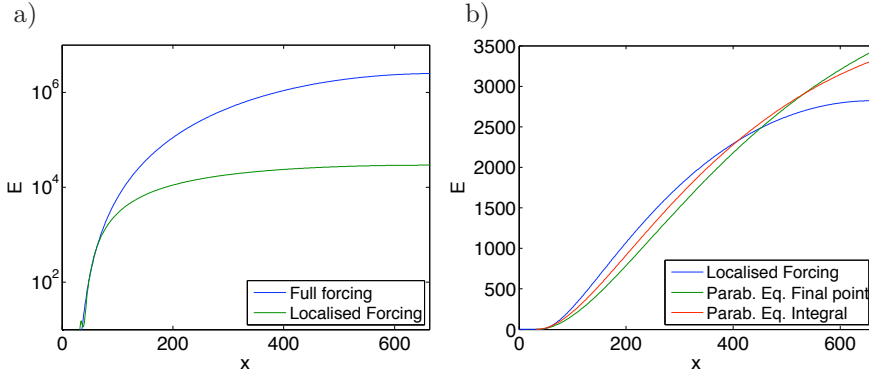


FIGURE 20. Downstream evolution of the kinetic energy of the flow integrated over cross-stream planes. In a) blue and green lines are used to indicate the response to steady forcing active everywhere in the domain (“Full forcing”) and in a short region near the inflow (“Localised forcing”) respectively. The data are scaled with the magnitude of the forcing computed as integral over the whole domain. In b) the blue line corresponds to the case of localised forcing in a) while green (“Parab. Eq. Final Point”) indicates the evolution of the optimal initial condition yielding the largest possible kinetic energy at the downstream location $662\delta_0^*$ (Levin & Henningson 2003), and the red line (“Parab. Eq. Integral”) the evolution of optimal initial condition yielding the largest integral over the streamwise domain. In order to make a physically relevant comparison we have scaled the data pertaining to the “Localised Forcing” with the value of the response just downstream of the forcing region. The centre of the forcing is at the location $x = 32.3\delta_0^*$ corresponding to the optimal upstream location in Levin & Henningson (2003).

in section 4 is altered by multiplying the forcing \mathbf{f} with a function $\lambda(x)$ which is non zero only in a short streamwise region. The edges of this region are defined by two smooth step functions rising from zero to one over a distance of about $1\delta_0^*$. The centre of the forcing is chosen to be at $x = 23\delta_0^*$ with width of $4\delta_0^*$ if not otherwise stated.

This problem is physically closer to the case when disturbances are generated upstream, closer to the leading edge, and their evolution is monitored as they are convected downstream. Initially a comparison with optimal upstream disturbances calculated by means of the parabolized equations is thus presented (see results in Levin & Henningson 2003).

To this aim, we compute the optimal localised steady forcing for spanwise wave-number $\beta = 0.53$ at $x = 32.3\delta_0^*$. These were found to be optimal location and spanwise scale of the overall optimal in Levin & Henningson (2003); in their

scalings they correspond to $X = 0.37$ and $\beta = 0.53$ for an initial perturbation downstream of the leading edge with Reynolds-number independent evolution, here assumed to be $Re_x = 10^6$.

In figure 20 the streamwise growth of the energy of the perturbation obtained with four different approaches is shown. In figure 20a we compare the flow regime response to steady forcing active everywhere in the domain with the response to forcing localised upstream. Further, the latter is compared in figure 20b with the evolution of the optimal initial conditions yielding the largest possible kinetic energy at the downstream location $662\delta_0^*$ and with the evolution of the optimal upstream velocity profile yielding the largest integral of the perturbation energy over the whole streamwise domain (see also Cathalifaud & Luchini 2000). The two latter are computed with the parabolic stability equations (David Tempelmann, private communication); the case having as objective function the integral of the perturbation energy is indeed more relevant to comparing with the present results. It can be seen that the growth is faster when the forcing is active everywhere in our control domain since the component-wise transfer of energy is at work at every streamwise position. The two curves obtained with the parabolic equations (fig. 20a) are similar: faster growth is observed when the control is optimising over the whole domain, while a larger final level is reached when the objective is limited to the last downstream station. The comparison between the response to “localised forcing” and the “parabolic equations” cases reveals good agreement. The main differences between the two methods are the different set of equations and the way the disturbance is introduced. In Levin & Henningson (2003) and Cathalifaud & Luchini (2000) the linearised boundary-layer equations are used, whereas we optimise solving the linearised Navier–Stokes equations. In addition, an optimal upstream boundary condition is computed in Levin & Henningson (2003), whereas an optimal forcing is sought here.

Figure 21a) displays the structure of the optimal forcing function for the case of localised excitation. The wall-normal profiles shown in the plot are obtained by integrating the forcing in the streamwise direction. Figure 21b) and c) depict instead the optimal initial condition obtained with the parabolic boundary-layer equations, i.e. a streamwise vortex pair. The structure of the disturbances are remarkably similar; in the case of the optimal forcing (figure 21a), the action is located closer to the wall with a relatively weaker wall-normal component. When comparing the cases in b) and c) one can note that the vortices leading to the largest possible energy downstream are located further up into the free-stream. Conversely, when the perturbations is required to grow over the whole domain, the disturbance needs to be located in the shear layer so that its effect can be readily felt (cf. figure 21a and c). The results in the figure indicate that forcing the momentum equation is less effective in the free stream: optimal forcing thus induces streaks which grow for a shorter downstream distance.

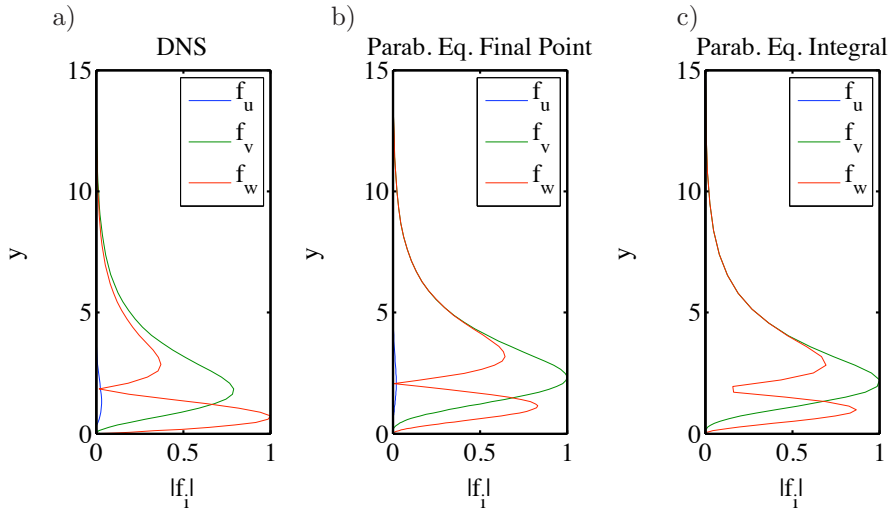


FIGURE 21. Wall-normal profiles of the streamwise, spanwise and wall-normal components of a) the optimal localised forcing (integrated in the streamwise direction), b) the initial condition yielding the largest possible kinetic energy at the downstream location $662\delta_0^*$; c) the initial condition yielding the largest integral of the disturbance energy over the streamwise domain.

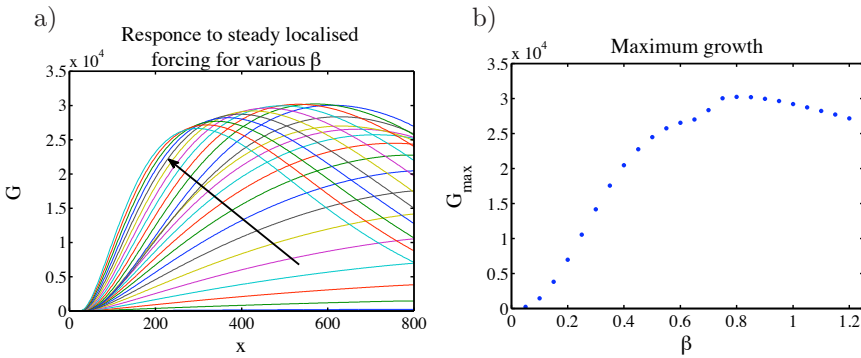


FIGURE 22. a) Streamwise evolution of the response to steady localised forcing for different spanwise wave-numbers β . The arrow indicates increasing β . b) Maximum response versus spanwise wave-numbers.

A parameter study is conducted to examine the effect of frequency and spanwise scale of the localised forcing. First, figure 22, the results obtained when varying the spanwise wave-number are shown. The downstream evolution originating from optimal localised disturbances of zero frequency are

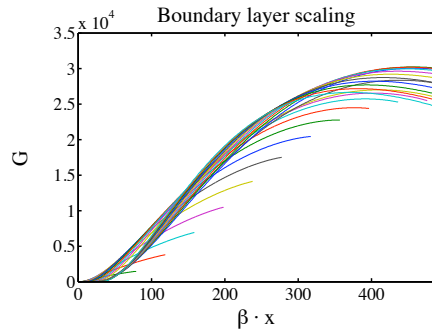


FIGURE 23. Streamwise evolution of the response to localised forcing for different spanwise wave-numbers β where the streamwise position x is scaled with β . The distance from the leading edge is considered to re-scale the data.

displayed for the spanwise wave-numbers investigated. A slower energy growth is observed for the lower wave-numbers owing to the lower forcing to the streaks (proportional to β); the wave-number giving the largest peak response for the present configuration is $\beta = 0.8$. Forcing of smaller scale induce streaks rapidly, but viscous dissipation causes earlier decay.

As shown among others by Andersson *et al.* (2001), in the limit of validity of the boundary layer equations there is a coupling between the streamwise and spanwise length scale of the disturbance. It is in fact possible to show that a streak family $u(x, y, z)$, defined by the spanwise wave-number β_0 , is independent of the Reynolds number. This results in a scaling property that couples the streamwise and spanwise scales, implying that the same solution is valid for every combination of the streamwise location $x + x_0$ (distance from the leading edge) and of β such that their product stays constant. In other words, this amounts to moving along the plate and varying the spanwise wave-number so that the local spanwise wave-number $\beta_0 \delta^* / \delta_0^*$ remains constant (see also Brandt *et al.* 2003). To further examine this scaling property, the streamwise coordinate in figure 22a) is multiplied by the spanwise wave-number of the disturbance and the result shown in figure 23. Despite the fact that the streamwise extent of each curve is different, the curves indicating the evolution of the streaky disturbance collapse notably, thus confirming the similarity of the boundary-layer streaks.

Finally we investigate the case of zero spanwise number (pure two-dimensional disturbances) and vary the temporal frequency. The results are shown in figure 24. The growth observed here is due to the combined Orr and TS-wave mechanism and thus the value of the optimal frequency is close to that obtained when forcing over the whole domain, $\omega = 0.055$. The structure of the optimal forcing for the frequency with largest amplification is displayed in figure 25. The excitation is localised closer to the wall, well inside the boundary

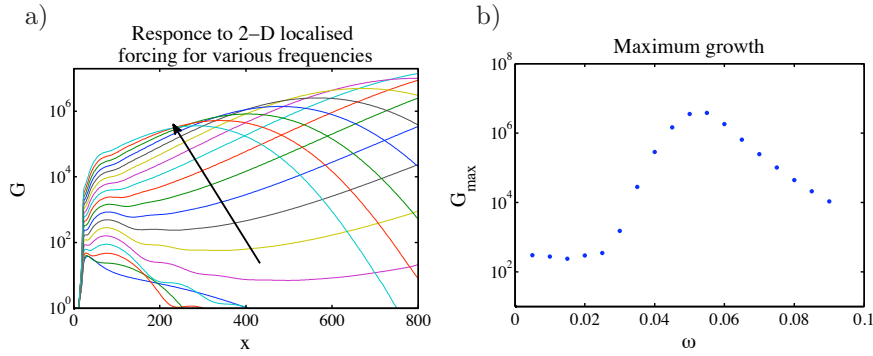


FIGURE 24. a) Streamwise evolution of the response to localised forcing for different temporal frequencies ω . The arrow indicates increasing ω . b) Maximum growth with respect to ω .

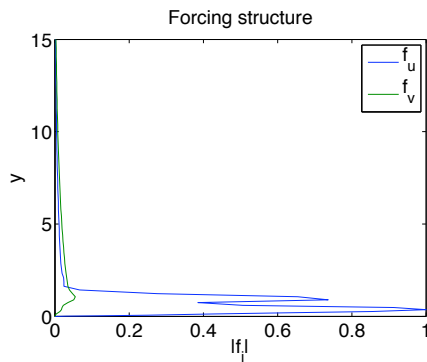


FIGURE 25. Localised forcing with frequency. We plot the streamwise and wall-normal components of the forcing function. The quantities are integrated in the streamwise direction. Note that this is a 2D structure thus the spanwise component is zero.

layer, when compared to the forcing forming streamwise streaks, see figure 21. Forcing the streamwise momentum equation is significantly more efficient at triggering the Orr mechanism and the following wave packet of two-dimensional TS waves.

6. Conclusions

We have used a Lagrange multiplier technique in conjunction with direct and adjoint linearized Navier–Stokes equations in order to quantify the growth potential in the spatially developing flat-plate boundary-layer flow at moderately high Reynolds. Spanwise periodic and fully three-dimensional disturbances are

investigated. We consider both the initial conditions leading to the largest possible energy amplification at time T and the optimal spatial structure of time-periodic forcing. To the best of our knowledge, the pseudo-spectrum of the governing operator along real frequencies is computed here for the first time with matrix-free methods. The optimisation framework adopted does not restrict us to assume slow variation of the base flow in the streamwise direction, common to both the first order approximation of the OSS formulation and the more advanced PSE approximation. Specifically we do not, as in the PSE framework, need different equations to describe the lift-up instability and the wave packet propagation.

For the optimal initial condition we find that the largest potential for growth is found at small spanwise wave-numbers and consists of upstream tilted structures, enabling the subsequent disturbances to exploit the Orr mechanism and the local convective instability of the oblique wave packet of Tollmien-Schlichting waves. The length and position of the initial disturbance is related to the final time of the optimisation: short time evolution requires the wave-packet to be initiated further downstream in the region of largest local instability and vice-versa for longer optimisation times. The lift-up instability mechanism inherent to spanwise wavelengths of the order of the boundary layer thickness is faster than the Orr/oblique instability; we show that for the present configuration the latter instability needs approximately 300 time units more to extract as much energy as the lift-up instability. The results indicate that streamwise vortices of finite length become optimal once a spatially-evolving boundary layer with inflow/outflow conditions is considered. As concerns the optimal response to periodic forcing, the difference in the two instabilities is less pronounced. In this case, the Orr/oblique wave instability only manages to gain a factor of two in energy more than the streak mechanism. The largest amplification of the local convective instability over the non-modal streak generation can be explained by the long computational box examined and the relatively high inflow Reynolds number. Starting closer to the leading edge, one can expect streaks to dominate the transition scenario.

Three-dimensional localised optimal initial conditions are also computed and the corresponding wave-packets examined. For short optimisation times, the optimal disturbances consist of streaky structures propagating and elongating in the downstream without any significant spreading in the lateral direction. For long optimisation times, conversely, the optimal disturbances are characterised by wave-packets of TS-waves. These travel at lower streamwise speed and with faster spreading in the spanwise direction. The latter can achieve the largest possible energy amplification. Intermediate optimisation times are also considered where both the TS- and streak-mechanism are relevant. The wave-packet has therefore features from both scenarios previously considered: It consists of elongated streaks in the streamwise velocity component, followed by short-wavelength instability waves, mainly evident in the cross-stream velocities.

Finally, we examine the effect of inflow upstream disturbances on the the boundary layer flow. Thus we introduce a localised forcing near the inflow of the computational box and compute the forcing structure that provides the largest response over our control domain. First, we compare with results based on the solution of the parabolized Navier-Stokes equations: good agreement is obtained, despite the differences of the two methods. Secondly, we investigate zero-frequency upstream forcing and show a maximum for perturbations with spanwise wave-number larger than that obtained when the forcing location is not constrained. Thirdly, analysis of time-periodic two-dimensional forcing is considered: the findings agree with those obtained with distributed forcing since the flow response corresponds in both cases to exponentially growing Tollmien-Schlichting waves at the forcing frequency.

Three different destabilising mechanisms are considered in this study, all at work in the boundary layer flow. Although these could be explained using the OSS equations, they are analysed without any simplifying assumptions. The present work is of a more general character. By choosing an objective function and using the full linearized Navier–Stokes equations as constraints we are not limiting ourselves to simple geometries. Whenever a DNS code is available to accurately describe a flow, all that is needed in order to investigate the stability characteristics is a linearised version of the code and the implementation of the corresponding adjoint equations along with a wrapper built around these two simulations ensuring the correct optimisation scheme. The method used here is therefore applicable to any geometrical configuration.

Acknowledgements

The authors wish to thank David Tempelmann for providing data from the parabolic stability equations and for many fruitful discussions. Inspiring comments on the manuscript from Carlo Cossu are acknowledged as well. Computer time was provided by the Centre for Parallel Computing (PDC) at KTH, Stockholm. The present work is supported by the Swedish research council which is gratefully acknowledged.

Appendix A. Derivation of the adjoint equations

In this section we report the derivation of the adjoint linearised Navier–Stokes equations, needed to perform directional derivatives on the augmented cost functions (17) and (29). The definition of the adjoint evolution operator is associated with the inner product $(\mathbf{u}, \mathbf{u}) = \int_{\Omega} \mathbf{u}^T \mathbf{u} \, d\Omega$,

$$(\mathbf{p}, \exp(\mathcal{A}t)\mathbf{u}) = (\exp(\mathcal{A}^\dagger t)\mathbf{p}, \mathbf{u}). \quad (42)$$

The inner product in time-space domain $\Sigma = [0, T] \times \Omega$ is used in the derivation of \mathcal{A}^\dagger ,

$$(\mathbf{u}, \mathbf{u})_{\Sigma} = \int_0^T (\mathbf{u}, \mathbf{u}) \, dt = \int_0^T \int_{\Omega} \mathbf{u}^T \mathbf{u} \, d\Omega \, dt. \quad (43)$$

By noting that the linearised Navier–Stokes equations can be written as $(\partial_t - \mathcal{A})\mathbf{u} = 0$ we recognise that the adjoint should satisfy the following property

$$(\mathbf{p}, (\partial_t - \mathcal{A})\mathbf{u})_\Sigma = ((-\partial_t - \mathcal{A}^\dagger)\mathbf{p}, \mathbf{u})_\Sigma = 0. \quad (44)$$

In order to derive the exact structure of the operator \mathcal{A}^\dagger we adopt the formulation including the pressure

$$\partial_t \mathbf{u} + (\mathbf{U} \cdot \nabla)\mathbf{u} + (\mathbf{u}\nabla)\mathbf{U} - Re^{-1}\Delta\mathbf{u} + \nabla\pi = 0 \quad (45)$$

along with continuity,

$$\nabla\mathbf{u} = 0. \quad (46)$$

In this form, the Lagrange function consists of two governing equations with multipliers \mathbf{p} and σ

$$\int_\Omega [(\mathbf{p})^T (\partial_t \mathbf{u} + (\mathbf{U} \cdot \nabla)\mathbf{u} + (\nabla\mathbf{U})\mathbf{u} - Re^{-1}\Delta\mathbf{u} + \nabla\pi) + (\sigma, \nabla\mathbf{u})] \, d\Omega \, dt \quad (47)$$

Integration by parts of the above expression yields

$$\begin{aligned} & \int_0^T \int_\Omega [(\mathbf{p})^T (\partial_t \mathbf{u} + (\mathbf{U} \cdot \nabla)\mathbf{u} + (\nabla\mathbf{U})\mathbf{u} - Re^{-1}\Delta\mathbf{u} + \nabla\pi) + (\sigma, \nabla\mathbf{u})] \, d\Omega \, dt \\ &= \int_0^T \int_\Omega \mathbf{u}^T (-\partial_t \mathbf{p} - (\mathbf{U} \cdot \nabla)\mathbf{p} + (\nabla\mathbf{U})^T \mathbf{p} - Re^{-1}\Delta\mathbf{p} - \nabla\sigma) \, d\Omega \, dt \\ &+ \int_0^T \text{B.C.} \, dt + \int_\Omega (\mathbf{p}(T))^T \mathbf{u}(T) \, d\Omega - \int_\Omega (\mathbf{p}(0))^T \mathbf{u}(0) \, d\Omega \\ &= ((-\partial_t - \mathcal{A}^\dagger)\mathbf{p}, \mathbf{u})_\Sigma + \int_0^T \text{B.C.} \, dt + (\mathbf{p}(T), \mathbf{u}(T)) - (\mathbf{p}(0), \mathbf{u}(0)). \end{aligned} \quad (48)$$

This equality defines the adjoint linearized Navier–Stokes equations

$$-\partial_t \mathbf{p} = \mathcal{A}^\dagger \mathbf{p} = (\mathbf{U} \cdot \nabla)\mathbf{p} - (\nabla\mathbf{U})^T \mathbf{p} + Re^{-1}\Delta\mathbf{p} + \nabla\sigma, \quad \mathbf{p}(T) = \mathbf{p}_T, \quad (49)$$

where σ is the adjoint pressure. It can also be expressed as solution to a Poisson equation

$$\Delta\sigma = -\nabla \cdot ((\mathbf{U} \cdot \nabla)\mathbf{p} - (\nabla\mathbf{U})^T \mathbf{p}), \quad (50)$$

with solution $\sigma = \mathcal{Z}\mathbf{p}$. The boundary conditions of the adjoint system are determined so that the integral containing boundary terms vanish. The adjoint field has periodic boundary conditions along the two wall parallel directions and homogeneous Dirichlet conditions at the wall and the free stream. The initial and end time inner products equals, *i.e.*

$$(\mathbf{p}(T), \mathbf{u}(T)) = (\mathbf{p}(T), \exp(\mathcal{A}T)\mathbf{u}(0)) = (\exp(\mathcal{A}^\dagger T)\mathbf{p}(T), \mathbf{u}(0)) = (\mathbf{p}(0), \mathbf{u}(0)). \quad (51)$$

Hence the adjoint evolution operator becomes

$$\mathbf{p}(0) = \exp(\mathcal{A}^\dagger T)\mathbf{p}(T), \quad (52)$$

solves the adjoint linearized Navier–Stokes equations backwards in time to fulfil the relation (44).

Appendix B. Localised initial condition

In this section we consider a localised initial condition and show how the Lagrangian approach is modified. Assuming the initial condition to be non-zero within a fixed region in space, e.g. $\mathbf{u}(0) \neq 0$ in $\Lambda \subset \Omega$, the relevant integral becomes

$$(\mathbf{u}(0), \mathbf{u}(0))_\Lambda = \int_\Lambda \mathbf{u}(0)^T \mathbf{u}(0) \, d\Lambda. \quad (53)$$

After the localisation is applied, the state variable might not satisfy the divergence-free condition, thus we need to re-enforce it by adding one more constraint in the Lagrange function. Therefore we rewrite equation (17) as

$$\begin{aligned} \mathcal{L}(\mathbf{u}, \mathbf{p}, \gamma) &= (\mathbf{u}(T), \mathbf{u}(T)) - \int_0^T (\mathbf{p}, (\partial_t - \mathcal{A}) \mathbf{u}) \, d\tau \\ &\quad - \gamma ((\mathbf{u}(0), \mathbf{u}(0))_\Lambda - 1) - (\psi, \nabla \cdot \mathbf{u}(0))_\Lambda \end{aligned} \quad (54)$$

where ψ is a new Lagrange multiplier. Compared to the derivation in section (3), the difference occurs when the variation with respect to the state variable is taken. Integration by parts of equation (54) yields

$$\begin{aligned} \mathcal{L} &= (\mathbf{u}(T), \mathbf{u}(T)) - \int_0^T (\mathbf{u}, (-\partial_t - \mathcal{A}^\dagger) \mathbf{p}) \, d\tau \\ &\quad - (\mathbf{p}(T), \mathbf{u}(T)) + (\mathbf{p}(0), \mathbf{u}(0)) - \gamma ((\mathbf{u}(0), \mathbf{u}(0))_\Lambda - 1) - (\psi, \nabla \cdot \mathbf{u}(0))_\Lambda \end{aligned} \quad (55)$$

The adjoint governing equation as well as the final-time condition are the same, $(-\partial_t - \mathcal{A}^\dagger) \mathbf{p} = 0$ and $\mathbf{p}(T) = \mathbf{u}(T)$, whereas variations with respect to the initial velocity field give the following condition

$$(\delta \mathbf{u}(0), \mathbf{p}(0)) - \gamma (\delta \mathbf{u}(0), \mathbf{u}(0))_\Lambda - (\delta \mathbf{u}(0), \nabla \psi)_\Lambda = 0. \quad (56)$$

The expression above can be re-written in integral form

$$\int_\Omega (\delta \mathbf{u}(0)^T \mathbf{p}(0)) - \gamma \int_\Lambda (\delta \mathbf{u}(0)^T \mathbf{u}(0)) - \int_\Lambda (\delta \mathbf{u}(0)^T \nabla \psi) = 0, \quad (57)$$

or

$$\int_{\Omega - \Lambda} (\delta \mathbf{u}(0)^T \mathbf{p}(0)) + \int_\Lambda \delta \mathbf{u}(0)^T (\mathbf{p}(0) - \gamma \mathbf{u}(0) - \nabla \psi) = 0. \quad (58)$$

The first integral is zero for $\delta \mathbf{u}(0) = 0$, which implies that the initial condition is not updated outside Λ . Therefore the new guess for the localised initial condition $\mathbf{u}(0)$ is

$$\mathbf{u}(0) = \gamma^{-1} (\mathbf{p}(0) - \nabla \psi)|_\Lambda. \quad (59)$$

In the above, the scalar field ψ is obtained by combining (59) with

$$\frac{\partial \mathcal{L}}{\partial \psi} = \nabla \cdot \mathbf{u}(0) = 0. \quad (60)$$

This gives a projection to a divergence free space where the pressure-like scalar field is solution of a Poisson equation.

It can be proven that this is a unique projection. In our numerical implementation the projection is actually performed by transforming in the velocity-vorticity formulation adopted for the computations (Chevalier *et al.* 2007).

References

- ÅKERVIK, E., EHRENSTEIN, U., GALLAIRE, F. & HENNINGSON, D. S. 2008 Global two-dimensional stability measures of the flat plate boundary-layer flow. *Eur. J. Mech. B/Fluids* **27**, 501–513.
- ÅKERVIK, E., HEPFFNER, J., EHRENSTEIN, U. & HENNINGSON, D. S. 2007 Optimal growth, model reduction and control in a separated boundary-layer flow using global eigenmodes. *J. Fluid Mech.* **579**, 305–314.
- ANDERSSON, P., BERGGREN, M. & HENNINGSON, D. S. 1999 Optimal disturbances and bypass transition in boundary layers. *Phys. Fluids* **11**, 134–150.
- ANDERSSON, P., BRANDT, L., BOTTARO, A. & HENNINGSON, D. S. 2001 On the breakdown of boundary layers streaks. *J. Fluid Mech.* **428**, 29–60.
- BAGHERI, S., ÅKERVIK, E., BRANDT, L. & HENNINGSON, D. S. 2009a Matrix-free methods for the stability and control of boundary layers. *AIAA J.* **47**, 1057–1068.
- BAGHERI, S., BRANDT, L. & HENNINGSON, D. S. 2009b Input-output analysis, model reduction and control of the flat-plate boundary layer. *J. Fluid Mech.* **620**, 263–298.
- BLACKBURN, H. M., BARKLEY, D. & SHERWIN, S. J. 2008 Convective instability and transient growth in flow over a backward-facing step. *J. Fluid Mech.* **608**, 271–304.
- BRANDT, L., COSSU, C., CHOMAZ, J.-M., HUERRE, P. & HENNINGSON, D. S. 2003 On the convectively unstable nature of optimal streaks in boundary layers. *J. Fluid Mech.* **485**, 221–242.
- BUTLER, K. M. & FARRELL, B. F. 1992 Three-dimensional optimal perturbations in viscous shear flow. *Phys. Fluids A* **4**, 1637–1650.
- CATHALIFAUD, P. & LUCHINI, PAOLO 2000 Algebraic growth in boundary layers: Optimal control by blowing and suction at the wall. *Eur. J. Mech. B - Fluids* **19**, 469–490.
- CHEVALIER, M., SCHLATTER, P., LUNDBLADH, A. & S., HENNINGSON D. 2007 A pseudo spectral solver for incompressible boundary layer flows. *Technical Report, Trita-Mek* **7**.
- CHOMAZ, J. M. 2005 Global instabilities in spatially developing flows: non-normality and nonlinearity. *Annu. Rev. Fluid Mech.* **37**, 357–392.
- CORBETT, P. & BOTTARO, A. 2000 Optimal perturbations for boundary layers subject to stream-wise pressure gradient. *Phys. Fluids* **12** (1), 120–130.
- COSSU, C. & CHOMAZ, J.M. 1997 Global measures of local convective instability. *Phys. Rev. Lett.* **77**, 4387–90.
- EHRENSTEIN, U. & GALLAIRE, F. 2005 On two-dimensional temporal modes in spatially evolving open flows: the flat-plate boundary layer. *J. Fluid Mech.* **536**, 209–218.
- ELLINGSEN, T. & PALM, E. 1975 Stability of linear flow. *Phys. Fluids* **18**, 487–488.
- GASTER, M. 1975 A theoretical model of a wave packet in a boundary layer over a flat plate. *Proc. R. Soc. London, Ser. A* **347**, 271–289.
- GASTER, M. & GRANT, I. 1975 An experimental investigation of the formation and development of a wave packet in a laminar boundary layer. *Proc. R. Soc. London, Ser. A* **347**, 253–269.

- JOVANOVIĆ, M. R. & BAMIEH, B. 2005 Componentwise energy amplification in channel flows. *J. Fluid Mech.* **534**, 145–183.
- KOCH, W. 2002 On the spatio-temporal stability of primary and secondary crossflow vortices in a three-dimensional boundary layer. *J. Fluid Mech.* **456**, 85–111.
- KREISS, G., LUNDBLADH, A. & HENNINGSON, D. S. 1994 Bounds for threshold amplitudes in subcritical shear flows. *J. Fluid Mech.* **270**, 175–198.
- LANDAHL, M. T. 1980 A note on an algebraic instability of inviscid parallel shear flows. *J. Fluid Mech.* **98**, 1–34.
- LEHOUCQ, R. B., SORENSEN, D. & YANG, C. 1997 *Arpack users' guide: Solution of large scale eigenvalue problems with implicitly restarted Arnoldi methods*. Technical Report from <http://www.caam.rice.edu/software/ARPACK/>, Computational and Applied Mathematics, Rice University, October 1997.
- LEVIN, O. & HENNINGSON, D. S. 2003 Exponential vs algebraic growth and transition prediction in boundary layer flow. *Flow, Turbulence and Combustion* **70**, 183–210.
- LUCHINI, P. 2000 Reynolds-number-independent instability of the boundary layer over a flat surface: Optimal perturbations. *J. Fluid Mech.* **404**, 289–309.
- LUNDELL, F. & ALFREDSSON, P. H. 2004 Streamwise scaling of streaks in laminar boundary layers subjected to free-stream turbulence. *Phys. of Fluids* **16** (5), 1814–1817.
- MAMUN, CHOWDHURY K. & TUCKERMAN, LAURETTE S. 1995 Asymmetry and hopf bifurcation in spherical couette flow. *Phys. Fluids* **7** (1), 80–91.
- MARQUET, O., SIPP, D., CHOMAZ, J. M. & JACQUIN, L. 2008 Amplifier and resonator dynamics of a low-reynolds-number recirculation bubble in a global framework. *J. Fluid Mech.* **605**, 429–443.
- NAYAR, M. & ORTEGA, U. 1993 Computation of selected eigenvalues of generalized eigenvalue problems. *J. Comput. Phys.* **108**, 8–14.
- NORDSTRÖM, J., NORDIN, N. & HENNINGSON, D. S. 1999 The fringe region technique and the Fourier method used in the direct numerical simulation of spatially evolving viscous flows. *SIAM J. Sci. Comp.* **20**, 1365–1393.
- REDDY, S. C. & HENNINGSON, D. S. 1993 Energy growth in viscous channel flows. *J. Fluid Mech.* **252**, 209–238.
- SCHMID, P. J. & HENNINGSON, D. S. 2001 *Stability and transition in shear flows*. Springer.
- TREFETHEN, L. N., TREFETHEN, A. E., REDDY, S. C. & DRISCOLL, T. A. 1993 Hydrodynamic stability without eigenvalues. *Science* **261**, 578–584.
- TREFETHEN, N. & EMBREE, M. 2005 *Spectra and Pseudospectra; The Behaviour of nonnormal matrices and operators*. Princeton University Press,.
- TUCKERMAN, L.S & BARKLEY, D. 2000 *Bifurcation Analysis For Timesteppers*, pp. 453–566. *Numerical Methods for Bifurcation Problems and Large-Scale Dynamical Systems* . Springer, New York.